

## ABSTRACT

NIKAS, ARIEL NICHOLE. Morphoelastic Modeling Applied to Stomach Bending and Lung Branching. (Under the direction of Sharon R. Lubkin.)

Morphoelasticity, an emerging area of continuum mechanics, can describe the large strains of organogenesis. This framework multiplicatively decomposes the deformation gradient tensor into a growth tensor and an elasticity tensor that ensures compatibility. We apply this framework to two systems, lung branching and stomach bending.

In the embryonic stomach, the curvature changes as the stomach develops and the stomach shape becomes LR asymmetric. However, the emergence of the asymmetry in the stomach during organogenesis is not well understood. Recent experiments have shown that asymmetrical gene expression in some way causes this bending rather than external forces or rotation. We modeled several different types of growth using nonlinear solid mechanics to test hypotheses on the cause of stomach bending. In this thesis, we ruled out a greater rate of overall mitotic growth on the left as the cause for asymmetry in the stomach. Rather, we found that anisotropic growth, representing different oriented cell rearrangements or divisions, is necessary to obtain the shape changes seen in the developing stomach. Specifically, increased axial lengthening combined with radial thinning on the left side create a shape change most similar to published experimental studies.

Many previous models of lung branching morphogenesis were focused on the complex morphogen signaling systems and either omit explicit modeling of shape change, or model shape change by moving a surface normal to itself without explicit mechanics equations. Previous models have shown that morphogen flux distribution corresponds to the location of branching, and that this distribution is reliant on local geometry. In this dissertation, we explicitly modeled both the morphogen signaling and the resulting growth dependent on the calculated morphogen flux distribution, in a novel application of morphoelastic shell modeling for lung growth. We concluded that local geometry affects the resulting shape change. Specifically, we observed tubule lengthening for all local geometries and shouldering for epithelium of elliptical cross-section. We also observed that

the thickness of the epithelium affects the resulting shape change. These two different modeling approaches of solid mechanics and shell mechanics combined with morphoelasticity allowed us to test complex hypotheses on growth and can be generalized for many other organ systems.

© Copyright 2019 by Ariel Nichole Nikas

All Rights Reserved

Morphoelastic Modeling Applied to Stomach Bending and Lung Branching

by  
Ariel Nichole Nikas

A dissertation submitted to the Graduate Faculty of  
North Carolina State University  
in partial fulfillment of the  
requirements for the Degree of  
Doctor of Philosophy

Applied Mathematics

Raleigh, North Carolina

2019

APPROVED BY:

---

Mansoor Haider

---

Nanette Nascone-Yoder

---

Ralph Smith

---

Sharon R. Lubkin  
Chair of Advisory Committee



## **DEDICATION**

To Watson Nikas. You walked across my keyboard while I was applying to graduate school and you walked across my keyboard while I was finishing my dissertation.

## **BIOGRAPHY**

The author was born in Maryland in 1991. Ariel competed in timed hard drive replacing, which explains a lot. She then attended Meredith College in Raleigh, North Carolina where she graduated with a B.S. in mathematics. During her time at Meredith, she also earned a black belt in aikido. Later she got third in a 0.262 mile race.

## ACKNOWLEDGEMENTS

This work would not have been possible without the support of many people. I would like to thank my advisor, Dr. Sharon Lubkin, who listened to many wild speculations, read too many drafts, and always had a good story. I would also like to thank my committee members, Ralph Smith, Mansoor Haider, and Nanette Nascone-Yoder, who taught me to model and ask questions. None of this could have been done without the patience and kindness of many people from the department, especially the assistance of Di Buckland and Carolyn Gunton.

This work would not have been possible to complete without support from the CRSC at North Carolina State University and Dr. Hien Tran.

I would like to thank all my Meredith College math professors, especially Dr. C. Manning who supervised my undergraduate research and got me started on this path and Dr. Hontz who taught the majority of my math classes and was always available for advice. I appreciate your belief that I could do this.

Thank you to my family for feeding me, watching too much of *The Hobbit*, and randomly handing me avocados to go home with.

Of course, I would like to acknowledge Travis Rhea who did too much to detail in any way that represents the actual amount. Thank you for the love and support and for never giving up on me even when I was delirious from lack of sleep, and always being down for taco Tuesday.

Thank you to the McElroy brothers Justin, Travis, and Griffin who were full of advice for the modern era but also goofs. This degree does not make me a doctor of "horse-bone-ology."

I would like to thank all the cats I have lived with over my time in graduate school, my beloved Watson Nikas, Burton Guster Nikas-Rhea, Oxford Nikas-Chaney, Dr. Pep Pepterson Thomas, Pudlet Thomas, and Thea Noorman.

And of course to my wonderful fellow graduate students, Emma Sorrel, Ben Randall, and Evan Curcio.

## TABLE OF CONTENTS

<b>LIST OF TABLES</b> . . . . .	<b>vii</b>
<b>LIST OF FIGURES</b> . . . . .	<b>viii</b>
<b>Chapter 1 Overview</b> . . . . .	<b>1</b>
1.1 Organ Morphogenesis . . . . .	2
1.1.1 Stomach Organogenesis . . . . .	3
1.1.2 Lung Organogenesis . . . . .	4
1.2 Morphogenesis Modeling Overview . . . . .	4
1.2.1 Agent-based Modeling Approaches . . . . .	5
1.2.2 Continuum Modeling Approaches . . . . .	5
1.3 Isotropy, Anisotropy, and Inhomogeneity of Growth . . . . .	6
1.4 Mathematical Background . . . . .	8
1.4.1 Morphoelasticity . . . . .	8
1.4.2 Continuum Mechanics . . . . .	16
1.4.3 Hyperelasticity . . . . .	18
1.5 Summary of Morphoelastic Framework . . . . .	21
<b>Chapter 2 Details of Mechanics</b> . . . . .	<b>24</b>
2.1 Solid Mechanics . . . . .	24
2.1.1 One-Dimensional Example . . . . .	26
2.1.2 Three-Dimensional Example . . . . .	27
2.2 Shell Mechanics . . . . .	29
2.2.1 General Shell Theory . . . . .	32
<b>Chapter 3 Implementation &amp; Verification</b> . . . . .	<b>37</b>
3.1 COMSOL Implementation . . . . .	37
3.1.1 Implementing Growth . . . . .	38
3.1.2 Local Coordinate Systems . . . . .	39
3.1.3 Hyperelasticity . . . . .	42
3.2 Model Verification . . . . .	42
3.2.1 Two-Dimensional Tests . . . . .	43
3.2.2 Three-Dimensional Tests . . . . .	47
<b>Chapter 4 Stomach Bending</b> . . . . .	<b>48</b>
4.1 Motivation . . . . .	48
4.2 Two-Dimensional Model . . . . .	49
4.2.1 Model Geometry . . . . .	49
4.2.2 Modeling Assumptions . . . . .	51
4.2.3 Two-Dimensional Results . . . . .	51
4.3 Three-Dimensional Model . . . . .	55
4.3.1 Modeling Assumptions . . . . .	56

4.3.2	Results	60
4.4	Conclusions	69
<b>Chapter 5</b>	<b>Lung Branching</b>	<b>71</b>
5.1	Problem Background	72
5.1.1	Brief Overview of Published Models	72
5.1.2	Simplified Signaling and Spatial Distribution of Morphogen Flux	74
5.2	Modeling Morphogenesis of the Embryonic Lung	76
5.2.1	Histological Assumptions	76
5.2.2	Geometry Assumptions	77
5.2.3	Morphogen Transport	79
5.2.4	Growth and Mechanics Model	81
5.2.5	Material Assumptions	83
5.2.6	Shell Mechanics	83
5.3	Numerical Experiments	85
5.3.1	Geometry Definitions	86
5.3.2	Boundary Conditions for Growth and Stresses	87
5.3.3	Case 1: Axisymmetric	88
5.3.4	Case 2: Circular Epithelial Cross Section Inside Elliptical ROI Cross Section	89
5.3.5	Case 3: Elliptical Epithelial Cross Section Inside Circular ROI Cross Section	91
5.3.6	Case 4: Elliptical Epithelial Cross Section Inside Elliptical ROI Cross Section	92
5.3.7	Varying Epithelial Thickness	93
5.4	Conclusions	95
<b>Chapter 6</b>	<b>Discussion</b>	<b>99</b>
6.1	Stomach Bending	99
6.2	Lung Branching	101
6.3	Further Extension	102
6.4	Conclusion	103
<b>BIBLIOGRAPHY</b>		<b>104</b>
<b>APPENDICES</b>		<b>108</b>
Appendix A	Preliminary Numerical Experiments	109
Appendix B	Mixed Interpolation of Tensorial Components	116

## LIST OF TABLES

Table 1.1	Tensors in morphoelastic framework. All tensors in this document are represented as bold characters where possible. . . . .	22
Table 1.2	Vectors in morphoelastic framework. . . . .	22
Table 1.3	Variables and functions in morphoelastic framework. . . . .	23
Table 1.4	Parameters in morphoelastic framework. . . . .	23
Table 1.5	Geometries in morphoelastic framework. . . . .	23
Table 2.1	Variables and Parameters used in morphoelastic solid mechanics framework. . . . .	25
Table 3.1	Lamé coefficients $\mu$ for each Poisson's ratio $\nu$ . For use in comparing the hyperelastic model, corresponding Lamé coefficients $\mu$ for each Poisson's ratio $\nu$ , used in the linear elastic model, were calculated from Equation 3.10. However, this had no effect on the outcome of the morphoelastic model. Regardless of the parameters, the model remained at 0% error. The new length in $x$ , formerly 1mm, is represented by $\hat{x}$ . The new length in $y$ , formerly 1 mm, is represented by $\hat{y}$ . The new area in $A$ , formerly 1 mm <sup>2</sup> , is represented by $\hat{A}$ . . . . .	45
Table 3.2	Mesh refinement. A mesh refinement study showed that a finer mesh is unnecessary to maintain optimal accuracy of the hyperelastic model in a simple 1 mm by 1 mm square. . . . .	45
Table 3.3	Linear elastic versus hyperelastic convergence. A comparison between the linear elastic and hyperelastic model shows that the linear model fails to converge above 30% strain. As expected outside the range of infinitesimal strains, the linear model will have issues converging. The hyperelastic model continues to work through all growth strains tested which supports our modeling choice of using a hyperelastic formulation rather than a linear elastic formulation for our simulations. . . . .	46
Table 4.1	Left-right (LR) endoderm and mesoderm width ratios in developing mice and frogs as calculated from the reported medians. The width the endoderm and mesoderm on the left and right side of the mouse and frog stomach changes as the stomach develops. Both sides begin with statistically the same size endoderm, however the ratio of the left to the right decreases to become statistically significantly different from 1 over time as calculated by the authors of [Dav17]. This data was captured from plots in Figure 2E, F, M, and N in [Dav17]. Asterisks indicate values found to be statistically different from 1 as calculated by the authors of [Dav17]. . . . .	55
Table 5.1	Lung bud measurements from [Mai01] and [Jon19]. All measurements were based on control, stage E12.5 mouse lungs. . . . .	78

## LIST OF FIGURES

Figure 1.1	Example of growth with material isotropy. For an isotropic material, isotropic growth results in dilation but no shape change. Where the same area change is maintained in this example, anisotropic growth here is shown as growth horizontally but not vertically. . . . .	6
Figure 1.2	Example of isotropic growth with material anisotropy. For an anisotropic material, isotropic growth can result in shape changes. In this case the material is stiffer vertically than horizontally and when grown isotropically does not extend as much in the vertical direction. When material properties are the same in every direction and the domain is grown isotropically, the shape enlarges. . . . .	7
Figure 1.3	Uniform growth compared to differential growth. Uniform, isotropic growth of an isotropic material results in a dilation of the original shape and is an affine transformation. Differential growth in an isotropic material results in a change of shape and may not be an affine transformation. . . . .	8
Figure 1.4	Types of growth for isotropic materials, illustrated on a cylinder. Isotropic uniform growth is an enlargement of the original body. Uniform anisotropic growth is shown for each of the cylindrical coordinate directions $(r, \theta, z)$ with stretch ratios $\lambda_r, \lambda_\theta$ , and $\lambda_z$ . Inhomogeneous isotropic growth, where the growth is different in certain areas of the domain, causes obvious shape change. We consider this geometry further in Chapter 2. . . . .	9
Figure 1.5	Mapping of the initial configuration to the deformed configuration. $B_0$ is the initial configuration with position vector $X$ . $B$ is the deformed configuration with position vector $x$ . The initial position vector $X$ can be mapped to the deformed configuration's position vector $x$ using the displacement vector $u$ . . . . .	10
Figure 1.6	Application of growth and elastic tensors to an initial configuration. Only considering the growth tensor $\mathbf{G}$ can lead to incompatibilities in the body. Coupled with an elastic deformation tensor $\mathbf{A}$ however, these incompatibilities are resolved. Both the growth tensor and the elastic deformation tensor in this order under right polar decomposition give the overall deformation tensor $\mathbf{F}$ . Image adapted from [Rod94]. . . . .	12
Figure 2.1	Model components. For each of our models, we specify a domain $\Omega$ and a local coordinate system. We use the framework of morphoelasticity in solids and shells, where we specify the growth tensor $\mathbf{G}$ as an input for each model. In particular for Chapter 5, the stretch ratio $\lambda$ is a function of the flux $j(X)$ which is determined via coupling to a steady state diffusion model. Unless otherwise specified all boundary surfaces are considered to be under no stress, $\hat{n} \cdot \sigma = 0$ . Specific no displacement boundary conditions are given with each model. Because none of our models are time-dependent, there are no initial conditions. . . . .	27

Figure 2.2	Growth of a cylinder. For a cylinder of radius 1 mm and height of 2 mm, we set $\text{diag}(\mathbf{G})=(1,1,2)$ in order to double the height. We had no stress boundary conditions on all the faces, no external pressure, and no displacement or rotation at an arbitrary point. To reflect our models in later chapters, we also chose to have no $z$ displacement at on the bottom face of the cylinder. The error between our analytical volume and the calculated deformed volume $\hat{V}$ was 0.0002%. . . . .	30
Figure 2.3	Depiction of shell element. The $n$ direction is locally normal to the shell midsurface, and the $\alpha$ and $\beta$ directions follow the directions of principal curvature, after [Smi05]. . . . .	33
Figure 3.1	Domain and boundary conditions used to solve for local coordinate systems in an example 2D domain. We solve $\nabla^2 q = 0$ in the domain $\Omega$ . There are no flux boundary conditions, $n \cdot \nabla q = 0$ , on $\partial\Omega_1$ and $\partial\Omega_3$ . Without loss of generality at $\partial\Omega_4$ $q = 1$ and at $\partial\Omega_2$ $q = 0$ . . . . .	40
Figure 3.2	Curves following the direction of the gradient of $q$ for calculating local coordinates. We calculated the curves of an example vector field from the Laplace equation with an inlet $q = 1$ on the bottom right face and an outlet $q = 0$ on the bottom left face. Notice how the calculated curves follow the curve of the domain. . . . .	41
Figure 3.3	Local curvilinear coordinate system. Our local curvilinear coordinate system was calculated in this example for half of our stomach geometry seen later in Chapter 4. The first basis vector, in red, follows the curves of the domain, the second basis vector, in green, is in the $z$ direction, and the third, in blue, is locally orthogonal to both the previous vectors. . . . .	41
Figure 3.4	Example domain with a clear analytical solution. We tested the accuracy of our model in a simple 1 mm by 1 mm square whose new dimensions we would be able to calculate analytically. This two-dimensional geometry was used for many tests to compare the hyperelastic model to the linear elastic model and check the accuracy of each. . . . .	44
Figure 3.5	Doubling the width and halving the height of a square. Even with strains as large as 100%, the multiplicatively decomposed hyperelastic model remains accurate. Here we implemented a 100% strain in the $x$ -direction and a -50% strain in the $y$ -direction to create a 2 mm by 1 mm rectangle from our 1 mm by 1 mm square. Area is conserved. . . . .	47
Figure 4.1	Cross section of a developing frog at stages 34, 37, and 39. The epithelium is false-colored pink and yellow on the right and left side respectively. The mesenchyme is false-colored aqua on the right side and blue on the left side. Notice the difference in curvature in Stages 34 and 39 but also the consistent location of the top attachment point. From [Dav17]. . . . .	49



Figure 4.2	Simplified 2D histology. The simplified histology for the our model incorporates the four distinct sections of the stomach (right and left endoderm and right and left mesoderm) and the liver, for completeness, with colors corresponding to the previous figure. The size of the stomach at this stage is approximately $400\ \mu\text{m}$ by $200\ \mu\text{m}$ , based on measurements from [Dav17]. Note that the right side of all images corresponds to the left side of the stomach as in [Dav17] from an anterior viewpoint. All directions are stated in reference to this orientation. . . . .	50
Figure 4.3	Test of stiffness effects. (A) has the maximal stiffness of $E = 1000\ \text{Pa}$ on the interior and the minimal stiffness of $E = 100\ \text{Pa}$ on the exterior. (B) is meant as a control where both domains have the same stiffness $E = 100\ \text{Pa}$ . (C) has the maximal stiffness of $E = 1000\ \text{Pa}$ on the exterior and the minimal stiffness of $E = 100\ \text{Pa}$ on the interior. In the simulations shown, areas of positive stress (tension) are depicted in blue and negative stress (compression) are depicted in red. . . . .	52
Figure 4.4	Tests for growth location. Each column represents a different scenario of domain expansion. As the endoderm expanded in (A) it began to curve the opposite direction of what was anticipated. (B) Both regions expanded and it curved in the correct direction. However (C) had the most dramatic curve. In the simulations shown, areas of tension are depicted in blue and compression are depicted in red. . . . .	53
Figure 4.5	Growth in the domain as compared to the boundary. The columns compare (A) expanding the left side mesoderm to (B) growing the left side's boundary. The left boundary expansion did not give the expected qualitative result. In the simulations shown, areas of tension are depicted in blue and compression are depicted in red. . . . .	54
Figure 4.6	Parametric study of isotropic stretch ratio as it affects curvature. A representative sample from our parametric study shows growth strains of (A) $\lambda = 1$ , (B) 1.25, and (C) 1.5 in the mesoderm layer. More dramatic curvature is seen at the higher values of $\lambda$ , as predicted. In the simulations shown, areas of tension are depicted in blue and compression are depicted in red. . . . .	54
Figure 4.7	Size comparison of endoderm to mesoderm. At Stage 34 and 39, the endoderm is the larger tissue on the left and right sides of the frog stomach. The change of left and right endoderm size over time is quantified in Table 4.1. From [Dav17]. . . . .	56
Figure 4.8	Simplified 3D geometry for the undeformed stomach. For all subfigure labelling: D: dorsal, V: ventral, A: anterior, P: posterior. L and R are the initially symmetric left and right sides respectively. (A) is a view of the anterior face. (B) is a dorsal view. (C) is a cut view of the dorsal half. Color differentiation is to aid in visualization of the shape change. . . . .	57

Figure 4.9	Boundary conditions for the half domain. Due to the initial symmetry of our domain, we computed our model on a half domain. The bottom two faces have a symmetry boundary condition, meaning they have no normal displacement to the cut plane. We pinned a point, giving it no rotation and no displacement. All other surfaces have a no stress boundary condition, $\hat{n}\sigma = 0$ . As an additional modeling assumption due to surrounding tissues, the two posterior faces cannot move normal to the plane but are free in the other directions. . . . .	57
Figure 4.10	Local coordinate system $(R, h, z)$ . The black arrows give the local coordinate directions from the origin. The green vector arrows represent the axial direction $z$ . The red vector arrows represent the hoop direction $h$ and the blue vector arrows represent the radial direction $R$ . . . . .	58
Figure 4.11	Isotropic growth of the left side of the stomach and no growth of the right side. The stretch ratio in each direction is $\lambda_R = \lambda_h = \lambda_z = 1.2$ . Under isotropic growth, the geometry becomes asymmetric and very slight bending relative to the applied growth is seen in the biologically anticipated direction in (A)-(C). This bend may increase given a higher stretch ratio. (C) The cut view is shown in perspective to aid with visualization of the bending. . . . .	61
Figure 4.12	Anisotropic growth on the left side in the radial direction. The stretch ratios are $\lambda_R = 1.2$ , $\lambda_h = 1$ , $\lambda_z = 1$ . We observe thickening in the left side of the stomach in (A) and no bending in (A)-(C). Neither outcome is consistent with the shape changes seen in the developing frog stomach. . . . .	61
Figure 4.13	Anisotropic growth on the left side in the hoop direction. The stretch ratios are $\lambda_R = 1$ , $\lambda_h = 1.2$ , $\lambda_z = 1$ . The stomach appeared to extend in the dorsal-ventral direction in (A) but does not bend in the biologically anticipated direction in (B)-(C). This is not consistent with the shape changes seen in the developing frog. . . . .	62
Figure 4.14	Anisotropic growth on the left side in the axial direction. The stretch ratios are $\lambda_R = 1$ , $\lambda_h = 1$ , $\lambda_z = 1.2$ . In (A)-(C), the deformed geometry shows bending from the left side over to the right side. However, it fails to show the radial thinning observed in [Dav17]. . . . .	63
Figure 4.15	Volume conserving anisotropic growth on the left side in the radial direction with shrinking in the axial direction. The stretch ratios are $\lambda_R = 1.2$ , $\lambda_h = 1$ , $\lambda_z = 1/1.2$ . This shows the deformed right side crossing over into the left in (A)-(C) which is not consistent with what is seen in the embryonic frog. . . . .	64
Figure 4.16	Volume conserving anisotropic growth on the left side in the radial direction with contraction in the hoop direction. The stretch ratios are $\lambda_R = 1.2$ , $\lambda_h = 1/1.2$ , $\lambda_z = 1$ . In views (A)-(C), this shows the deformed right side crossing over into the left which is not consistent with what is seen in the embryonic frog. . . . .	64

Figure 4.17	Volume conserving anisotropic growth on the left side in the radial direction with shrinking in the axial direction and contracting in the hoop direction. The stretch ratios are $\lambda_R = 1.2$ , $\lambda_h = 1/\sqrt{1.2}$ , $\lambda_z = 1/\sqrt{1.2}$ . In all views (A)-(C), the deformed right side crossed over into the left which is not consistent with what is seen in the embryonic frog. . . . .	65
Figure 4.18	Volume conserving anisotropic growth in the hoop direction with shrinking in the axial direction. The stretch ratios are $\lambda_R = 1$ , $\lambda_h = 1.2$ , $\lambda_z = 1/1.2$ . (B) and (C) show bending in the opposite direction seen in [Dav17]. . . . .	66
Figure 4.19	Volume conserving anisotropic growth in the hoop direction with shrinking in the radial direction. The stretch ratios are $\lambda_R = 1/1.2$ , $\lambda_h = 1.2$ , $\lambda_z = 1$ . (A) This shows bending in the opposite direction seen in [Dav17] though not to the extreme of the previous Figure 4.18. . . . .	66
Figure 4.20	Volume conserving anisotropic growth in the hoop direction with shrinking in the radial and axial direction. The stretch ratios are $\lambda_R = 1/\sqrt{1.2}$ , $\lambda_h = 1.2$ , $\lambda_z = 1/\sqrt{1.2}$ . (B)-(C) Bending is in the opposite direction seen in [Dav17]. . . . .	67
Figure 4.21	Volume conserving anisotropic growth in the axial direction with contraction in the hoop direction. The stretch ratios are $\lambda_R = 1.2$ , $\lambda_h = 1/1.2$ , $\lambda_z = 1.2$ . (B)-(C) show bending in the biologically anticipated direction. . . . .	68
Figure 4.22	Volume conserving anisotropic growth in the axial direction with thinning in the radial direction. The stretch ratios are $\lambda_R = 1/1.2$ , $\lambda_h = 1$ , $\lambda_z = 1.2$ . (A)-(C) show bending in the biologically anticipated direction and (A) includes the thinner width on the left seen in [Dav17] as well. . . . .	68
Figure 4.23	Volume conserving anisotropic growth in the axial direction with contraction in the hoop direction and thinning in the radial direction. The stretch ratios are $\lambda_R = 1/\sqrt{1.2}$ , $\lambda_h = 1/\sqrt{1.2}$ , $\lambda_z = 1.2$ . (A)-(C) all show bending in the biologically anticipated direction . . . . .	69
Figure 5.1	Three modes of lung branching as defined and shown in [Met08]. The three modes of lung branching were defined as domain, planar, and orthogonal branching. For domain branching, new lung bud tips grow from the sides of an existing stalk. For planar bifurcation, the tip of an existing lung bud splits and this pattern continues iteratively. This results in lung tips that all lie on a line, as seen in the end view of the figure. For orthogonal bifurcation, the tip of a lung bud splits but the next generation of splitting is rotated $90^\circ$ . This results in lung bud tips that do not exist along the same line but rather in a plane, as seen in the end view of the figure. [Met08] hypothesized that these different modes were all caused by different mechanisms. Reproduced from [Met08]. . . . .	73
Figure 5.2	Packing of lung buds. <b>A</b> displays the an example partitioning of a mouse lung into regions of interest. Simplified example regions of interest can be seen in subfigure <b>B</b> . These regions of interest further display the different curvatures of the mesothelial surface that occur in different regions of the developing lung. From [GL18]. . . . .	77

Figure 5.3	Simplified histology of a single lung branch tip. Our simplified histology for a single lung branch tip includes the mesothelial surface, mesenchyme, epithelium, and lumen. The epithelium is a thin barrier tissue separating the mesenchyme from the lumen. Morphogens diffuse from the signaling mesothelial surface, represented by the blue line, through the mesenchyme, to be absorbed or bound on the epithelium, represented by the solid black line. Morphogen flux to the epithelium drives the shape change of the epithelium.	78
Figure 5.4	Geometric measures in an E12.5 mouse lung annotated from [Jon19] left and [Mai01] right. $2R_M$ is the full distance from one epithelial surface to another. We consider half this distance to be the location of the edge of our mesenchyme in our region of interest, where our region of interest can be considered to be the zone inside the blue dashed line. $\Phi$ is the thickness of the epithelium, assumed to be constant. $L$ is the distance between the basal epithelial surface and the pleural surface through the mesenchyme. $R_e$ is the distance across the lung bud from basal epithelial surface to basal epithelial surface.	79
Figure 5.5	Domain and boundaries for the transport model. In $\Omega$ , $D\nabla^2 c = 0$ . The boundary condition for the pleural surface, $\partial\Omega_P$ , is $\hat{n} \cdot D\nabla c = k$ , meaning the morphogen is being produced at a constant rate represented as a constant flux. The boundary condition for the sides $\partial\Omega_S$ and bottom $\partial\Omega_B$ is $\hat{n} \cdot D\nabla c = 0$ , because our region of interest has no net flux given that it is modeled as packing with its neighbors. The boundary condition for the epithelium, $\partial\Omega_E$ , is given by $c = 0$ , meaning all morphogen is assumed to be absorbed there.	80
Figure 5.6	Local orthogonal coordinates for the shell. The local coordinates $(\eta_1, \eta_2, \eta_3)$ have corresponding unit vectors that are tangential in the direction of maximum curvature, tangential in the direction of minimum curvature, and normal to the shell surface, respectively. A representative shell piece is shown with its local coordinate system.	82
Figure 5.7	Location in shell. The bottom or apical surface is considered to be located at $\tilde{z} = -1$ and the top or basal at $\tilde{z} = 1$ . In this two dimensional figure, the midsurface is represented by a dotted line. In thin shells planes normal to the midsurface, with the normal direction represented by the blue arrow in this two-dimensional simplification, remain normal to the midsurface even after deformation. In thick shells, that is not necessarily the case. For our model, we consider the positive normal direction to be oriented away from the lumen towards the mesothelial surface, or apicobasally.	85
Figure 5.8	Sketch of lung ROI geometry. (A) The cross section view shows a dotted line of symmetry and the polar distance between the pleural and basal epithelial surface $L$ . (B) Other geometric parameters of interest are the minor axis of the inner ellipse, $a_1$ , the major axis of the inner ellipse, $a_2$ , the minor axis of the outer ellipse, $A_1$ , and the major axis of the outer ellipse, $A_2$ . Axes of reflection symmetry are represented by dotted lines.	86

Figure 5.9	Boundary condition on cut plane. For a top down view, with $\Phi$ displaying the thickness of the shell, we have a plane of symmetry in red. All surfaces of the shell are under no stress, the surfaces touching the cut plane cannot move normal to the plane or rotate, and bottom surface of the plane also has no normal displacement. . . . .	87
Figure 5.10	Local ROI geometry of a cylindrical epithelium tubule nested in a larger cylindrical mesenchyme and its morphogen flux distribution pattern. As $L$ decreases, the circular morphogen flux hot spot becomes a morphogen flux ring, denoted by "O". The authors of [GL18] hypothesized that a circular morphogen flux distribution pattern would correspond to tubule extension, while an annular morphogen flux distribution pattern was hypothesized to result in the the tip of the tubule dimpling or flattening. As annotated from [GL18]. . . . .	88
Figure 5.11	Flux and growth of epithelium of circular cross section inside a mesenchyme of circular cross section. As previously defined, $L$ is the distance between the basal epithelial surface and the pleural surface in $\mu\text{m}$ . In the local cross-sectional geometry of an epithelium of circular cross section nested in a mesenchyme of circular cross section with a cross-sectional area ratio of 1:4, we considered several $L$ values. Higher normal flux magnitude is displayed in darker colors. Larger values for $L$ lead to a circular flux distribution pattern and epithelial extension towards the pleural surface, while small values of $L$ lead to an annular region of higher flux magnitude and epithelial extension but no perceptible flattening. . . . .	89
Figure 5.12	Epithelium of circular cross section inside a mesenchyme ROI of elliptical cross section. Large values of $L$ result in circular hot spots, while a small $L$ value shows a split in the area of high flux distribution. In [GL18], the authors hypothesized that single hot spots for this geometry would cause extension of the epithelium, while tip splitting or branching of the epithelium is hypothesized to occur for split hot spots when an epithelium of circular cross section is inside a mesenchyme of elliptical cross section. Image annotated from [GL18]. . . . .	90
Figure 5.13	Flux and growth of epithelium of circular cross section inside a mesenchyme of elliptical cross section. We observed that at the smallest $L$ value the flux distribution pattern splits into two zones, as shown in [GL18]. However, we did not observe shouldering given the split morphogen flux distribution in this simulation. We found that all $L$ values and their different morphogen flux distributions corresponded to extension. . . . .	91

Figure 5.14	Epithelium of elliptical cross section in a mesenchyme circular cross section. The flux distribution splits into two hot spots as $L$ decreases. In [GL18], tip splitting or branching is hypothesized to occur for split flux distributions, like that seen when $L$ is small in a local geometry of an epithelium of elliptical cross section is inside a mesenchyme of circular cross section. Larger $L$ values for this geometry cause a single hot spot. This hotspot is hypothesized to lead to epithelial extension towards the pleural surface. Image annotated from [GL18], . . . . .	92
Figure 5.15	Flux and growth of epithelium of elliptical cross section inside a mesenchyme of circular cross section. In the specific region of interest of an epithelium of elliptical cross section inside a mesenchyme of circular cross section with cross-sectional area ratio of 1:4, we considered $L = 10, 20, 30 \mu\text{m}$ . Darker colors correspond to higher local values of normal flux magnitude. Single morphogen flux hot spots, corresponding to higher $L$ values, showed considerable extension towards the pleural surface. . . . .	93
Figure 5.16	Flux distribution of an epithelium of elliptical cross section inside a mesenchyme of elliptical cross section. In [GL18], single morphogen flux hot spots, seen for the larger $L$ values, for this geometry are hypothesized to lead to epithelial extension towards the pleural surface, while tip splitting or branching of the epithelium is hypothesized to occur for split morphogen flux hot spots, seen for smaller $L$ values, when an epithelium of elliptical cross section is inside a mesenchyme of elliptical cross section. Image annotated from [GL18]. . . . .	94
Figure 5.17	Flux and growth of epithelium of elliptical cross section inside a mesenchyme of elliptical cross section. Our flux distribution matches that seen in [GL18]. Extension of the tubule is seen with single morphogen flux hot spots, seen for the large $L$ values, and some shouldering occurs with all values. . . . .	95
Figure 5.18	Differences in shape change caused by varying epithelial thickness. Comparing the thickness of the epithelium from $\Phi = 15 \mu\text{m}$ to $\Phi = 5 \mu\text{m}$ , we observed that epithelial thickness caused variation in shape change due to growth. Notice that as seen from the top for $\Phi = 5 \mu\text{m}$ the shell changed its cross-sectional aspect ratio much more significantly than for $\Phi = 15 \mu\text{m}$ . . . . .	97
Figure 5.19	Self intersection due to epithelial thickness and interaction with overall shape. For an epithelial cross section with minor axis $20 \mu\text{m}$ and major axis $40 \mu\text{m}$ and thickness of $\Phi = 15 \mu\text{m}$ , simulations converge but the shell self-intersects. This is not biologically realistic. . . . .	98
Figure A.1	Cylindrical geometry for preliminary experiments. The simplified geometry was the same for both solid mechanics and shells. Consider a cylinder whose boundary conditions are no $z$ -displacement and no rotation at the top or bottom. On that cylinder in the slightly darker circle is where the different growth strains were applied. The cylinder had a radius of $250 \mu\text{m}$ , a height $750 \mu\text{m}$ , and a thickness of $50 \mu\text{m}$ . . . . .	110

Figure A.2	Application of local growth strain to a solid cylinder in a cylindrical coordinate system. Using a cylinder that has a height to radius ratio of 3:1, we tested the solid mechanics version of this problem. Going from left to right, we increased the strain by 5% increments from 5% to 20%. More dramatic shape changes would be expected at 20% than at 5%. The color bar represents first principal strain. In (A)-(B), we tested cell rearrangement cases. In (A), the cylinder grew circumferentially but the height shrank and in (B) its height grew but it decreased circumferentially. (C)-(E) are the cellular division cases, where volume is not conserved. In (C) the cylinder grew circumferentially, in (D) along the height, and in (E) in both directions. . . . .	112
Figure A.3	Application of local growth strain to a cylindrical shell in a cylindrical coordinate system. Using the shell formulation instead, we tested the same geometry and growth models as in Figure A.2. Going across we increased the strain from 5% to 10% to 20%. 15% was disregarded because it gave no additional information. The color bar represents first principal strain. In (A)-(B), we tested cell rearrangement cases. In (A), the cylinder grew circumferentially but the height shrank and in (B) its height grew but it decreased circumferentially. (C)-(E) are the cellular division cases, where volume is not conserved. In (C) the cylinder grew circumferentially, in (D) along the height, and in (E) in both directions. . . . .	113
Figure A.4	Effects of boundary conditions. To emphasize that boundary conditions can drastically affect results, two similar cases are shown. Going across the strain is increased by 5% from (A) 5%, (B) 10%, (C) 15%, and (D) 20%. The color bar represents first principal strain. The top row is where this shell formulation has no vertical displacement only on the bottom of the cylinder. The bottom row is where it has no vertical displacement on both the top and bottom of the cylinder. All other conditions are exactly the same. Notice that the top row has interesting dimpling or buckling above the area of strain. . . . .	114
Figure A.5	Cylindrical shell strained while surrounding a solid material. Using the shell formulation but with a relatively low stiffness solid inside, we tested the same geometry. Going across we increased the strain from 5% to 10% to 20%. From top to bottom, we grouped cell rearrangement together, first increasing height and then increasing circumferentially. Then we grouped volumetric growth together increasing in height, then circumference, and then both. Notice that there is very little overall deformation and the strained circle remains in a very similar location and configuration compared to how it began. The color bar represents first principal strain. . . . .	115
Figure B.1	For the same element, the left square shows the interpolation points for the displacement, $\underline{u}$ , and the rotation, $\underline{\theta}$ . In the right square, the tying points are represented by crosses and labelled with A, B, C, and D. As represented in the local coordinates (r,s), A is located at (0,1) and B is located at (-1, 0). Notation after that in [CB11]. . . . .	117

Figure B.2	For the same element, the left square shows the interpolation points for the displacement, $\underline{u}$ , and the rotation, $\underline{\theta}$ as black circles. The additional purple circle represents an additional interpolation point for the rotation only. In the right square, the tying points are represented by crosses and labelled A through H. As represented in the local coordinates (r,s), A is at $(1/\sqrt{3}, 1)$ and C is at $(-1, 1/\sqrt{3})$ . Notation after that in [CB11]. . . . .	117
Figure B.3	Locking of numerical methods. As shown for a linear elastic solid mechanics model, when Poisson's ratio gets closer to 0.5 the relative percent error decreased in a linear fashion. The slight uptick at $\nu = 0.49$ indicates locking. .	118



## CHAPTER

# 1

## OVERVIEW

The term *morphogenesis* describes the processes of growth, cell division, reorganization, and restructuring of a tissue, organ, or organism that change its morphology. We used the emerging field of *morphoelasticity* to model morphogenesis in two complex biological systems, specifically lung branching and stomach bending. Many popular extant morphogenetic models such as agent-based models are not grounded in a physics framework though can be informative when formulated correctly. Using the mathematical theory of morphoelasticity allows us to model complicated systems while still considering the underlying physics.

The stomach in many species has a distinctive curved shape which is important for the proper function of the organ. This curve creates left-right asymmetry in the stomach. We will evaluate hypotheses on the cause of stomach bending due to varying left-right levels of: (a) mitosis, (b) cell rearrangement, or (c) a combination. Models (b) and (c) are mathematically novel in that they represent some of the first implementations of anisotropic growth in morphoelasticity. In this

thesis, we ruled out that a greater rate of overall mitotic growth on the left side of the stomach as compared to the right is cause for the asymmetric bending in the stomach. Instead, we concluded that anisotropic growth, representing different oriented cell rearrangements or divisions on the left and right sides of the stomach, is necessary to obtain the shape changes seen in the developing stomach.

Lungs begin as a single tube that then goes through many iterations of branching in many directions to become fully formed. We will determine the pseudoglandular lung shape changes resulting from growth governed by different morphogen flux distributions as asserted in [GL18]. Our lung models will be the first lung models to include the framework of morphoelasticity, and one of the first morphoelastic models to incorporate thick shell theory. For our novel application, we explicitly modeled both the morphogen signaling, which depends strongly on local geometry, and the resulting growth dependent on the calculated morphogen flux distribution. Unlike many previous models of lung branch growth, we also considered the differences that epithelial thickness may yield in the final shape. Anticipated outcomes from these models will either support or refute proposed biological hypotheses.

## 1.1 Organ Morphogenesis

Mathematical aspects of morphogenesis have been described as early as 1917 by D’Arcy Thompson [Tho61]. Morphogenesis can occur in both developing organisms and in mature organisms, such as during lactation or the formation of tumors. In early development, organs can rapidly change in size, shape, and even material properties. Specifically in early development, *organogenesis* is the term used for the process where the ectoderm, mesoderm, and endoderm form the internal organs. These tissues further differentiate during development. We specifically focus in this thesis on two kinds of tissues: epithelium and mesenchyme. An *epithelium* is a sheet-like tissue that lines the surfaces of organs and separates tissues from each other and from the lumen, a fluid-filled cavity. The size and shape of epithelial cells depend on their function and location but in general they are tightly packed with negligible distance between cells. The *apical* surface of an epithelium is in contact with

a lumen; the *basal* surface of an epithelium is in contact with another tissue. Our second tissue of interest is the *mesenchyme*. The mesenchyme is a tissue containing some widely separated cells in an extracellular matrix (ECM). Often considered connective tissue, the mesenchyme fills the space between epithelia.

To aid in clarity when discussing morphogenesis and early development in general, humans are classified by 23 Carnegie stages which are divided roughly by size, timing, and morphological characteristics [OM01]. These stages have been adapted to other animals and allow us to compare timing during development between species. For mice, it is common practice to refer to embryonic days since timed pregnancy as E and then the day, for example E12.5, and further development after birth begins with P for postnatal. For example, Carnegie stage 16, which is in humans at day 40, in mice is at E12.5. It is important to note that these stages are of varying time periods in humans, between one day and nearly one week. This time period discrepancy arises because the stages are divided based on morphological events, such as limb bud formation or notochord detectability, which do not occur uniformly over time.

### **1.1.1 Stomach Organogenesis**

The embryonic stomach in many vertebrates begins as a straight tube which undergoes significant shape change to become an asymmetric, multiply curved, bent, elliptical tube. This left-right (LR) asymmetry is seen in many organs throughout the body. "Left-right (LR) asymmetry is a fundamental feature of internal anatomy, yet the emergence of morphological asymmetry remains one of the least understood phases of organogenesis. Asymmetric rotation of the intestine is directed by forces outside the gut, but the morphogenetic events that generate anatomical asymmetry in other regions of the digestive tract remain unknown" [Dav17]. We consider the change in stomach shape in *Xenopus laevis* frog embryos from the commonly defined developmental stages 34-39. At stage 34 the embryonic frog stomach is symmetrical, but as it grows, significant asymmetry emerges. In both mice and frogs, the asymmetry of the stomach is known to depend on left-right patterning genes, such as *Foxj1*, *Pitx2*, and *Nodal* [Dav17].

### 1.1.2 Lung Organogenesis

The mature lungs are a richly branched organ that exhibits fractal-like space filling. This results in the large gas exchange surface area essential to the proper function of the lung. Its mature shape is produced by a variety of mechanisms throughout development. In mice, lung organogenesis begins at E9.5 and goes through four major fetal stages [Mas04]. The first is the pseudoglandular stage where branches are formed occurring between E12 and E16.5. Then there are two intermediate stages, the canalicular and saccular, occurring between E16.5 and P4. Further structural changes occur during the alveolar stage from the post-natal development stages P4-P14. We consider the branching of embryonic lungs in the pseudoglandular stage. Epithelium-mesenchyme interaction in branching is essential; experiments have shown that “after removal of the mesenchyme at the growing tip, further branching of the epithelial tubules is prevented” [Mas04]. The morphogenetic behavior of the epithelium has been linked to a number of genes and growth factors such fibroblast growth factor 10 (FGF10), transforming growth factor beta ( $TGF-\beta$ ), and sonic hedgehog (Shh) among others. While many chemicals have been associated with branching, the exact mechanisms that cause specific branching patterns and the mechanics behind this are a continuing area of research.

## 1.2 Morphogenesis Modeling Overview

Morphogenesis is the process by which growth and cell rearrangements alter the shape of a developing tissue. Shape change can be described mathematically as a rearrangement of the relative positions of material points in the body. Many different approaches have been taken to model morphogenesis. We can subdivide the main approaches into continuum-based or agent-based. Common continuum models are based in the theories of poroelasticity, fluid dynamics, solid mechanics, mixture modeling, or are just phenomenological. Agent-based model approaches include vertex models, Lindenmayer systems, cellular Potts models, and some stochastic based models.

### **1.2.1 Agent-based Modeling Approaches**

Agent-based modeling approaches focus on describing individual cell interactions. Agent-based computational models use individual agents that interact following set rules, and can be deterministic or stochastic. One agent-based approach to morphogenesis, vertex modeling, models individual cells as polyhedra where multicellular interactions are defined by vertex movements [Hon04]. Vertex models have been used to simulate tissue morphogenesis but do not include a full physics framework [Oku14], [MI08] [Bar17]. Cellular Potts models, which are stochastic, consider the adhesion between cells to be a driving factor for deformation [Mer06], [SM13], [Hes11]. Using the definition in [GG92], in cellular Potts models a cell's location is defined by a number of adjacent lattice sites. The set of lattice coordinates that defines the cell changes as the cells move and grow as determined by a minimization process of a pseudo-energy function. Hybrid cellular Potts models consider cell movements discretely but model chemical signaling in a continuum [Oer14].

### **1.2.2 Continuum Modeling Approaches**

In continuum modeling, one considers objects to be completely space-filling rather than discrete particles and considers changes to be occurring in some neighborhood around any particular point. For continuum based approaches, a general theory for soft, elastic tissues with finite volumetric growth that mathematically described the relation between stress and growth was developed in [Rod94]. For hard tissues like bone, it has been well established that stress and strain can modulate growth [Rod94]. However, soft tissues, unlike hard tissues, can experience large elastic deformations and become residually stressed [Rod94]. Stress is not only a potential result of growth but may also affect the further growth of the body. Growth may introduce incompatibilities in the body, like self-intersection, that can be resolved with the introduction of an elastic stress. The morphoelastic framework developed in [Rod94] considers that the shape change during growth occurs as a result of material being either added or removed, an elastic deformation, or both. The morphoelastic model system will be more fully described in Section 1.4.1.

### 1.3 Isotropy, Anisotropy, and Inhomogeneity of Growth

For our morphogenesis problems, we consider the change in shape of individual organs. For the purposes of this thesis, we hereafter consider "growth" to be a general term describing a shape change and not necessarily an indicator of an increase in volume. Both growth and materials can be considered isotropic or anisotropic. Shape change can be due to anisotropic growth, isotropic growth of an anisotropic material, or inhomogeneous growth. Since they are all biologically different, we will discuss the distinctions. For simplicity, we consider all materials in this thesis to be isotropic. During morphogenesis, organs can experience growth, in potentially both volume and shape, as cells divide, apoptose, and rearrange. Uniform isotropic growth of an isotropic material gives no change in shape. Biologically that would be equivalent to mitosis, where the rate of mitosis was uniform in every direction and at every location. Volume conserving anisotropic growth is a result of cell rearrangements. Assuming isotropic material properties, Figure 1.1 illustrates the difference between isotropic growth (growth equal in every direction) and anisotropic growth (growth that is different in different directions) for a square whose area is quadrupling. If a material is anisotropic

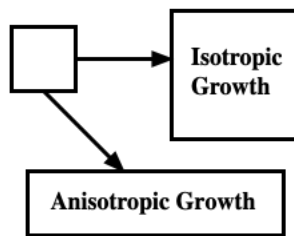


**Figure 1.1** Example of growth with material isotropy. For an isotropic material, isotropic growth results in dilation but no shape change. Where the same area change is maintained in this example, anisotropic growth here is shown as growth horizontally but not vertically.

then the material properties are not the same in every direction. Figure 1.2 illustrates an example of isotropic growth in an anisotropic material.

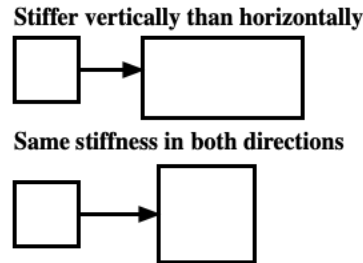


**Figure 1.2** Example of isotropic growth with material anisotropy. For an anisotropic material, isotropic growth can result in shape changes. In this case the material is stiffer vertically than horizontally and when grown isotropically does not extend as much in the vertical direction. When material properties are the same in every direction and the domain is grown isotropically, the shape enlarges.

It is also important to consider differential growth, where the rates of volumetric growth are different in different locations. Figure 1.3 shows an example of the difference between uniform isotropic growth and differential growth.

Figure 1.4 summarizes several of these different types of growth on a cylinder where material properties are assumed to be isotropic. Uniform isotropic growth results in a dilation of the original cylinder. Uniform anisotropic growth results in a change of aspect ratio of the cylinder. Inhomogeneous isotropic growth results in a shape change and does not result in a cylinder. We consider this geometry and the multiple types of growth further in Chapter 4. Notice that because we are considering a cylinder in Figure 1.4 we are using the cylindrical coordinate system. Alternative coordinate systems and how to find them are described in Section 3.1.2.

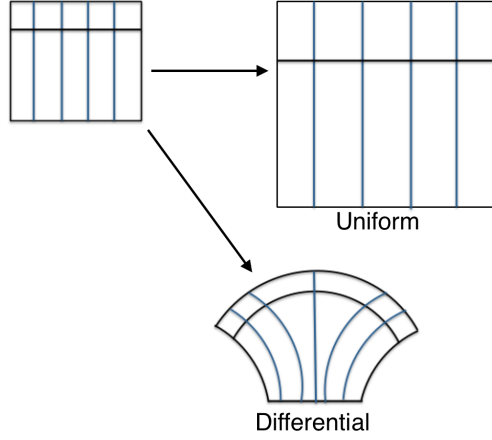


**Figure 1.3** Uniform growth compared to differential growth. Uniform, isotropic growth of an isotropic material results in a dilation of the original shape and is an affine transformation. Differential growth in an isotropic material results in a change of shape and may not be an affine transformation.

## 1.4 Mathematical Background

### 1.4.1 Morphoelasticity

Following the framework developed in [Rod94] and described in detail in [Gor17], we will explain the morphoelastic model structure. In order to describe how a body undergoes a shape or volume change, we consider its initial configuration,  $B_0$ , and its deformed configuration,  $B$ . The relationship between a position vector in the initial configuration and a position vector in the deformed configuration can be represented by

$$x_1 = X_1 + u_1, \quad (1.1)$$

$$x_2 = X_2 + u_2, \quad (1.2)$$

$$x_3 = X_3 + u_3, \quad (1.3)$$

in three dimensions where  $X_i$  is the initial vector,  $x_i$  is the vector in the deformed geometry, and  $u_i$  is the displacement vector. Figure 1.5 displays the relationship between the undeformed and



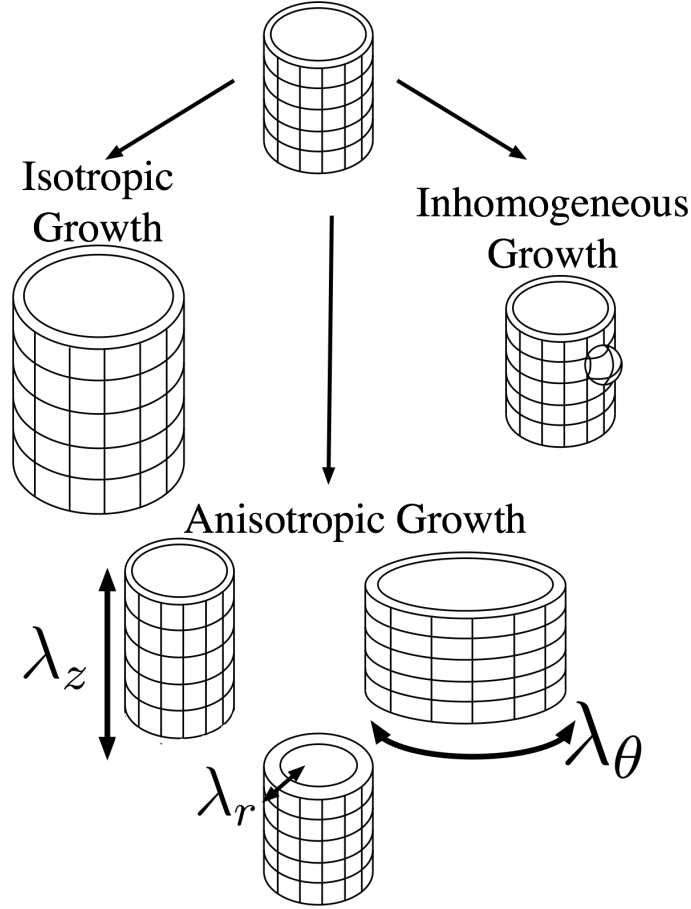


**Figure 1.4** Types of growth for isotropic materials, illustrated on a cylinder. Isotropic uniform growth is an enlargement of the original body. Uniform anisotropic growth is shown for each of the cylindrical coordinate directions  $(r, \theta, z)$  with stretch ratios  $\lambda_r, \lambda_\theta$ , and  $\lambda_z$ . Inhomogeneous isotropic growth, where the growth is different in certain areas of the domain, causes obvious shape change. We consider this geometry further in Chapter 2.

deformed bodies and their position and displacement vectors.

Formulating this as a mapping from the initial to the deformed configuration, the chain rule yields

$$dx_i = \frac{\partial x_i}{\partial x_j} dX_j, \quad (1.4)$$

where summation notation is used.

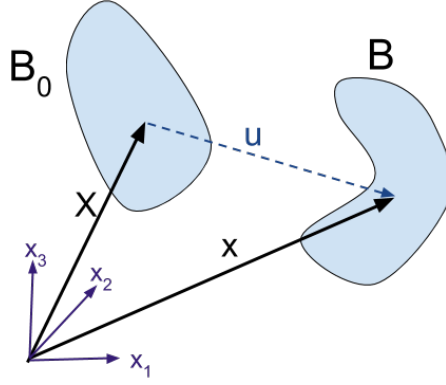


**Figure 1.5** Mapping of the initial configuration to the deformed configuration.  $B_0$  is the initial configuration with position vector  $X$ .  $B$  is the deformed configuration with position vector  $x$ . The initial position vector  $X$  can be mapped to the deformed configuration's position vector  $x$  using the displacement vector  $u$ .

More generally, we could consider the mapping to be

$$\mathbf{F}_{ij} = \frac{\partial x_i}{\partial X_j}, \quad (1.5)$$

where  $\mathbf{F}$  is a second-order tensor called the *deformation gradient tensor* that can be represented as

$$\mathbf{F} = \begin{bmatrix} \frac{\partial x_1}{\partial X_1} & \frac{\partial x_1}{\partial X_2} & \frac{\partial x_1}{\partial X_3} \\ \frac{\partial x_2}{\partial X_1} & \frac{\partial x_2}{\partial X_2} & \frac{\partial x_2}{\partial X_3} \\ \frac{\partial x_3}{\partial X_1} & \frac{\partial x_3}{\partial X_2} & \frac{\partial x_3}{\partial X_3} \end{bmatrix}. \quad (1.6)$$

Differentiating each of the above terms with respect to  $x_1, x_2, x_3$  yields the nine equations

$$\frac{\partial x_1}{\partial X_1} = \frac{\partial X_1}{\partial X_1} + \frac{\partial u_1}{\partial X_1} \quad \frac{\partial x_1}{\partial X_2} = \frac{\partial X_1}{\partial X_2} + \frac{\partial u_1}{\partial X_2} \quad \frac{\partial x_1}{\partial X_3} = \frac{\partial X_1}{\partial X_3} + \frac{\partial u_1}{\partial X_3} \quad (1.7)$$

$$\frac{\partial x_2}{\partial X_1} = \frac{\partial X_2}{\partial X_1} + \frac{\partial u_2}{\partial X_1} \quad \frac{\partial x_2}{\partial X_2} = \frac{\partial X_2}{\partial X_2} + \frac{\partial u_2}{\partial X_2} \quad \frac{\partial x_2}{\partial X_3} = \frac{\partial X_2}{\partial X_3} + \frac{\partial u_2}{\partial X_3} \quad (1.8)$$

$$\frac{\partial x_3}{\partial X_1} = \frac{\partial X_3}{\partial X_1} + \frac{\partial u_3}{\partial X_1} \quad \frac{\partial x_3}{\partial X_2} = \frac{\partial X_3}{\partial X_2} + \frac{\partial u_3}{\partial X_2} \quad \frac{\partial x_3}{\partial X_3} = \frac{\partial X_3}{\partial X_3} + \frac{\partial u_3}{\partial X_3}. \quad (1.9)$$

Notice that grouping all of the left hand sides of the equations together, we find the deformation

gradient tensor  $\mathbf{F}$  again. Grouping the first terms on the right hand sides gives the Kronecker-delta matrix

$$\delta_{ij} = \begin{bmatrix} 1 & 0 & 0 \\ 0 & 1 & 0 \\ 0 & 0 & 1 \end{bmatrix}. \quad (1.10)$$

The second terms from the right hand side of each of the nine equations are always the derivatives of the displacement with respect to a coordinate direction, as shown

$$\begin{bmatrix} \frac{\partial u_1}{\partial X_1} & \frac{\partial u_1}{\partial X_2} & \frac{\partial u_1}{\partial X_3} \\ \frac{\partial u_2}{\partial X_1} & \frac{\partial u_2}{\partial X_2} & \frac{\partial u_2}{\partial X_3} \\ \frac{\partial u_3}{\partial X_1} & \frac{\partial u_3}{\partial X_2} & \frac{\partial u_3}{\partial X_3} \end{bmatrix}. \quad (1.11)$$

Altogether, this yields the equation

$$\begin{bmatrix} \frac{\partial x_1}{\partial X_1} & \frac{\partial x_1}{\partial X_2} & \frac{\partial x_1}{\partial X_3} \\ \frac{\partial x_2}{\partial X_1} & \frac{\partial x_2}{\partial X_2} & \frac{\partial x_2}{\partial X_3} \\ \frac{\partial x_3}{\partial X_1} & \frac{\partial x_3}{\partial X_2} & \frac{\partial x_3}{\partial X_3} \end{bmatrix} = \begin{bmatrix} 1 & 0 & 0 \\ 0 & 1 & 0 \\ 0 & 0 & 1 \end{bmatrix} + \begin{bmatrix} \frac{\partial u_1}{\partial X_1} & \frac{\partial u_1}{\partial X_2} & \frac{\partial u_1}{\partial X_3} \\ \frac{\partial u_2}{\partial X_1} & \frac{\partial u_2}{\partial X_2} & \frac{\partial u_2}{\partial X_3} \\ \frac{\partial u_3}{\partial X_1} & \frac{\partial u_3}{\partial X_2} & \frac{\partial u_3}{\partial X_3} \end{bmatrix}. \quad (1.12)$$

Therefore the deformation gradient tensor can be concisely represented as

$$\mathbf{F}_{ij} = \delta_{ij} + \frac{\partial u_i}{\partial X_j}, \quad (1.13)$$

or, in more compact notation, as

$$\mathbf{F} = \mathbf{I} + \nabla u. \quad (1.14)$$

This means that  $\mathbf{F}$  describes the local, relative deformations of an object using the spatial derivative of the mapping from the undeformed basis to the deformed basis. In order to generalize, if we denote the deformation mapping by  $\chi$  and the define new bases  $\{e_1, e_2, e_3\}$  and  $\{E_1, E_2, E_3\}$  then

$$\mathbf{F} = \nabla \chi = \frac{\partial}{\partial x_j} (X_i e_i) \otimes E_j. \quad (1.15)$$

In morphoelasticity, when a volume element of the initial unstressed configuration  $B_0$  grows the size and orientation of the new volume element are described by the *growth deformation tensor*  $\mathbf{G}$ . This growth deformation tensor, when applied to the volume elements of  $B_0$ , transforms the initial configuration to a virtual unstressed state  $V$ . This virtual deformation, while unstressed, could result in incompatibilities in the continuum of the body. Figure 1.6 shows an example of such an incompatibility. Incompatibilities include self-intersection and other topological changes that make

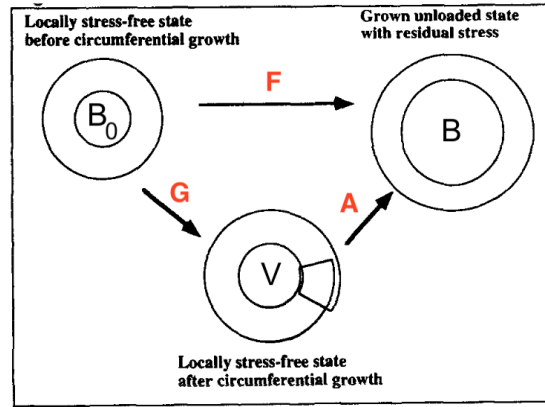


**Figure 1.6** Application of growth and elastic tensors to an initial configuration. Only considering the growth tensor  $\mathbf{G}$  can lead to incompatibilities in the body. Coupled with an elastic deformation tensor  $\mathbf{A}$  however, these incompatibilities are resolved. Both the growth tensor and the elastic deformation tensor in this order under right polar decomposition give the overall deformation tensor  $\mathbf{F}$ . Image adapted from [Rod94].

the unstressed deformed body an impossibility. However, introduction of an *elastic deformation tensor*  $\mathbf{A}$  resolves these.  $V$ , the virtual configuration, can be used to find both the elastic strains which ensure compatibility and the elastic stresses which ensure that the body loads are balanced and the boundary conditions are met. These are defined by the elastic deformation tensor  $\mathbf{A}$  which will map  $V$  to the new configuration  $B$ . Taken together we can write  $\mathbf{F} = \mathbf{A}\mathbf{G}$ .

Further description of the structures of  $\mathbf{F}$ ,  $\mathbf{A}$ , and  $\mathbf{G}$  can be found using the polar decomposition theorem. The polar decomposition theorem, as used in [Rod94], states that: For a second-order tensor  $\mathbf{F}$  such that  $\det \mathbf{F} \geq 0$ , there exist unique positive-definite symmetric tensors  $\mathbf{U}$  and  $\mathbf{V}$  and a

unique proper orthogonal tensor  $\mathbf{R}$  such that

$$\mathbf{F} = \mathbf{R}\mathbf{U} = \mathbf{V}\mathbf{R}. \quad (1.16)$$

Note that  $\mathbf{F}$  is not necessarily non-singular, as  $\det(\mathbf{F}) \geq 0$ . The positive symmetric tensors  $\mathbf{U}$  and  $\mathbf{V}$  are called the *left* and *right stretch tensors*, respectively. Their squares can easily be obtained from  $\mathbf{F}$  as follows:

$$\mathbf{F}^T \mathbf{F} = \mathbf{U}^2 = \mathbf{C}, \text{ the right Cauchy-Green tensor} \quad (1.17)$$

$$\mathbf{F} \mathbf{F}^T = \mathbf{V}^2 = \mathbf{B}, \text{ the left Cauchy-Green tensor.} \quad (1.18)$$

Since  $\mathbf{V} = \mathbf{R}\mathbf{U}\mathbf{R}^T$  (because orthogonal tensors' inverses are their transposes),  $\mathbf{U}$  and  $\mathbf{V}$  have the same eigenvalues. Because the eigenvalues of  $\mathbf{U}$  and  $\mathbf{V}$  are the same, this means that given either of the Cauchy-Green tensors, finding the square root of either  $\mathbf{C}$  or  $\mathbf{B}$ 's eigenvalues is the same as finding the eigenvalues,  $\lambda_i$  of either  $\mathbf{U}$  or  $\mathbf{V}$ . Using the eigenvectors  $u_i$  or  $v_i$  of  $\mathbf{U}$  or  $\mathbf{V}$  respectively allows us to reformulate  $\mathbf{F}$  another way in three dimensions as

$$\mathbf{F} = \sum_{i=1}^3 \lambda_i v_i \otimes u_i. \quad (1.19)$$

The polar decomposition theorem can also be utilized on  $\mathbf{G}$  to guarantee that it can be symmetrized. If we have an  $\mathbf{F}$  that is known then  $\mathbf{A}$  and  $\mathbf{G}$  are not unique. We could, through the polar decomposition theorem, decompose  $\mathbf{G}$ , instead of  $\mathbf{F}$ , into

$$\mathbf{G} = \mathbf{R}_G \mathbf{U}_G, \quad (1.20)$$

where  $\mathbf{U}_G$  is a symmetric tensor and  $\mathbf{R}_G$  is an orthogonal tensor. In the morphoelastic models developed in this thesis, we will assume tissues are materially isotropic. In that case, the strain-energy density satisfies  $W(\mathbf{A}) = W(\mathbf{A}\mathbf{R})$  for any proper orthogonal tensor  $\mathbf{R}$ . Since  $\mathbf{F} = \mathbf{A}\mathbf{G}$  and  $\mathbf{G}$  can

be decomposed, we can state that

$$W(\mathbf{A}) = W(\mathbf{F}\mathbf{G}^{-1}), \quad (1.21)$$

$$= W(\mathbf{F}\mathbf{U}_G^{-1}\mathbf{R}_G^T), \quad (1.22)$$

$$= W(\mathbf{F}\mathbf{U}_G). \quad (1.23)$$

Because the elastic energy  $W$  of an isotropic material depends just on the symmetric part of the growth tensor  $\mathbf{G}$ , the deformation gradient tensor  $\mathbf{F}$  can be decomposed into an elastic deformation tensor and a symmetric growth tensor. This means that we will always consider  $\mathbf{G}$  to be symmetric for an isotropic material. Specific choices for the formulation of the strain-energy density function of a hyperelastic material will be described in detail in Section 1.4.3.

We can use the polar decomposition theorem in a different context to decouple growth from rotation. As described in [Rod94],  $\mathbf{G}$  decomposes into two pieces, the *growth stretch tensor*  $\mathbf{U}_g$  and the *rotation tensor*  $\mathbf{R}_g$ . The growth stretch tensor  $\mathbf{U}_g$  can be found by integrating the growth rate tensor over time, though in this thesis we do not grow bodies in time; rather, we consider a single time step. Without loss of generality, the rotation tensor  $\mathbf{R}_g$  can be considered the identity tensor because any rotation in the growth tensor can simply be incorporated into the elastic deformation tensor  $\mathbf{A}$  as shown by

$$\mathbf{F} = \mathbf{A}\mathbf{G}, \quad (1.24)$$

$$= \mathbf{A}\mathbf{R}_g\mathbf{U}_g, \quad (1.25)$$

$$= \hat{\mathbf{A}}\mathbf{U}_g, \quad (1.26)$$

where  $\hat{\mathbf{A}}$  can be considered new elastic deformation tensor and  $\mathbf{G} \equiv \mathbf{U}_g$ .

However,  $\mathbf{G}$  merits a still closer look. The growth deformation tensor  $\mathbf{G}$  describes how individual volume elements change their unstressed size, shape, and orientation. Note that if the determinant of the growth tensor  $J_G = 1$ , there is no change of volume between the initial unstressed configu-

ration and the new configuration, but shape change could still have occurred. To describe  $\mathbf{G}$  for implementation in our models, we also needed to define a growth stretch ratio  $\lambda$ . This allows our stretch ratios to be considered  $\lambda_{ij} = 1 + \epsilon_{ij}$ , where  $\epsilon_{ij}$  is the strain in the  $ij$  direction. In Cartesian coordinates this allows us to write  $\mathbf{G}$  as

$$\mathbf{G} = \begin{bmatrix} \lambda_{xx} & \lambda_{xy} & \lambda_{xz} \\ \lambda_{yx} & \lambda_{yy} & \lambda_{yz} \\ \lambda_{zx} & \lambda_{zy} & \lambda_{zz} \end{bmatrix}. \quad (1.27)$$

Further details can be found in Section 3.1.

Another essential tensor in our model framework is the Cauchy stress tensor  $\mathbf{T}$ . The Cauchy stress tensor  $\mathbf{T} = n\sigma$ , where  $n$  is the normal vector and  $\sigma$  is stress, describes stresses on a body and allows us to write the equation of motion

$$\nabla \cdot \mathbf{T} + \rho b = \rho v, \quad (1.28)$$

where  $\rho$  is the mass density, and  $v$  the velocity. In this thesis, we ignore any body forces so  $b$  is 0 and because we assume our tissue's movement is only due to growth,  $v = 0$ . Therefore the equation of motion for our models is

$$\nabla \cdot \mathbf{T} = 0. \quad (1.29)$$

The Cauchy stress tensor  $\mathbf{T}$  is symmetric so  $\mathbf{T} = \mathbf{T}^T$ . The Cauchy stress tensor and the elastic deformation tensor  $\mathbf{A}$  relate through the strain-energy density function  $W$ ,

$$\mathbf{T} = J_A^{-1} \mathbf{A} \frac{\partial W}{\partial \mathbf{A}} - p \mathbf{1}, \quad (1.30)$$

where  $J_A = \det(\mathbf{A})$ . In this thesis we assume that the tissues are materially incompressible, giving  $J_A = 1$ . If the material is compressible,  $p = 0$ .

### 1.4.2 Continuum Mechanics

Mechanics and its interaction with gene signaling are essential to development and growth. Specifically we consider the *kinematics* of the growing body to be an important aspect. Kinematics as defined by [Bla17] is the term for the geometric transformations that quantify morphogenetic change without reference to force. We are especially focused on describing the stretch ratios of the growing organs as defined by the *strain*. While there are many mathematical formulations for strain, it can be simply defined as the difference due to deformation of a domain relative to its original configuration. Strain is a unitless measure. *Stress* is a description of the internal forces per area that occur between neighboring particles in a material and its unit is commonly given as Pascals. In simple 1-D cases, stress is linearly proportional to strain using a stiffness constant, usually Young's modulus. To properly formulate the nonlinear large-strain 3-D system of partial differential equations governing the mechanics of growth, we must consider the morphoelasticity and hyperelasticity equations and relate them to the standard continuity and balance equations with careful attention to the stresses and strains from growth.

#### 1.4.2.1 Solid Mechanics

Following our previously established theory from [Rod94] explained in Section 1.4.1, we also need to include the framework of solid mechanics. We give the standard time dependent equations, however for our modeling purposes we only consider the mechanics at steady state as will be further clarified in Chapter 2. To begin, we consider the continuity equation

$$\frac{\partial \rho}{\partial t} + \nabla \cdot j = c - d, \quad (1.31)$$

where  $\rho$  is the mass density,  $j$  is the flux in the system,  $c$  is a source of mass, and  $d$  is a sink. We must consider changes in mass as the growing organs may experience unbalanced mitosis and apoptosis. If mass is perfectly conserved and the density does not change with time the Equation



1.31 simplifies to

$$\nabla \cdot (\rho u) = 0. \quad (1.32)$$

We can also define the mass rate of growth as

$$\dot{m} = \rho \operatorname{div} v, \quad (1.33)$$

assuming that the mass density  $\rho$  is constant and uniform everywhere. Here,  $m$  is the mass and  $v$  is the growth velocity. The rate of unit tissue volume change is then described as

$$\frac{dV}{dt} = \operatorname{div} v = \operatorname{tr}(\mathbf{D}_g), \quad (1.34)$$

where  $\mathbf{D}_g$  is the rate of growth tensor.  $\mathbf{D}_g$  is then related to the growth stretch tensor by

$$\mathbf{D}_g = \frac{1}{2}(\dot{\mathbf{U}}_g \mathbf{U}_g^{-1} + \mathbf{U}_g^{-1} \dot{\mathbf{U}}_g). \quad (1.35)$$

Recall that the growth stretch tensor  $\mathbf{U}_g$  is the non-rotational tensor from  $\mathbf{G}$ 's decomposition and without loss of generality this can be considered  $\mathbf{G}$  as shown previously in Equation 1.24, stating

$$\mathbf{F} = \hat{\mathbf{A}} \mathbf{U}_g. \quad (1.36)$$

The deformation gradient tensor itself can be related to the deformation of the system given

$$\mathbf{F} = \mathbf{I} + \nabla u, \quad (1.37)$$

where  $\mathbf{I}$  is the identity tensor and  $\nabla u$  is the gradient of the displacement vector as previously expressed in Equation 1.14. The determinant of  $\mathbf{F}$ , representing the ratio between the current and initial volume, is written as  $J = \det(\mathbf{F})$ . Recall that  $\mathbf{F}$  can be multiplicatively decomposed into the elastic deformation tensor  $\mathbf{A}$  and the growth deformation tensor  $\mathbf{G}$ , or  $\mathbf{F} = \mathbf{A}\mathbf{G}$ .

The equation of motion, another balance equation, is represented in terms of the deformation

gradient tensor  $\mathbf{F} = \mathbf{A}\mathbf{G}$  with

$$0 = \nabla \cdot \mathbf{F}\mathbf{S} + F_V, \quad (1.38)$$

where  $F_V$  is the volume force vector and  $\mathbf{S}$  is the second Piola-Kirchhoff stress tensor. The second Piola-Kirchhoff stress tensor  $\mathbf{S}$  is symmetric and related to the Cauchy stress tensor  $\mathbf{T}$  which was used previously by the equation

$$\mathbf{S}^T = J_{\mathbf{F}} \mathbf{F}^{-1} \mathbf{T}. \quad (1.39)$$

$\mathbf{S}$  is sometimes referred to as the nominal stress and represents force over the original area, while  $\mathbf{T}$  is sometimes called the true stress and represents force over the deformed area. Consider the formulation of the deformation problems in terms of  $\mathbf{S}$ .  $\mathbf{S}$  is represented by

$$\mathbf{S} = \mathbf{S}_{\text{ext}} + \frac{\partial W}{\partial \mathbf{E}}, \quad (1.40)$$

where  $\mathbf{S}_{\text{ext}}$  is any external stress which in this thesis is assumed to be 0,  $W$  is the strain-energy density function which on the hyperelastic model chosen, and  $\mathbf{E}$  is the Green-Lagrange strain tensor. The Green-Lagrange strain tensor is given by

$$\mathbf{E} = \frac{1}{2}(\mathbf{F}^T \mathbf{F} - \mathbf{I}). \quad (1.41)$$

Because we assumed all materials to be incompressible and because material testing has shown a linear stress-strain relationship in developing epithelia for moderately large stretch [Tab08], we selected the neo-Hookean hyperelastic model. Hyperelasticity is further described in the following section.

### 1.4.3 Hyperelasticity

As defined in [Fun65], non-Hookean nonlinear materials can be generalized into three basic types. *Elastic materials* possess a homogeneous stress-free natural state and in a finite  $\delta$ -neighborhood of this state there exists a one to one correspondence between the Eulerian stress tensor and

the Almansi strain tensor. Often the Eulerian stress tensor is written directly as a function of the deformation gradient tensor  $\mathbf{F}$ , but this is only true for idealized materials. Materials are considered *hypoelastic* if the components of the stress rate with respect to time are a homogeneous linear function of the components of the rate of deformation and are not history dependent. We consider *hyperelastic* materials for our models. Materials are said to be hyperelastic if there exists a strain-energy density function where the rate of change of the strain-energy density with respect to time is equivalent to the rate of doing work using the stresses.

The objective of hyperelastic models is to describe the behavior of materials that do not satisfy a linear relationship between stress and strain and they are especially useful when strains are not infinitesimal. Given infinitesimal strains, many materials' stress-strain relationships are approximately linear but soft tissues typically undergo large strains even without growth; so, we cannot rely upon linear elastic theory as an accurate approximation. We use the notation and framework as defined in [Hac18]. The majority of widely used hyperelastic models relate to our morphoelastic framework through the right Cauchy deformation tensor  $\mathbf{C}$ . The principal invariants  $I_1$ ,  $I_2$ , and  $I_3$  of the right Cauchy deformation tensor as defined in Equation 1.17 are used in many descriptions of the strain-energy density function. They are defined in summation notation as

$$I_1 = \text{trace}(\mathbf{C}) = \mathbf{C}_{ii}, \quad (1.42)$$

$$I_2 = \frac{1}{2} \left( I_1^2 - \mathbf{C}_{ij} \mathbf{C}_{ji} \right), \quad (1.43)$$

$$I_3 = \det(\mathbf{C}). \quad (1.44)$$

#### 1.4.3.1 Neo-Hookean

The simplest hyperelastic model is neo-Hookean. This model describes the strain-energy density function  $W$  as being

$$W = \frac{\mu}{2} (I_1 - 3), \quad (1.45)$$

where  $\mu$  is the Lamé coefficient representing the shear modulus in continuum mechanics and where  $3\mu$  is the Young's modulus. This model can be used for predicting the behavior of materials undergoing large deformation whose stress-strain relationship is not necessarily linear. The neo-Hookean model is a simplified form of the Mooney-Rivlin hyperelastic model. We chose to start simply with a one parameter hyperelastic model in order to focus more on other aspects of the problems.

#### 1.4.3.2 Mooney-Rivlin

The Mooney-Rivlin hyperelastic model is well-defined in situations where the material is nearly incompressible or when the bulk modulus of a material is a few orders of magnitude larger than the shear modulus. This model is defines the strain-energy density function to be

$$W = \frac{C_1}{2}(I_1 - 3) + \frac{C_2}{2}(I_2 - 3), \quad (1.46)$$

where for small strains  $2(C_1 + C_2)$  is the shear modulus  $\mu$  and  $6(C_1 + C_2)$  is the Young's modulus. With the bulk and shear moduli difficult to determine in soft, developing tissues, we decided against using this model.

#### 1.4.3.3 Fung

For strain-stiffening materials especially for soft biological materials like arteries, a Fung hyperelastic model is often used. There are many different formulations of Fung hyperelastic models; we considered the one given in [Hac18]. In this case the strain-energy density function is considered to be

$$W = \frac{c}{2}(e^Q - 1) + \frac{K}{2} \left( \frac{(J_A)^2 - 1}{2} - \ln J_A \right), \quad (1.47)$$

where  $J_A$  is the determinant of the elastic deformation tensor,  $K$  is the bulk modulus,  $c$  is a material property, and  $Q$  is a function of the reduced Green-Lagrange strain tensor  $\mathbf{E}$ . For soft tissues, strain stiffening typically occurs around 30% strain [Fun84]. However, given that this model requires more

parameters, we instead used the neo-Hookean hyperelastic model.

## 1.5 Summary of Morphoelastic Framework

Collecting the equations developed in this chapter together into an overarching framework we have

$$\mathbf{F} = \mathbf{A}\mathbf{G} = \nabla\chi \quad \text{deformation gradient tensor} \quad (1.48)$$

$$\frac{\Delta V}{V} = \det(\mathbf{G}) \quad \text{volume change equation} \quad (1.49)$$

$$\text{div}\mathbf{T} = 0 \quad \text{equation of motion} \quad (1.50)$$

$$\mathbf{T} = \mathbf{T}^T = J^{-1}\mathbf{F}\frac{\partial W}{\partial \mathbf{F}} - p\mathbf{1} \quad \text{constitutive law} \quad (1.51)$$

$$W = \frac{\mu}{2}(I_1 - 3) \quad \text{Neo-Hookean strain-energy density function.} \quad (1.52)$$

These equations, while not a complete list of every relation, are the most essential to our morphogenetic framework and will be referenced in later chapters. An alternative formulation with respect to the reference variables can be found in [Gor17]. The growth tensor  $\mathbf{G}$  is an input to our system and will be defined differently for the two systems developed in Chapters 4 and 5.  $\mathbf{G}$  will be explained in further detail in these chapters as their individual local coordinate systems are established. Tables 1.1-1.5 list all tensor, parameter, variable, and geometry names.

The rest of this dissertation is organized as follows. Chapter 2 establishes the details of the solid and shell mechanics and gives the analytical solutions to a few examples. Chapter 3 describes the implementation and verification of our model systems. In Chapter 4, we apply our modeling framework to test different hypotheses on the causes of stomach bending using solid mechanics. In Chapter 5, for different local regions of interest we solve a morphogen transport problem to inform the growth of a lung tubule using shell mechanics to test hypotheses relating morphogen flux distributions to epithelial shape changes. Chapter 6 contains a discussion of our results and some ideas for further work.

**Table 1.1** Tensors in morphoelastic framework. All tensors in this document are represented as bold characters where possible.

Symbol	Description
<b>F</b>	deformation gradient tensor
<b>A</b>	elastic deformation tensor
<b>G</b>	growth tensor
<b>R</b>	proper orthogonal tensor
<b>U<sub>G</sub></b>	growth stretch tensor
<b>R<sub>G</sub></b>	growth rotation tensor
<b>T</b>	Cauchy stress tensor
<b>S</b>	second Piola-Kirchhoff stress tensor
<b>C</b>	right Cauchy-Green deformation tensor
<b>B</b>	left Cauchy-Green deformation tensor
<b>E</b>	Green-Lagrange strain tensor
$\epsilon_{\text{th}}$	thermal strain tensor
<b>U</b>	left stretch tensor
<b>V</b>	right stretch tensor
<b>D<sub>g</sub></b>	rate of growth tensor
<b>I</b>	identity tensor
$\epsilon$	Cauchy strain
$\sigma$	stress

**Table 1.2** Vectors in morphoelastic framework.

Symbol	Description
$v$	velocity
$u$	displacement
$X$	reference position in the initial configuration
$x$	reference position in the deformed configuration
$e_i$	basis vectors
$E_i$	alternative basis vectors
$n$	normal vector
$F_V$	volume force vector

**Table 1.3** Variables and functions in morphoelastic framework.

Symbol	Description
$\lambda$	stretch ratio
$J_D$	determinant of tensor <b>D</b>
$W$	strain-energy density function
$I_i$	invariants of <b>C</b> where i=1,2,3
$b$	body force
$c$	mass increase rate
$d$	mass decrease rate
$m$	mass
$t$	time
$\chi$	mapping from $X$ to $x$

**Table 1.4** Parameters in morphoelastic framework.

Symbol	Description
$p$	pressure
$K$	bulk modulus
$\mu$	Lamé coefficient
$\rho$	mass density

**Table 1.5** Geometries in morphoelastic framework.

Symbol	Description
$B_0$	initial configuration
$B$	deformed configuration
$V$	virtual configuration

## CHAPTER

# 2

## DETAILS OF MECHANICS

### 2.1 Solid Mechanics

In this dissertation, our models are not time-dependent but rather are focused on the deformations that result from specified growth strains as inputs. We used the variables and parameters described in Table 2.1. Following the notation in [Gor17], a complete closed time-independent model for morphoelasticity can be given by

$$x = X + u \quad \text{displacement} \quad (2.1)$$

$$\mathbf{F} = \mathbf{I} + \nabla u \quad \text{deformation gradient} \quad (2.2)$$

$$\mathbf{F} = \mathbf{A}\mathbf{G} \quad \text{decomposition} \quad (2.3)$$



$$J_{\mathbf{A}} = \det(\mathbf{A}) = 1 \quad \text{elastic incompressibility} \quad (2.4)$$

$$\mathbf{C} = \mathbf{F}^T \mathbf{F} \quad (2.5)$$

$$\mathbf{I}_1 = \text{trace}(\mathbf{C}) \quad (2.6)$$

$$\nabla \cdot \mathbf{T} = 0 \quad \text{equation of motion} \quad (2.7)$$

$$\mathbf{T} = \mathbf{T}^T \quad \text{constitutive law} \quad (2.8)$$

$$\mathbf{T} = J_{\mathbf{A}}^{-1} \mathbf{A} \frac{\partial W}{\partial \mathbf{A}} - p \mathbf{I} \quad \text{constitutive law} \quad (2.9)$$

$$W = \frac{\mu}{2} (\mathbf{I}_1 - 3) \quad \text{Neo-Hookean constitutive law,} \quad (2.10)$$

where  $x$  is a dependent variable, all gradients are taken with respect to the material coordinates  $X$ , and  $\mathbf{G}(X)$  will be an input dependent on modeling assumptions for each specific model and will be developed in Chapters 4 and 5. Note that the symmetry of the Cauchy stress tensor  $\mathbf{T}$  in Equation 2.8 simplifies the system. To ensure continuity, we also consider the set of material points of the

**Table 2.1** Variables and Parameters used in morphoelastic solid mechanics framework.

Symbol	Description	Type	Type
$X$	material coordinate	IV	vector
$x$	spatial coordinate	DV	vector
$u$	displacement	DV	vector
$\mathbf{F}$	deformation gradient tensor	DV	tensor
$\mathbf{A}$	elastic deformation tensor	DV	tensor
$\mathbf{C}$	right Cauchy-Green deformation tensor	DV	tensor
$\mathbf{T}$	Cauchy stress tensor	DV	tensor
$W$	strain energy density function	DV	scalar
$I_1$	first invariant of $\mathbf{C}$	DV	scalar
$p$	pressure	DV	scalar
$\mathbf{G}$	growth deformation tensor	P	tensor
$\mu$	shear modulus	P	scalar
$J_{\mathbf{A}}$	determinant of $\mathbf{A}$	P	scalar

initial configuration  $B_0$  which deform to become a new volume  $B$  as given by

$$\int_B dV = \int_{B_0} J_{\mathbf{F}} dV_0, \quad (2.11)$$

where  $J_{\mathbf{F}} = \det(\mathbf{F})$ ,  $V$  is the deformed volume, and  $V_0$  is the initial volume. Equation 2.3 is essential to all of our models. We implement specific choices of the growth tensor  $\mathbf{G}$  depending on each of our applications. Boundary conditions for each model are in general no stress on any surface,  $\boldsymbol{\sigma} \cdot \hat{\mathbf{n}} = 0$ , along with specified locations of no displacement for each model to ensure a unique solution to our system. A general overview of the components in our modeling systems is shown in Figure 2.1. Further discussion of nonlinear mechanics can be found in [Hol00], [Fer99], [TN92]. With this modeling framework in place, we discuss several simple cases of growth in the following sections.

### 2.1.1 One-Dimensional Example

We found the analytical solution to this system in a one-dimensional example with an arbitrary shear modulus  $\mu$ . Consider a line segment whose length doubles, giving  $\mathbf{G} = 2$ . We set the boundary condition so that the segment is fixed on one end,  $u(0) = 0$  and that the external pressure  $p = 0$ . After doubling the length of the line segment the material coordinates and spatial coordinates have the relation  $x = 2X$ . Since  $x = X + u$ , this means  $u = X$  and we can now solve for all of our other variables as follows:

$$\mathbf{F} = 1 + \frac{\partial}{\partial X} u = 1 + \frac{\partial}{\partial X} X = 2, \quad (2.12)$$

$$\mathbf{F} = \mathbf{A}\mathbf{G} \implies 2 = (\mathbf{A})(2) \implies \mathbf{A} = 1, \quad (2.13)$$

$$\mathbf{C} = \mathbf{F}^T \mathbf{F} \implies \mathbf{C} = 4, \quad (2.14)$$

$$W = \frac{\mu}{2}(\mathbf{I}_1 - 3) \implies W = \frac{\mu}{2}(4 - 3) = \frac{\mu}{2}, \quad (2.15)$$

$$\mathbf{T} = J_{\mathbf{A}}^{-1} \mathbf{A} \frac{\partial W}{\partial A} - p \mathbf{I} \implies \mathbf{T} = \frac{\partial}{\partial A} \left( \frac{\mu}{2} \right) \implies \mathbf{T} = \mathbf{0}. \quad (2.16)$$

We can therefore conclude that our system has no residual stress.

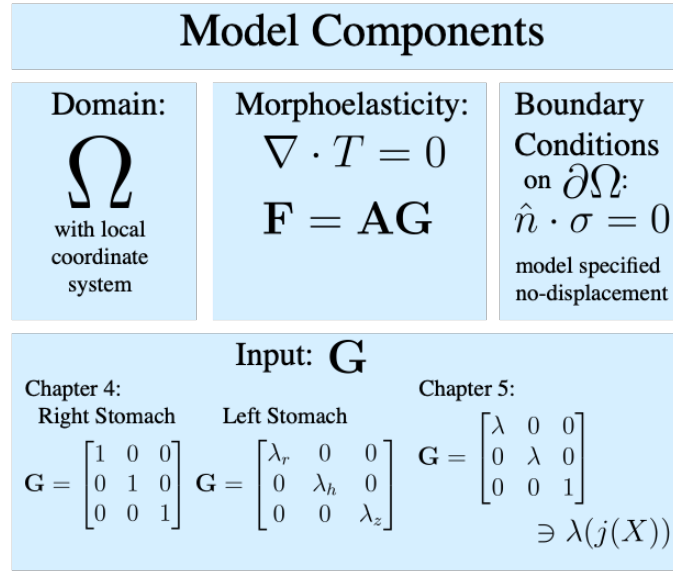


**Figure 2.1** Model components. For each of our models, we specify a domain  $\Omega$  and a local coordinate system. We use the framework of morphoelasticity in solids and shells, where we specify the growth tensor  $G$  as an input for each model. In particular for Chapter 5, the stretch ratio  $\lambda$  is a function of the flux  $j(X)$  which is determined via coupling to a steady state diffusion model. Unless otherwise specified all boundary surfaces are considered to be under no stress,  $\hat{n} \cdot \sigma = 0$ . Specific no displacement boundary conditions are given with each model. Because none of our models are time-dependent, there are no initial conditions.

### 2.1.2 Three-Dimensional Example

For a simpler, generalized case of our later stomach models, consider the domain to be a solid right cylinder in the standard cylindrical coordinate system  $X = (r, \theta, z)^T$  whose height and therefore volume we wish to double. We will consider the height of the cylinder to be  $H$ , the radius to be  $R$ , and because the cylinder is axisymmetric,  $0 \leq \theta \leq 2\pi$ . Since our model is not time dependent, we do not need to specify any initial conditions. However, our model framework contains spatial derivatives, so we must specify boundary conditions. Let  $\hat{u} = (u, v, w)^T$  be the displacement vector where  $u$  describes  $r$ -displacement,  $v$  describes  $\theta$ -displacement, and  $w$  describes  $z$ -displacement where  $u, v, w$  are functions of  $(r, \theta, z)$ . We pinned a point slightly off center of the bottom face

at  $(\alpha, 0, 0)$  to have no displacement, meaning  $u(\alpha, 0, 0) = 0$ ,  $v(\alpha, 0, 0) = 0$ , and  $w(\alpha, 0, 0) = 0$  as well as having no rotation. Additionally, we have a no stress boundary condition on all the surfaces, meaning  $\sigma \cdot \hat{n} = 0$  and a condition of no external pressure, so  $p = 0$ . We consider, as a modeling choice, the bottom face, where  $z = 0$ , to have no vertical displacement, meaning  $w(r, \theta, 0) = 0$ . We then model a doubling of volume by specifying the growth tensor

$$\mathbf{G}(r, \theta, z) = \begin{bmatrix} 1 & 0 & 0 \\ 0 & 1 & 0 \\ 0 & 0 & 2 \end{bmatrix}. \quad (2.17)$$

We can solve this system analytically as well. Given  $\mathbf{G}$  in Equation 2.17, we find that

$$u(r, \theta, z) = (0, 0, z) \quad (2.18)$$

$$\mathbf{F} = I + \nabla u = I + \begin{bmatrix} 0 & 0 & 0 \\ 0 & 0 & 0 \\ 0 & 0 & \frac{\partial}{\partial z} z \end{bmatrix} \quad (2.19)$$

$$\Rightarrow \mathbf{F} = \begin{bmatrix} 1 & 0 & 0 \\ 0 & 1 & 0 \\ 0 & 0 & 2 \end{bmatrix} \quad (2.20)$$

$$\mathbf{F}=\mathbf{A}\mathbf{G} \Rightarrow \begin{bmatrix} 1 & 0 & 0 \\ 0 & 1 & 0 \\ 0 & 0 & 2 \end{bmatrix} = \mathbf{A} \begin{bmatrix} 1 & 0 & 0 \\ 0 & 1 & 0 \\ 0 & 0 & 2 \end{bmatrix} \quad (2.21)$$

$$\Rightarrow \mathbf{A} = \begin{bmatrix} 1 & 0 & 0 \\ 0 & 1 & 0 \\ 0 & 0 & 1 \end{bmatrix} \quad (2.22)$$

$$\mathbf{C}=\mathbf{F}^T\mathbf{F} = \begin{bmatrix} 1 & 0 & 0 \\ 0 & 1 & 0 \\ 0 & 0 & 4 \end{bmatrix} \quad (2.23)$$

$$W = \frac{\mu}{2}(\mathbf{I}_1 - 3) \Rightarrow W = \frac{\mu}{2}(4 - 3) = \frac{\mu}{2}, \quad (2.24)$$

$$\mathbf{T} = J_{\mathbf{A}}^{-1} \mathbf{A} \frac{\partial W}{\partial A} - p \mathbf{I} \Rightarrow \mathbf{T} = \frac{\partial}{\partial A} \left( \frac{\mu}{2} \right) \Rightarrow \mathbf{T} = \mathbf{0}. \quad (2.25)$$

From this we can conclude that the resulting body is not residually stressed, and given that the determinant of  $\mathbf{F}$  is 2, the volume doubles. An example implementation in the finite elements solver COMSOL with 107358 degrees of freedom for a cylinder of radius 1 mm and height of 2 mm is shown in Figure 2.2, which shows both the deformed and undeformed shape. The analytical value for the new volume is  $V = 4\pi$ . The relative error of our calculated deformed volume  $\hat{V}$ , defined as  $\frac{V-\hat{V}}{V}$ , was 0.0002%.

## 2.2 Shell Mechanics

We implemented our shell models for the lung tubule in the finite elements solver COMSOL which uses an extension of Mindlin-Reissner plate theory to model shells with a MITC finite element method, described further in Appendix B. Following the model formulation in COMSOL, consider  $r$  to be the location of the undeformed shell midsurface,  $n$  to be a vector normal to that surface, and the local coordinate system  $(\eta_1, \eta_2, \eta_3)$  where  $\eta_1$  and  $\eta_2$  are locally orthogonal to each other and  $\eta_3$  is locally normal to the midsurface. If the deformed midsurface can be described by  $r + u$ , where  $u$

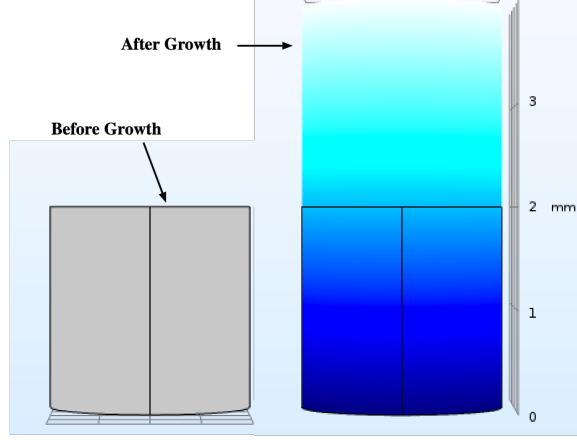


**Figure 2.2** Growth of a cylinder. For a cylinder of radius 1 mm and height of 2 mm, we set  $\text{diag}(\mathbf{G})=(1,1,2)$  in order to double the height. We had no stress boundary conditions on all the faces, no external pressure, and no displacement or rotation at an arbitrary point. To reflect our models in later chapters, we also chose to have no  $z$  displacement at on the bottom face of the cylinder. The error between our analytical volume and the calculated deformed volume  $\hat{V}$  was 0.0002%.

is a displacement vector and the deformed normal can be described by  $n + a$ , then the in-plane Green-Lagrange strain can be described by

$$\epsilon_{\alpha\beta} = \frac{1}{2} \left[ \frac{\partial}{\partial \eta_\alpha} (r + u + \eta_3(n + a)) \cdot \frac{\partial}{\partial \eta_\beta} (r + u + \eta_3(n + a)) - \frac{\partial}{\partial \alpha} (r + \eta_3 n) \cdot \frac{\partial}{\partial \eta_\beta} (r + \eta_3 n) \right] \quad (2.26)$$

$$= \gamma_{\alpha\beta} + \eta_3 \chi_{\alpha\beta} + (\eta_3)^2 \kappa_{\alpha\beta} \quad (2.27)$$

for  $\alpha, \beta = 1, 2$ . The transverse shear strain can be described by

$$\epsilon_{\alpha 3} = \epsilon_{3\alpha} = \frac{1}{2} \left[ \frac{\partial}{\partial \eta_\alpha} (r + u + \eta_3(n + a)) \cdot (n + a) - \frac{\partial}{\partial \eta_\alpha} (r + \eta_3 n) \cdot n \right] \quad (2.28)$$

$$= \zeta_\alpha + \eta_3 \omega_\alpha. \quad (2.29)$$

Each of the strain tensor parts are written specifically as

$$\gamma_{\alpha\beta} = \frac{1}{2} \left[ \frac{\partial u}{\partial \eta_\alpha} \frac{\partial r}{\partial \eta_\beta} + \frac{\partial r}{\partial \eta_\alpha} \frac{\partial u}{\partial \eta_\beta} + \frac{\partial u}{\partial \eta_\alpha} \frac{\partial u}{\partial \eta_\beta} \right], \quad (2.30)$$

$$\chi_{\alpha\beta} = \frac{1}{2} \left[ \frac{\partial r}{\partial \eta_\alpha} \frac{\partial a}{\partial \eta_\beta} + \frac{\partial a}{\partial \eta_\alpha} \frac{\partial r}{\partial \eta_\beta} + \frac{\partial u}{\partial \eta_\alpha} \frac{\partial n}{\partial \eta_\beta} + \frac{\partial n}{\partial \eta_\alpha} \frac{\partial u}{\partial \eta_\beta} + \frac{\partial u}{\partial \eta_\alpha} \frac{\partial a}{\partial \eta_\beta} + \frac{\partial a}{\partial \eta_\alpha} \frac{\partial u}{\partial \eta_\beta} \right], \quad (2.31)$$

$$\kappa_{\alpha\beta} = \frac{1}{2} \left[ \frac{\partial a}{\partial \eta_\alpha} \frac{\partial n}{\partial \eta_\beta} + \frac{\partial n}{\partial \eta_\alpha} \frac{\partial a}{\partial \eta_\beta} + \frac{\partial a}{\partial \eta_\alpha} \frac{\partial a}{\partial \eta_\beta} \right], \quad (2.32)$$

$$\zeta_\alpha = \frac{1}{2} \left[ \frac{\partial r}{\partial \eta_\alpha} \cdot a + \frac{\partial u}{\partial \eta_\alpha} \cdot n + \frac{\partial u}{\partial \eta_\alpha} \cdot a \right], \quad (2.33)$$

$$\omega_\alpha = \frac{1}{2} \left[ \frac{\partial n}{\partial \eta_\alpha} \cdot a + \frac{\partial a}{\partial \eta_\alpha} \cdot n + \frac{\partial a}{\partial \eta_\alpha} \cdot a \right]. \quad (2.34)$$

These are related to the membrane stress  $\sigma_m$ , the bending stress  $\sigma_b$ , the shear stress  $\sigma_s$ , and the in-plane stress  $\sigma_{\text{inplane}}$  via the equations

$$\sigma_m = \hat{\mathbf{C}}(\gamma - \epsilon_G), \quad (2.35)$$

$$\sigma_b = \frac{\hat{\mathbf{C}}\Phi}{2}(\chi - \epsilon_G), \quad (2.36)$$

$$\sigma_s = \tilde{z}\sigma_b, \quad (2.37)$$

$$\sigma_{\text{inplane}} = \sigma_m + \tilde{z}\sigma_b, \quad (2.38)$$

where  $\hat{\mathbf{C}}$  is the Cauchy stress tensor and  $\epsilon_G$  is the implemented growth strain. For our models in Chapter 5,  $\epsilon_G$  is a function of the local flux  $j(X)$  calculated via coupling to a steady state diffusion equation. The membrane force is then defined as

$$N = \Phi\sigma_m, \quad (2.39)$$

and the bending component is given by

$$M = \frac{\Phi^2}{6}\sigma_b, \quad (2.40)$$

and shear forces are described by

$$Q = \Phi \sigma_s. \quad (2.41)$$

This however does not encompass a complete shell theory. We further describe the theory, force balance, moment balance, and stress-strain relationships in the following section.

### 2.2.1 General Shell Theory

Shell equations follow from plate theory, extended to accommodate two directions of curvature. To simplify discussion, we ignore shear strains, which would yield different resultants. We followed similar methods from rods and beams, namely force and moment balancing, to formulate a simple model for shells. Following the notation and development in [Smi05], we began by considering a curvilinear coordinate system with the directions  $\alpha, \beta$ , and  $z$ . Here  $z$  is normal to the surface and  $z_n = 0$  will be the unperturbed middle surface. Additionally,  $\alpha$  and  $\beta$  follow the two principal curvatures as shown in Figure 2.3. Unit vectors in each of those directions are denoted as  $\hat{i}$  with subscripts denoting the direction.

With the two radii of curvature,  $R_\alpha$  denoting the curvature in the  $\alpha$  direction and  $R_\beta$  denoting the curvature in the  $\beta$  direction, the Lamé constants can be defined as

$$A^2 = \frac{\partial r}{\partial \alpha} \frac{\partial r}{\partial \alpha} \quad (2.42)$$

$$B^2 = \frac{\partial r}{\partial \beta} \frac{\partial r}{\partial \beta}. \quad (2.43)$$

Let external forces be defined by

$$\mathbf{f} = f_\alpha \hat{i}_\alpha + f_\beta \hat{i}_\beta + f_n \hat{i}_n, \quad (2.44)$$

and the displacements in the  $\alpha$ ,  $\beta$ , and  $z$  directions be given by  $u$ ,  $v$ , and  $w$  respectively. Force



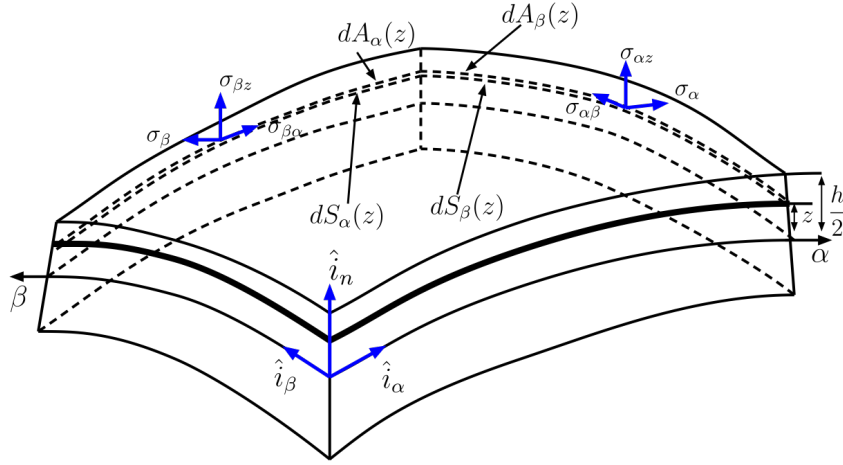


**Figure 2.3** Depiction of shell element. The  $n$  direction is locally normal to the shell midsurface, and the  $\alpha$  and  $\beta$  directions follow the directions of principal curvature, after [Smi05].

balancing in each direction when not dependent on time yields

$$\frac{\partial}{\partial \alpha}(BN_\alpha) + \frac{\partial}{\partial \beta}(AN_{\beta\alpha}) + \frac{\partial A}{\partial \beta}(N_{\beta\alpha}) - \frac{\partial B}{\partial \alpha}(N_\beta) + \frac{AB}{R_\alpha}Q_\alpha + ABf_\alpha = 0, \quad (2.45)$$

$$\frac{\partial}{\partial \beta}(AN_\beta) + \frac{\partial}{\partial \alpha}(BN_{\alpha\beta}) + \frac{\partial B}{\partial \alpha}(N_{\beta\alpha}) - \frac{\partial A}{\partial \beta}(N_\beta) + \frac{AB}{R_\beta}Q_\alpha + ABf_\beta = 0, \quad (2.46)$$

$$-\frac{AB}{R_\alpha}N_\alpha - \frac{AB}{R_\beta} + \frac{\partial}{\partial \alpha}(BQ_\alpha) + \frac{\partial}{\partial \beta}(AQ_\beta) + ABf_n = 0. \quad (2.47)$$

Moment balancing in the shell yields

$$\frac{\partial}{\partial \alpha}(BM_\alpha) + \frac{\partial}{\partial \beta}(AM_{\beta\alpha}) + \frac{\partial A}{\partial \beta}(M_{\alpha\beta}) - \frac{\partial B}{\partial \alpha}(M_\beta) - ABQ_\alpha + AB\hat{m}_\beta = 0, \quad (2.48)$$

$$\frac{\partial}{\partial \beta}(AM_\beta) + \frac{\partial}{\partial \alpha}(BM_{\alpha\beta}) + \frac{\partial B}{\partial \alpha}(M_{\beta\alpha}) - \frac{\partial A}{\partial \beta}(M_\alpha) - ABQ_\beta + AB\hat{m}_\alpha = 0, \quad (2.49)$$

$$N_{\alpha\beta} - N_{\beta\alpha} + \frac{M_{\alpha\beta}}{R_\alpha} - \frac{M_{\beta\alpha}}{R_\beta} = 0. \quad (2.50)$$

The shell model's general strain-displacement relations, where  $U$ ,  $V$ , and  $W$  denote displacements

at an arbitrary point on the shell, can be written as

$$\epsilon_\alpha = \frac{1}{1+z/R_\alpha} \left( \frac{1}{A} \frac{\partial U}{\partial \alpha} + \frac{V}{AB} \frac{\partial A}{\partial \beta} + \frac{W}{R_\alpha} \right), \quad (2.51)$$

$$\epsilon_\beta = \frac{1}{1+z/R_\beta} \left( \frac{1}{B} \frac{\partial V}{\partial \beta} + \frac{U}{AB} \frac{\partial B}{\partial \alpha} + \frac{W}{R_\beta} \right), \quad (2.52)$$

$$\epsilon_z = \frac{\partial W}{\partial z}, \quad (2.53)$$

$$\epsilon_{\alpha\beta} = \frac{A(1+z/R_\alpha)}{B(1+z/R_\beta)} \frac{\partial}{\partial \beta} \left[ \frac{U}{A(1+z/R_\alpha)} \right] + \frac{B(1+z/R_\beta)}{A(1+z/R_\alpha)} \frac{\partial}{\partial \alpha} \left[ \frac{V}{B(1+z/R_\beta)} \right], \quad (2.54)$$

$$\epsilon_{\alpha z} = \frac{1}{A(1+z/R_\alpha)} \frac{\partial W}{\partial \alpha} + A(1+z/R_\alpha) \frac{\partial}{\partial z} \left[ \frac{U}{A(1+z/R_\alpha)} \right], \quad (2.55)$$

$$\epsilon_{\beta z} = \frac{1}{B(1+z/R_\beta)} \frac{\partial W}{\partial \beta} + B(1+z/R_\beta) \frac{\partial}{\partial z} \left[ \frac{V}{B(1+z/R_\beta)} \right]. \quad (2.56)$$

Assuming displacements are linear in the thickness direction, the displacements at arbitrary points can be expressed as

$$U(\alpha, \beta, z) = u(\alpha, \beta) + z\theta_\alpha(\alpha, \beta), \quad (2.57)$$

$$V(\alpha, \beta, z) = v(\alpha, \beta) + z\theta_\beta(\alpha, \beta), \quad (2.58)$$

$$W(\alpha, \beta, z) = w(\alpha, \beta). \quad (2.59)$$

Thus the changes in curvature can be described by

$$\kappa_\alpha = \frac{1}{A} \frac{\partial \theta_\alpha}{\partial \alpha} + \frac{\theta_\beta}{AB} \frac{\partial A}{\partial \beta}, \quad (2.60)$$

$$\kappa_\beta = \frac{1}{B} \frac{\partial \theta_\beta}{\partial \beta} + \frac{\theta_\alpha}{AB} \frac{\partial B}{\partial \alpha}, \quad (2.61)$$

$$\kappa_{\alpha\beta} = \frac{A}{B} \frac{\partial}{\partial \beta} \left( \frac{\theta_\alpha}{A} \right) + \frac{B}{A} \frac{\partial}{\partial \alpha} \left( \frac{\theta_\beta}{B} \right) + \frac{1}{R_\alpha} \left( \frac{1}{B} \frac{\partial u}{\partial \beta} - \frac{v}{AB} \frac{\partial B}{\partial \alpha} \right) + \frac{1}{R_\beta} \left( \frac{1}{A} \frac{\partial v}{\partial \alpha} - \frac{u}{AB} \frac{\partial A}{\partial \beta} \right). \quad (2.62)$$

With no damping, external forces, or moments, the forces can be simplified to

$$N_\alpha = \frac{Yh}{1-\nu^2} \left[ e_\alpha + \nu e_\beta - \frac{h^2}{12} \left( \frac{1}{R_\alpha} - \frac{1}{R_\beta} \right) \left( \kappa_\alpha - \frac{e_\alpha}{R_\alpha} \right) \right], \quad (2.63)$$

$$N_\beta = \frac{Yh}{1-\nu^2} \left[ e_\beta + \nu e_\alpha - \frac{h^2}{12} \left( \frac{1}{R_\beta} - \frac{1}{R_\alpha} \right) \left( \kappa_\beta - \frac{e_\beta}{R_\beta} \right) \right], \quad (2.64)$$

$$N_{\alpha\beta} = \frac{Yh}{2(1+\nu)} \left[ e_{\alpha\beta} - \frac{h^2}{12} \left( \frac{1}{R_\alpha} - \frac{1}{R_\beta} \right) \left( \frac{\kappa_{\alpha\beta}}{2} - \frac{e_{\alpha\beta}}{R_\alpha} \right) \right], \quad (2.65)$$

$$N_{\beta\alpha} = \frac{Yh}{2(1+\nu)} \left[ e_{\alpha\beta} - \frac{h^2}{12} \left( \frac{1}{R_\beta} - \frac{1}{R_\alpha} \right) \left( \frac{\kappa_{\alpha\beta}}{2} - \frac{e_{\alpha\beta}}{R_\beta} \right) \right], \quad (2.66)$$

where the strains at an arbitrary point on the reference surface of the shell are defined by

$$e_\alpha = \frac{1}{A} \frac{\partial u}{\partial \alpha} + \frac{\nu}{AB} \frac{\partial A}{\partial \beta} + \frac{w}{R_\alpha}, \quad (2.67)$$

$$e_\beta = \frac{1}{B} \frac{\partial v}{\partial \beta} + \frac{u}{AB} \frac{\partial B}{\partial \alpha} + \frac{w}{R_\beta}, \quad (2.68)$$

$$e_{\alpha\beta} = \frac{A}{B} \frac{\partial}{\partial \beta} \left( \frac{u}{A} \right) + \frac{B}{A} \frac{\partial}{\partial \alpha} \left( \frac{v}{B} \right). \quad (2.69)$$

With no damping, external forces, or moments, the momentums in each direction can be simplified to

$$M_\alpha = \frac{Yh^3}{12(1-\nu^2)} \left[ \kappa_\alpha + \nu \kappa_\beta - \left( \frac{1}{R_\alpha} - \frac{1}{R_\beta} \right) e_\alpha \right], \quad (2.70)$$

$$M_\beta = \frac{Yh^3}{12(1-\nu^2)} \left[ \kappa_\beta + \nu \kappa_\alpha - \left( \frac{1}{R_\beta} - \frac{1}{R_\alpha} \right) e_\beta \right], \quad (2.71)$$

$$M_{\alpha\beta} = \frac{Yh^3}{24(1-\nu^2)} \left[ \kappa_{\alpha\beta} - \frac{e_{\alpha\beta}}{R_\alpha} \right], \quad (2.72)$$

$$M_{\beta\alpha} = \frac{Yh^3}{24(1-\nu^2)} \left[ \kappa_{\alpha\beta} - \frac{e_{\alpha\beta}}{R_\beta} \right]. \quad (2.73)$$

For our shell models, all shell surfaces are considered to be under no stress meaning  $\hat{n}\sigma = 0$ . For all of our specific geometry there exists a cut face of symmetry. At that location the shell surface also has a boundary condition of no normal displacement and no rotation. These conditions and

any additional modeling assumptions will be further clarified in Chapter 5. Further examples of growth, specifically inhomogeneous growth, for both the solid and shell framework can be found in Appendix A.

## CHAPTER

# 3

## IMPLEMENTATION & VERIFICATION

In this chapter, we discuss how we implemented our morphoelastic framework in the finite elements package COMSOL. We also verify our computational model, and consider some simple examples. We discuss how we implement growth strains and create a local coordinates system. We compare linear elastic and hyperelastic computational models to the analytical solution in simple shapes. We then model some simple examples with geometry and inputs more similar to those seen in later chapters.

### **3.1 COMSOL Implementation**

We implemented all of our models in the finite elements multiphysics partial differential equations package COMSOL 5.3, which is the first version to include multiplicative strain decomposition in its Structural Mechanics module, with built-in hyperelastic submodules. COMSOL handles creation of

complex geometries, has multiple meshing capabilities, can define coordinate systems, and does some basic visualization.

### 3.1.1 Implementing Growth

COMSOL does not have an interface specifically tailored to growth. However its Structural Mechanics module contains a thermal expansion submodule whose equations are identical in form to ours but with different definitions for the variables. The thermal expansion equation implemented in COMSOL is

$$\epsilon_{\text{th}} = \alpha_{ij}(T - T_{\text{ref}}), \quad (3.1)$$

for scalar temperatures  $T$  and  $T_{\text{ref}}$  where temperatures are given in degrees and  $\alpha$  is given in  $(^\circ)^{-1}$ . However, we can reinterpret both as dimensionless. The thermal expansion equation gives a strain tensor  $\epsilon_{\text{th}}$  where the thermal expansion coefficient tensor  $\alpha_{ij}$  can vary in each direction. Strains, which are related to stretch ratios, describe a relative change in a distance measure. For example, in one dimension a strain could be formulated as

$$\epsilon = \frac{l - l_0}{l_0} = \lambda - 1,$$

where strain is calculated as the change in length  $l$  from the original length  $l_0$  relative to  $l_0$ . This strain is called the *engineering strain* or *Cauchy strain*. While there are many formulations for strain, we will always be using engineering strain unless otherwise specified. Since we are calculating strain due to analogous thermal expansion, this can describe a length change or growth. With thermal expansion as a surrogate for the mechanism driving growth, consider the thermal stretch ratio  $\lambda_{\text{th}}$  to be the only component of the stretch. For isotropic growth in an isotropic material this would mean the stretch ratio can be formulated as

$$\lambda_{\text{th}} = 1 + \alpha(T - T_{\text{ref}}), \quad (3.2)$$

where  $\alpha_{ij}(T - T_{\text{ref}})$  is the thermal strain in the  $i j$  direction. This means that the growth tensor  $\mathbf{G}$  can be represented as a diagonal tensor in a coordinate system corresponding to the directions of growth where the diagonal entries are all  $\lambda_{\text{th}}$ , which would make  $\det(\mathbf{G}) = J_G = \lambda_{\text{th}}^3$  the volumetric growth ratio. We also need to consider anisotropic growth in our isotropic materials. This is achieved by allowing our imposed  $\alpha$  to differ in each of the three directions. So the growth tensor with anisotropy oriented in the Cartesian directions that we implement through COMSOL becomes

$$\mathbf{G} = \mathbf{I} + \epsilon_{\text{th}} = \begin{bmatrix} 1 + \alpha_1(T - T_{\text{ref}}) & 0 & 0 \\ 0 & 1 + \alpha_2(T - T_{\text{ref}}) & 0 \\ 0 & 0 & 1 + \alpha_3(T - T_{\text{ref}}) \end{bmatrix}, \quad (3.3)$$

where each  $\alpha_i$  is a user input, as are  $T$  and  $T_{\text{ref}}$ . For our modeling purposes,  $T - T_{\text{ref}}$  was always held at 1 and  $\alpha_i$  described the individual growth strains we modeled. A parametric sweep of increasing values of  $T$  could be used as a short-time surrogate for finite time steps as the tissue continues to grow, but we did not do that here.

### 3.1.2 Local Coordinate Systems

For most morphogenetic systems, standard Cartesian coordinates are a poor choice. The stomach tube grows radially, longitudinally, and axially and these may be biologically distinct processes worth modeling. However, even polar coordinates for the stomach tube is a problematic choice, because even the early stomach is not a simple cylinder. The lung is even more geometrically complex. To adequately describe our inputs and shape changes, we work in a local coordinate system. Using a local curvilinear coordinate system can make it easier to, for example, define boundary conditions that follow a curved surface, or define anisotropic growth in a biologically natural direction.

COMSOL has a built-in method to determine local coordinates relative to surfaces. To find the first vector of our new coordinate system in COMSOL, we first solve the Laplace equation,  $\nabla^2 q = 0$ , on the domain with an "inlet" surface, "outlet" surface, and no flux at any of the other boundaries

and then compute the resulting vector field  $-\nabla q$  which describes the direction of gradient following the curve of our domain. Without loss of generality, we consider the inlet surface to have  $q = 1$  and the outlet surface to have  $q = 0$ , and the remaining surfaces to have the condition  $n \cdot \nabla q = 0$ . In two dimensions, the first new local coordinate direction follows the direction of the gradient of  $q$  and the second local coordinate direction follows the level curves of  $q$ . An example of this system and its boundary conditions is shown in Figure 3.1. COMSOL computes the solution to the Laplace equation given these boundaries and calculates a vector field. An example computed vector field from COMSOL can be found in Figure 3.2. Vectors from this field create the first basis vector,  $v_1$  of our new coordinate system. In three dimensions, we then user-define a second vector  $v_2$  and using the cross product of our first two basis vectors we calculate the third basis vector. If we call our new basis vectors  $(e_1, e_2, e_3)$ , their relationship can be described as

$$e_1 = v_1, \quad (3.4)$$

$$e_2 = v_2 - (v_2 \cdot e_1)e_1, \quad (3.5)$$

$$e_3 = e_1 \times e_2, \quad (3.6)$$

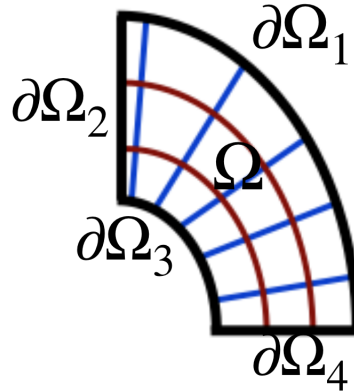


**Figure 3.1** Domain and boundary conditions used to solve for local coordinate systems in an example 2D domain. We solve  $\nabla^2 q = 0$  in the domain  $\Omega$ . There are no flux boundary conditions,  $n \cdot \nabla q = 0$ , on  $\partial\Omega_1$  and  $\partial\Omega_3$ . Without loss of generality at  $\partial\Omega_4$   $q = 1$  and at  $\partial\Omega_2$   $q = 0$ .



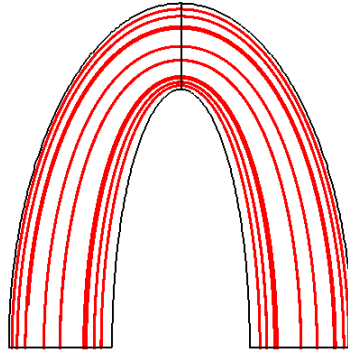


**Figure 3.2** Curves following the direction of the gradient of  $q$  for calculating local coordinates. We calculated the curves of an example vector field from the Laplace equation with an inlet  $q = 1$  on the bottom right face and an outlet  $q = 0$  on the bottom left face. Notice how the calculated curves follow the curve of the domain.

where  $v_1$  is from the calculated vector field and  $v_2$  was our user-defined vector. Our completed vector system can be seen in Figure 3.3.

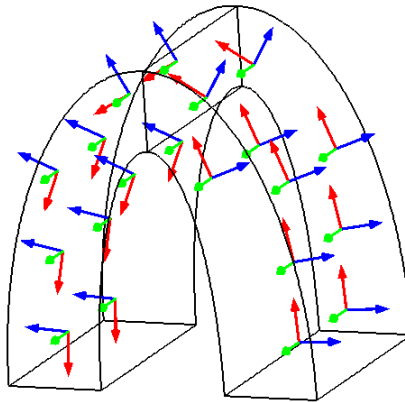


**Figure 3.3** Local curvilinear coordinate system. Our local curvilinear coordinate system was calculated in this example for half of our stomach geometry seen later in Chapter 4. The first basis vector, in red, follows the curves of the domain, the second basis vector, in green, is in the  $z$  direction, and the third, in blue, is locally orthogonal to both the previous vectors.

### 3.1.3 Hyperelasticity

We also needed to specify our hyperelastic model choice to be neo-Hookean as assumed in Section 1.4.3.1. The strain-energy density function for the neo-Hookean model as described in COMSOL is

$$W_s = \frac{1}{2}\mu(I_1 - 3) + \frac{1}{2}\kappa(J_{el} - 1)^2, \quad (3.7)$$

where  $I_1$  is the first principal invariant, or the trace, of the right Cauchy Green stress tensor. The second term of Equation 3.7 is given by COMSOL's specific compressible formulation of the neo-Hookean model and involves  $\kappa$ , a compressibility constant, and  $J_{el}$ , the determinant of the elastic deformation tensor which we refer to in this thesis as  $J_A$ . Because we assumed our material was elastically incompressible  $\kappa = 0$ , so our strain-energy density function simplifies directly to the standard incompressible neo-Hookean strain-energy density function

$$W_s = \frac{1}{2}\mu(I_1 - 3), \quad (3.8)$$

of Section 1.4.3.1. The Lamé parameter  $\mu$  is also user specified. So as follows from Section 1.4, with our  $\mathbf{G}$  which will be specified for each individual model,  $W$ , and boundary conditions specified for each individual model in the following chapters we can solve our system of PDEs using the finite elements package COMSOL. Further details on COMSOL can be found in [Com]. Further modeling assumptions and parameters will be in Chapters 5-6.

## 3.2 Model Verification

To ensure the accuracy of our model implementation in COMSOL, we considered problems we could solve analytically as well as computationally, in order to compare the results. In order to ensure that our model implementation was accurately describing both mitosis and cell rearrangement, we initially separated the processes to individually test the accuracy of each. To represent pure cell rearrangement, the tissue only undergoes a change in shape but not in the overall volume, so  $\det(\mathbf{G})$

= 1. For cell division, we want to be able to control exactly how much change there was in any given direction, so  $\det(\mathbf{G}) > 1$ . We started with test problems in simple domains whose solutions we could calculate analytically as well as computationally.

### 3.2.1 Two-Dimensional Tests

We began with two-dimensional domains whose areas would be simple to calculate analytically. Because we wanted to be able to solve for the new area analytically, for the first round of COMSOL verification tests our domain was a 1 mm by 1 mm square with a fixed boundary on the left edge where the x-displacement is 0 and all edges were unstressed, as seen in Figure 3.4. A solvable analytical problem that could be easily tested would be growth in just one direction, so we implemented a growth tensor

$$\mathbf{G} = \begin{bmatrix} 1.1 & 0 \\ 0 & 1 \end{bmatrix}. \quad (3.9)$$

This would mean our stretch ratio in the x-direction is 1.1 and the y-direction is 1. A stretch ratio of 1.1 means  $\alpha_1(T - T_{\text{ref}}) = 0.1$ , so we therefore implemented our x-direction stretch ratio using a 10% thermal strain. A stretch ratio of 1 in the y-direction means the length in the y-direction remains constant. Analytically we expect a new area of 1.1 mm<sup>2</sup>, where the width becomes 1.1 mm and the height remains 1 mm.

With this geometry and growth tensor, we tested the accuracy of the hyperelastic model given various parameters and strains and compared it to the linear elastic model to ensure that we chose the simplest possible, yet still accurate, model. To be consistent with the linear elastic model, Lamé coefficients for the hyperelastic model were calculated from the Young's modulus and Poisson's ratio using the following

$$\mu = \frac{E}{2(1 + \nu)}, \quad (3.10)$$

which can be found in [CB11]. The Young's modulus was held constant at 100 Pa. We tested Poisson's

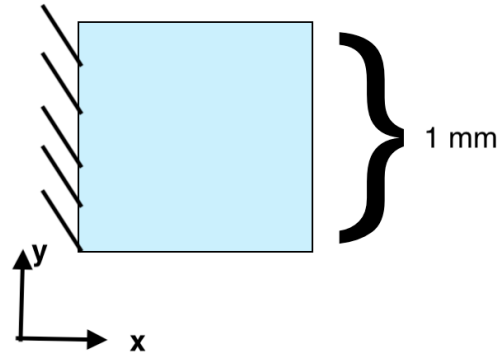


**Figure 3.4** Example domain with a clear analytical solution. We tested the accuracy of our model in a simple 1 mm by 1 mm square whose new dimensions we would be able to calculate analytically. This two-dimensional geometry was used for many tests to compare the hyperelastic model to the linear elastic model and check the accuracy of each.

ratios of 0.1, 0.2, 0.3, 0.4, and 0.49 for the linear elastic model. However, introducing a Poisson's ratio of 0.5 computationally can and often did create singularities and so it is not included in the reported results. We also calculated the Lamé coefficients that correspond to these  $\nu$  values to directly compare the hyperelastic model results. In the hyperelastic model we tested Lamé parameters of 45.45, 41.66, 38.46, 35.714, and 33.56 Pa. Even when  $\nu \neq 0.5$ , since the strain is from growth, there is no volume change. The hyperelastic model remains accurate in this small strain test of 10% regardless of tested parameter values as can be seen in Table 3.1, where  $\hat{x}$  is new width,  $\hat{y}$  is the new height, and  $\hat{A}$  is the new area.

The results of a mesh refinement study for this hyperelastic experiment holding the Lamé coefficient at  $\mu = 33.56$  Pa, equivalently Poisson's ratio  $\nu = 0.49$ , are shown in Table 3.2. Change in mesh size did not result in a change of accuracy for our simple experiment. A more complex geometry would likely need a finer mesh due to numerical problems arising from sharp corners and element inversions. Finer meshes will be used in our model geometries in later chapters to resolve any possible issues.

Holding  $\nu = 0.4$  and  $E = 100$  Pa, we increased the given strain, and therefore stretch ratio, in the

**Table 3.1** Lamé coefficients  $\mu$  for each Poisson's ratio  $\nu$ . For use in comparing the hyperelastic model, corresponding Lamé coefficients  $\mu$  for each Poisson's ratio  $\nu$ , used in the linear elastic model, were calculated from Equation 3.10. However, this had no effect on the outcome of the morphoelastic model. Regardless of the parameters, the model remained at 0% error. The new length in  $x$ , formerly 1mm, is represented by  $\hat{x}$ . The new length in  $y$ , formerly 1 mm, is represented by  $\hat{y}$ . The new area in  $A$ , formerly 1 mm<sup>2</sup>, is represented by  $\hat{A}$ .

$\nu$	.1	.2	.3	.4	.49
$\mu$	45.45	41.66	38.46	35.714	33.56
$\hat{x}$	1.1	1.1	1.1	1.1	1.1
$\hat{y}$	1	1	1	1	1
$\hat{A}$	1.1	1.1	1.1	1.1	1.1

**Table 3.2** Mesh refinement. A mesh refinement study showed that a finer mesh is unnecessary to maintain optimal accuracy of the hyperelastic model in a simple 1 mm by 1 mm square.

Degrees of Freedom	$\hat{A}$	Error
2262	1.1	0%
3866	1.1	0%
7642	1.1	0%
25530	1.1	0%
100450	1.1	0%

$x$ -direction for a 1 mm by 1 mm square. Comparing the linear elastic model with the neo-Hookean hyperelastic model, we see that the linear model fails to converge at values where the hyperelastic model can still be evaluated using the COMSOL FEM solver MUMPS for both with 3866 degrees of freedom. The results of this test can be seen in Table 3.3. The linear model fails to converge for growth above 30% strain. The other FEM solvers in COMSOL had the same failure to converge even with mesh refinements. This is not unexpected given that the linear elastic model is not meant for finite strain theory, and a 30% strain well exceeds infinitesimal strains. Additionally, if we use additive strain decomposition instead of multiplicative strain decomposition as described in Section 1.4.1, the linear elastic model fails to converge even under 1% growth strain. The hyperelastic model implemented in COMSOL always includes multiplicative strain decomposition.

In order to double the area of the square region, making it 2 mm<sup>2</sup>, with isotropic growth, we

**Table 3.3** Linear elastic versus hyperelastic convergence. A comparison between the linear elastic and hyperelastic model shows that the linear model fails to converge above 30% strain. As expected outside the range of infinitesimal strains, the linear model will have issues converging. The hyperelastic model continues to work through all growth strains tested which supports our modeling choice of using a hyperelastic formulation rather than a linear elastic formulation for our simulations.

Strain Percent	Linear Elastic Model Area	Hyperelastic Model Area
10%	1.1	1.1
20%	1.2	1.2
30%	1.3	1.3
40%	n/a	1.4
50%	n/a	1.5

needed to make  $\det(\mathbf{G}) = J_{\mathbf{G}} = 2$ . For isotropic growth, the stretch ratios in each directions are equal. So we set the stretch ratios  $\lambda_i = \sqrt{2}$ , which yields a determinant of 2. We tested the accuracy in COMSOL and received a calculated area of 2 mm<sup>2</sup>.

### 3.2.1.1 Area Conservation

We also tested situations where area is conserved, as in the case of doubling the width and halving the height with the same geometry as shown in Figure 3.4 and no  $x$ -displacement at  $x = 0$ . This is achieved with a growth tensor

$$\mathbf{G} = \begin{bmatrix} 2 & 0 \\ 0 & -0.5 \end{bmatrix} = \mathbf{I} + \epsilon_{\text{th}}. \quad (3.11)$$

The determinant  $J_{\mathbf{G}}$  equaling one, as explained in Section 1.4.1, indicates that volume is conserved. In order to have COMSOL implement this  $\mathbf{G}$ , our thermal strain is

$$\epsilon_{\text{th}} = \begin{bmatrix} 1 & 0 \\ 0 & -0.5 \end{bmatrix}. \quad (3.12)$$

As expected, when implemented this yielded exactly a 2 mm by 0.5 mm rectangle which can be seen in Figure 3.5.

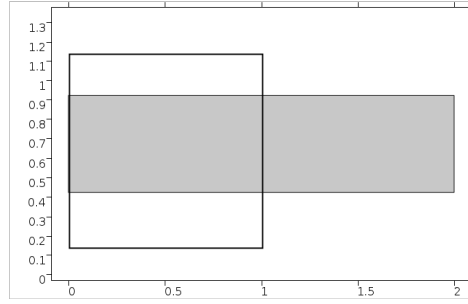


**Figure 3.5** Doubling the width and halving the height of a square. Even with strains as large as 100%, the multiplicatively decomposed hyperelastic model remains accurate. Here we implemented a 100% strain in the  $x$ -direction and a -50% strain in the  $y$ -direction to create a 2 mm by 1 mm rectangle from our 1 mm by 1 mm square. Area is conserved.

### 3.2.2 Three-Dimensional Tests

With the two-dimensional results in mind, we added another spatial dimension to match what we will be modeling so we considered a cube with 1 mm sides with three of the faces fixed to have no normal displacement, one each for an  $xy$ ,  $yz$ , and  $xz$  face, while all other faces had a no stress boundary condition. We found the hyperelastic model matched the analytical solution for all growth strains tested even at 100% strain with no error.

In the case of isotropically tripling the volume of a cube with 1 mm sides where  $J_G = 3$  and each element of the diagonal, the stretch ratios, would be  $\lambda_i = \sqrt[3]{3}$  with  $i = x, y, z$ . In COMSOL, we set the strain to be  $\epsilon_{th} = \sqrt[3]{3} - 1$  and no error was found with the computed volume.

## CHAPTER

# 4

## STOMACH BENDING

### 4.1 Motivation

Left-right asymmetry is a common anatomical feature and the stomach is no exception. In the embryonic stomach, the curvature changes as the stomach develops in many vertebrates. It goes from a straight centrally located tube to a multiply curved tube located on the left side of the abdomen. However the emergence of the asymmetry in the stomach during organogenesis is not well understood. Some hypotheses involve rotation of the stomach or external forces such as the surrounding tissues [LM69]. However, recent experiments have shown that asymmetrical gene expression in some way causes this curvature [Dav17]. We further investigated the hypothesis from [Dav17] that asymmetry of the stomach is intrinsic to the stomach itself as opposed to resulting from external forces, and is a result of asymmetric gene patterning causing asymmetric growth. We compared different models of the asymmetries in stomach growth qualitatively to images from



[Dav17] along with their geometric ratio data.

## 4.2 Two-Dimensional Model

To clarify our modeling priorities, we began with a model in two dimensions where the two tissue layers of the stomach, the endoderm and mesoderm layers, on the left side were undergoing growth strains. Since we were focused on the difference of behavior of the left relative to the right side of the stomach, we modeled growth only on the left side of the stomach. To determine if the relative stiffnesses of the regions was an influential factor, we considered the range of values found in literature such as [Mas04], [Gor17] for the Young's modulus in developing tissues, and varied these stiffnesses in the mesoderm and endoderm. We also considered whether the location of expansion the endoderm, mesoderm, both, or just on the boundaries, was significant. Insight from these two dimensional experiments was used to inform the development of our three dimensional model.

### 4.2.1 Model Geometry

In order to create our model, we had to simplify the observed histology of the embryonic frog stomach as seen in [Dav17] (Figure 4.1) . We kept the same four basic mirrored regions of the Stage

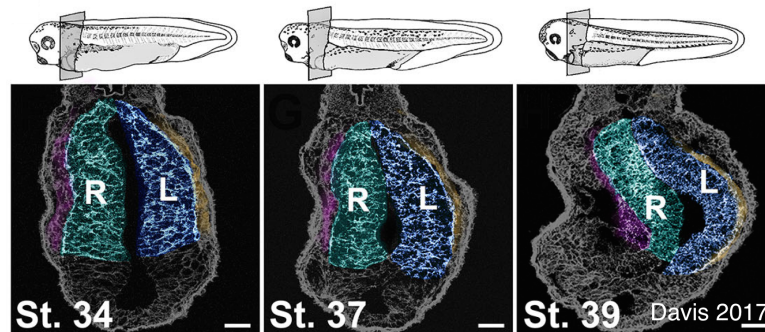


**Figure 4.1** Cross section of a developing frog at stages 34, 37, and 39. The epithelium is false-colored pink and yellow on the right and left side respectively. The mesenchyme is false-colored aqua on the right side and blue on the left side. Notice the difference in curvature in Stages 34 and 39 but also the consistent location of the top attachment point. From [Dav17].

34 frog stomach in our geometry and the two tissue layers as seen in Figure 4.2. The colors in Figure 4.2 correspond to the colors given in Figure 4.1. Based on the published data in [Dav17], the overall size of the stomach (the outer ellipse) was set to be  $400\text{ }\mu\text{m}$  by  $200\text{ }\mu\text{m}$ . The next smaller ellipse, representing the endoderm, was  $350\text{ }\mu\text{m}$  by  $150\text{ }\mu\text{m}$ . The innermost ellipse, representing the lumen, was  $220\text{ }\mu\text{m}$  by  $40\text{ }\mu\text{m}$ . The bottom third of our geometry corresponds to the liver as seen in the uncolored portion of Figure 4.1 and was included for only for visual completeness. We fixed the top-most point in our geometry with a boundary condition of no displacement in any direction and no rotation. All boundaries were considered to be under no stress,  $\hat{n} \cdot \sigma = 0$ .

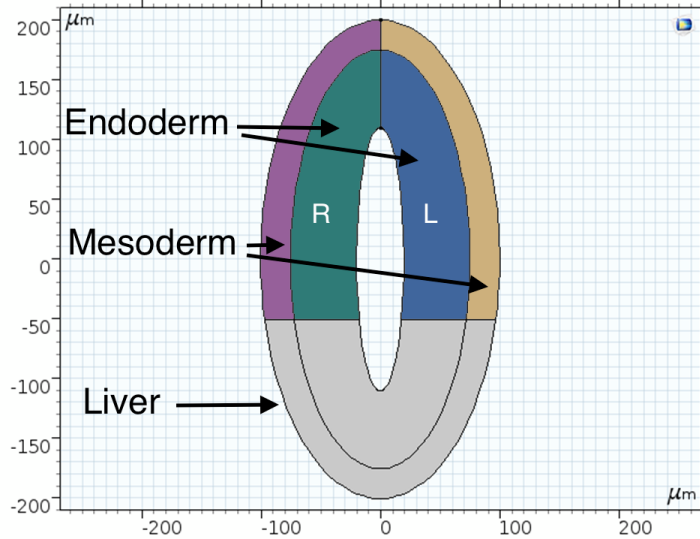


**Figure 4.2** Simplified 2D histology. The simplified histology for the our model incorporates the four distinct sections of the stomach (right and left endoderm and right and left mesoderm) and the liver, for completeness, with colors corresponding to the previous figure. The size of the stomach at this stage is approximately  $400\text{ }\mu\text{m}$  by  $200\text{ }\mu\text{m}$ , based on measurements from [Dav17]. Note that the right side of all images corresponds to the left side of the stomach as in [Dav17] from an anterior viewpoint. All directions are stated in reference to this orientation.

### 4.2.2 Modeling Assumptions

For the two dimensional model, we made several assumptions about the properties of the domain material. For computational ease, we began by considering the material to be linearly elastic because the hyperelastic tests for our chosen strains in 2D yielded no significant difference in results but were significantly more computationally expensive. With respect to linearly elastic materials, Poisson's ratio was held at  $\nu = .49$  since we considered the material to be incompressible and Young's modulus was varied in the experiments. We also considered each stomach region to be materially isotropic and all growth in these simple experiments was modeled as isotropic as well. All strains implemented were considered to be in the plane. Because all strains were isotropic and in the plane, Equation 1.2.7 simplifies to

$$\mathbf{G} = \begin{bmatrix} \lambda & 0 \\ 0 & \lambda \end{bmatrix}, \quad (4.1)$$

for the left side of the stomach where  $\lambda > 1$  is the stretch ratio. For the right side of the stomach,  $\mathbf{G} = \mathbf{I}$ .

### 4.2.3 Two-Dimensional Results

#### 4.2.3.1 Stiffness Tests

The main parameter of interest in these 2D models was the Young's modulus  $E$ , which describes the stiffness of the material. Given a range of values embryonic tissues' stiffnesses,  $E = 100 - 1000$  Pa [Phi13], we tested the extremes in different domains to see if there would be any marked difference in grown shape. As shown in Figure 4.3, there was no visible difference in shape change regardless of the choice of Young's modulus for each of the regions. Therefore, for all further experiments we set  $E = 100$  Pa for all regions.

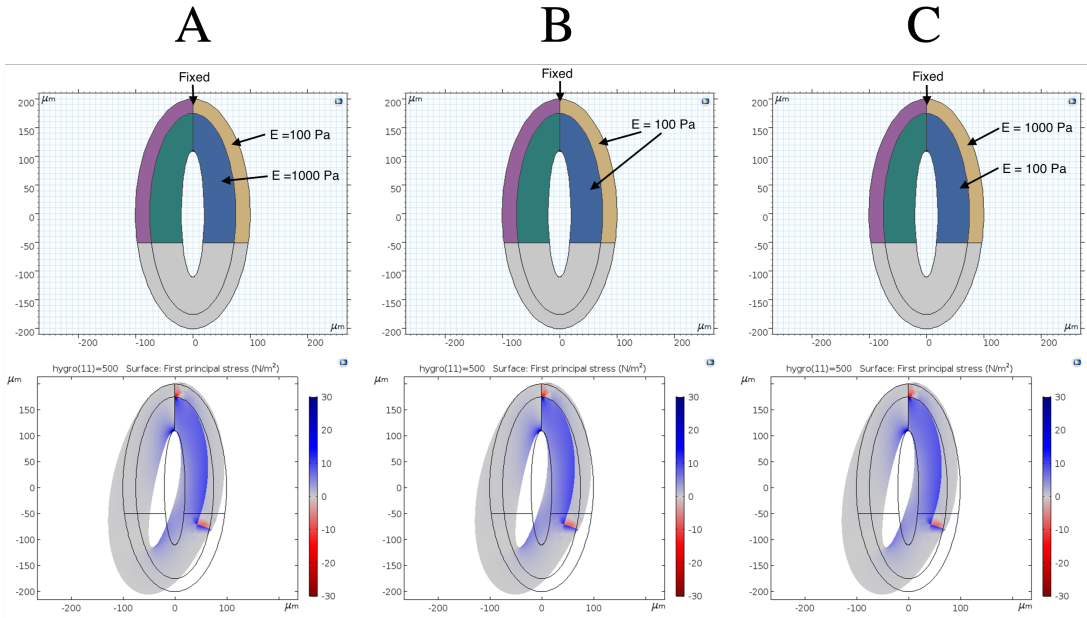


**Figure 4.3** Test of stiffness effects. (A) has the maximal stiffness of  $E = 1000$  Pa on the interior and the minimal stiffness of  $E = 100$  Pa on the exterior. (B) is meant as a control where both domains have the same stiffness  $E = 100$  Pa. (C) has the maximal stiffness of  $E = 1000$  Pa on the exterior and the minimal stiffness of  $E = 100$  Pa on the interior. In the simulations shown, areas of positive stress (tension) are depicted in blue and negative stress (compression) are depicted in red.

#### 4.2.3.2 Variation of Growth Location

We also tested isotropic growth in either of the two left tissue layers or both. As shown in Figure 4.4, expanding the left mesoderm layer alone is the most accurate when compared to the published images in [Dav17]. Given that the expansion of the left mesoderm gave the best result qualitatively, we further hypothesized that the expansion of the leftmost boundary alone may also give the anticipated shape change. As seen in Figure 4.5, that hypothesis was set aside, as boundary expansion yielded very little bending. Therefore for further experiments, we considered all growth to be in the domain rather than on the boundary.

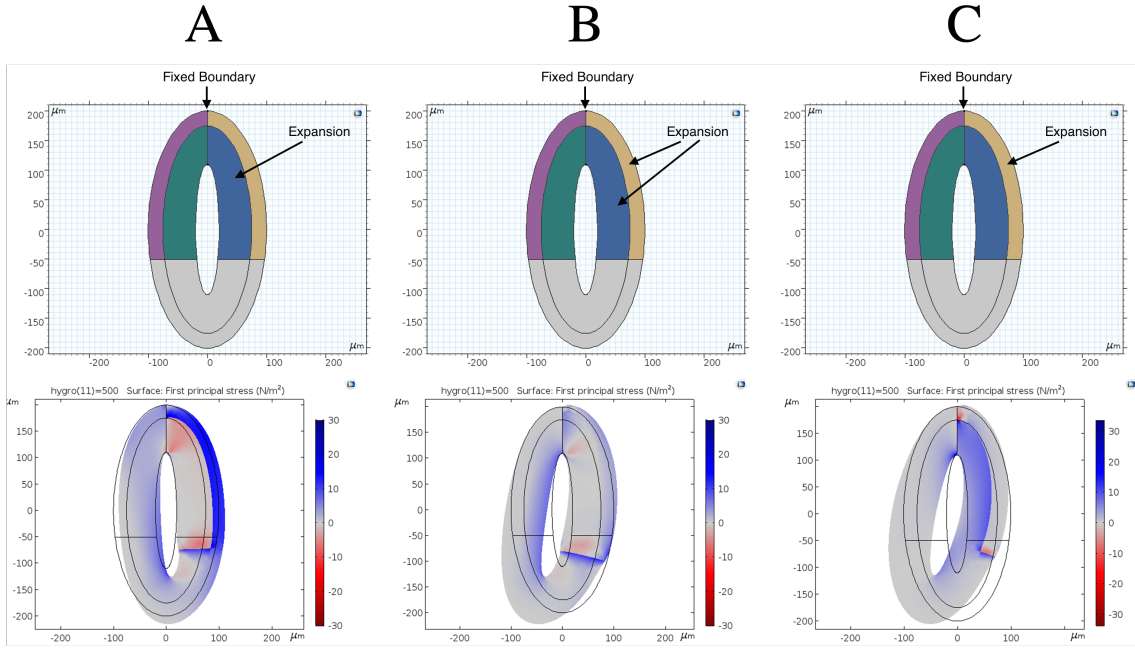


**Figure 4.4** Tests for growth location. Each column represents a different scenario of domain expansion. As the endoderm expanded in (A) it began to curve the opposite direction of what was anticipated. (B) Both regions expanded and it curved in the correct direction. However (C) had the most dramatic curve. In the simulations shown, areas of tension are depicted in blue and compression are depicted in red.

Because we implemented a large isotropic stretch ratio of 1.25 to ensure that we would be able to observe any differences, we also did a parametric sweep of the stretch ratios  $\lambda$  to ensure lower values also gave the expected curvature. The stretch ratio  $\lambda$  ranged from  $\lambda = 1$  to 1.5 and we found consistent but less dramatic curvature at the lower values, excluding 1 where as expected no growth occurred. A sample of the results is shown in Figure 4.6. Based on our results in 2D, we concluded that growth should occur in the left stomach and not on any boundary, and that the system was not sensitive to the Young's modulus between tissue layers. However, a three-dimensional model is necessary to gain a complete understanding of the problem, as the stomach bends in multiple directions.

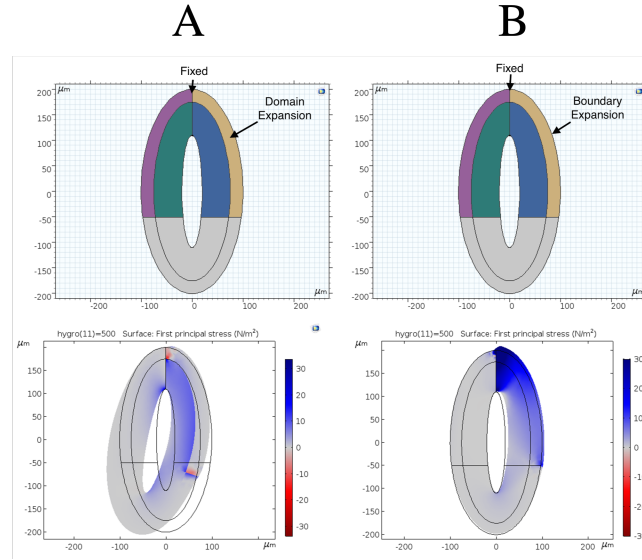


**Figure 4.5** Growth in the domain as compared to the boundary. The columns compare (A) expanding the left side mesoderm to (B) growing the left side's boundary. The left boundary expansion did not give the expected qualitative result. In the simulations shown, areas of tension are depicted in blue and compression are depicted in red.

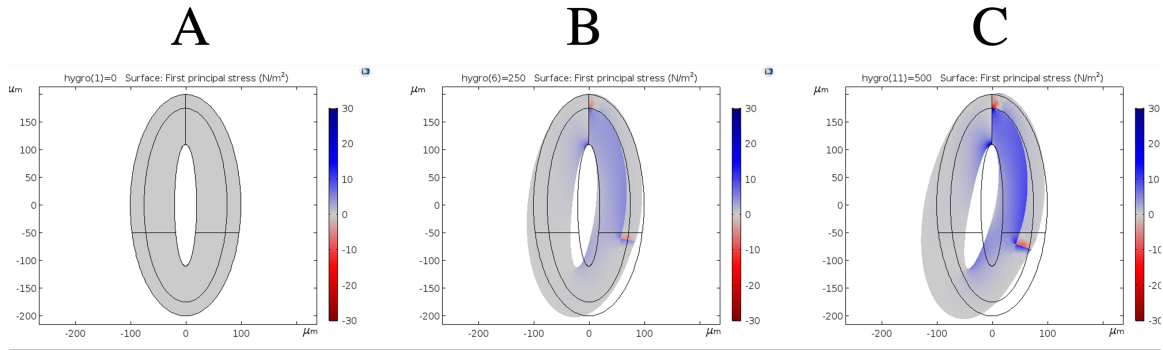


**Figure 4.6** Parametric study of isotropic stretch ratio as it affects curvature. A representative sample from our parametric study shows growth strains of (A)  $\lambda = 1$ , (B) 1.25, and (C) 1.5 in the mesoderm layer. More dramatic curvature is seen at the higher values of  $\lambda$ , as predicted. In the simulations shown, areas of tension are depicted in blue and compression are depicted in red.

### 4.3 Three-Dimensional Model

In order to most accurately capture the development of stomach asymmetry, we added another level of complexity by making our models three-dimensional. Tissues are inherently three-dimensional structures and may experience out-of-plane strains. As in our two-dimensional simulations, we will continue modeling the growth of the left stomach relative to the right. This is because we assume both sides are undergoing mitosis but that the asymmetric gene expression on the left stomach causes a change in either cell intercalation or the rate of relative mitosis. [Dav17] published box and whisker plots of the relative widths of the left and right endoderm and mesoderm layers of the embryonic frog and mouse stomach at various stages and they calculated the statistical significance. Using pixel counting, we captured the data from the medians of their box and whisker plots to calculate left-right ratios as shown in Table 4.1. Based on the ratios in Table 4.1, we concluded that

**Table 4.1** Left-right (LR) endoderm and mesoderm width ratios in developing mice and frogs as calculated from the reported medians. The width the endoderm and mesoderm on the left and right side of the mouse and frog stomach changes as the stomach develops. Both sides begin with statistically the same size endoderm, however the ratio of the left to the right decreases to become statistically significantly different from 1 over time as calculated by the authors of [Dav17]. This data was captured from plots in Figure 2E, F, M, and N in [Dav17]. Asterisks indicate values found to be statistically different from 1 as calculated by the authors of [Dav17].

Organism	Stage	L:R Ratio	
		Endoderm	Mesoderm
Frog	34	0.97	1.1
	37	0.93	1.0
	39	0.69*	0.38*
Mouse	10	0.98	0.94
	10.5	0.83*	0.89
	11	0.82*	0.87*

in order to agree with the *in vivo* behavior of the stomach our models must display LR relative radial thinning.

### 4.3.1 Modeling Assumptions

#### 4.3.1.1 Geometric Assumptions

Building on the result of our two-dimensional experiments, we developed a three dimensional stomach geometry where we assumed all material parameters, like  $\mu$  and  $\det(\mathbf{A})$ , were homogeneous and uniform throughout our entire domain. Based on observations from published experimental images, we combined the mesoderm and endoderm of each side to simplify the model as the relative size of the mesoderm layer is much smaller than the endoderm layer as seen in Figure 4.7.

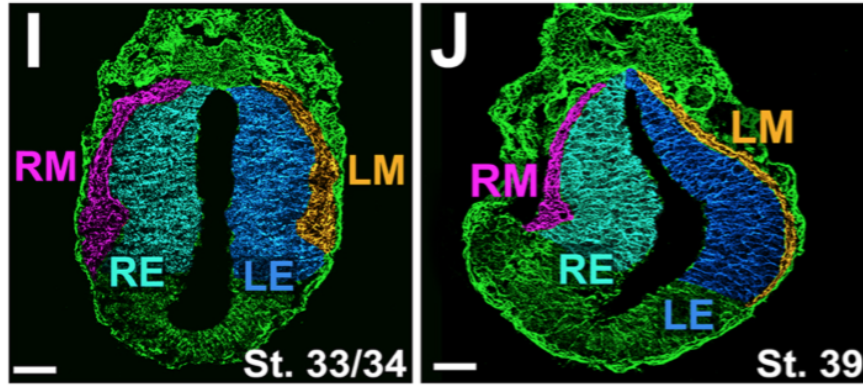


**Figure 4.7** Size comparison of endoderm to mesoderm. At Stage 34 and 39, the endoderm is the larger tissue on the left and right sides of the frog stomach. The change of left and right endoderm size over time is quantified in Table 4.1. From [Dav17].

To simplify the geometry, the liver division used in the two-dimensional geometry was eliminated. Three views of the undeformed geometry can be seen in Figure 4.8. Since we assumed our simplified undeformed 3D geometry to be symmetrical dorsally and ventrally, and in order to reduce computational time and effort, we considered just half of our new geometry as shown in Figure 4.9 with boundary conditions already labelled.

As previously described in Section 3.1.2, we also created a local orthogonal coordinate system,  $(R, h, z)$  to define growth based on our initial geometry.  $R$  describes the radial direction,  $h$  describes



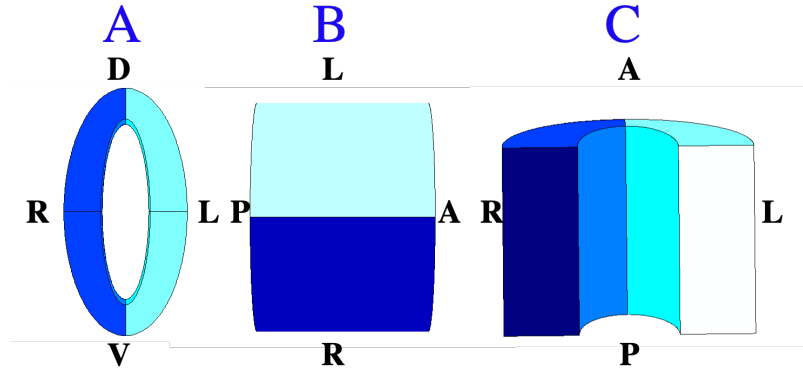


**Figure 4.8** Simplified 3D geometry for the undeformed stomach. For all subfigure labelling: D: dorsal, V: ventral, A: anterior, P: posterior. L and R are the initially symmetric left and right sides respectively. (A) is a view of the anterior face. (B) is a dorsal view. (C) is a cut view of the dorsal half. Color differentiation is to aid in visualization of the shape change.

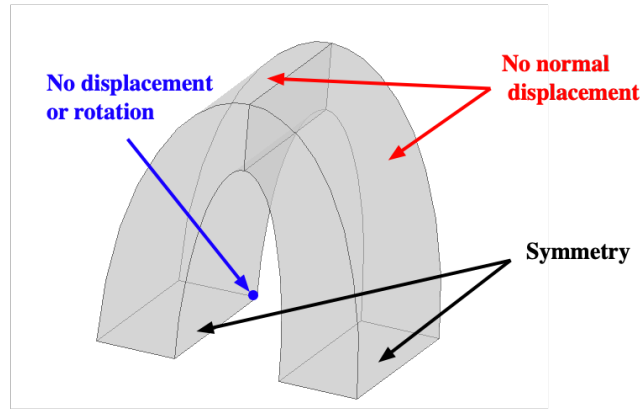


**Figure 4.9** Boundary conditions for the half domain. Due to the initial symmetry of our domain, we computed our model on a half domain. The bottom two faces have a symmetry boundary condition, meaning they have no normal displacement to the cut plane. We pinned a point, giving it no rotation and no displacement. All other surfaces have a no stress boundary condition,  $\hat{n}\sigma = 0$ . As an additional modeling assumption due to surrounding tissues, the two posterior faces cannot move normal to the plane but are free in the other directions.

the hoop direction, and  $z$  describes the axial direction, similar to cylindrical coordinates. This coordinate system is illustrated in Figure 4.10 with representative vectors showing the coordinate directions at different locations.

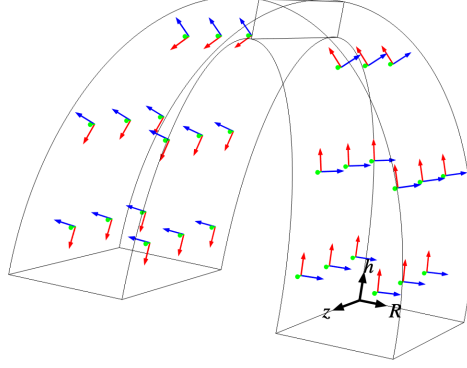


**Figure 4.10** Local coordinate system  $(R, h, z)$ . The black arrows give the local coordinate directions from the origin. The green vector arrows represent the axial direction  $z$ . The red vector arrows represent the hoop direction  $h$  and the blue vector arrows represent the radial direction  $R$ .

#### 4.3.1.2 Material Assumptions

For the three dimensional models, we no longer simplify our model to be linearly elastic. The soft tissue of the stomach is assumed to be hyperelastic due to the potentially large deformations that occur during development. We chose the neo-Hookean model for its simplicity and because the Fung hyperelastic model for soft tissues requires more unknown parameters. The tissues are assumed to be isotropic and elastically incompressible.

#### 4.3.1.3 Growth Assumptions

The *in vivo* stomach curves, crossing the midline from the left side over to the right moving posteriorly to anteriorly and exhibits radial thinning as observed in Figure 4.1. We will compare our simulations with the observed features of the frog stomach. Because only growth differences lead to shape change, we ignored the potential overall isotropic growth of the whole organ; we modeled instead only relative growth of the left to right side, where the growth deformation tensor as described in Equation 1.2.7 on the right side of the stomach was  $\mathbf{G} = \mathbf{I}$  for all models. Growth was considered to be homogenous on both the right and left side. We made three hypotheses about the left side: H1.

isotropic growth, H2. anisotropic growth without volume conservation, and H3. anisotropic growth with volume conservation.

For H1, we assumed that the shape change was due to a greater rate of mitosis on the left side relative to the right. This assumption will cause an increase in left side volume. In this case with our local coordinates the growth tensor on the left is

$$\mathbf{G}(R, h, z) = \begin{bmatrix} \lambda & 0 & 0 \\ 0 & \lambda & 0 \\ 0 & 0 & \lambda \end{bmatrix}, \quad (4.2)$$

where  $\lambda = 1.2$ . Since  $\lambda^3 > 1$ , volume will increase in the ratio of  $\det(\mathbf{G}) = 1.2^3$ .

For H2, we considered anisotropic growth in each direction without volume conservation. This assumption will also cause an increase in left side volume and is comparable to an increased rate of oriented cell divisions in a specific direction as compared to the other directions. In this case,

$$\mathbf{G}(R, h, z) = \begin{bmatrix} \lambda_R & 0 & 0 \\ 0 & \lambda_h & 0 \\ 0 & 0 & \lambda_z \end{bmatrix}, \quad (4.3)$$

where one of the stretch ratios  $\lambda_i = 1.2$  and the other two were one for  $i = 1, 2, 3$ , giving  $\det(\mathbf{G}) = 1.2$ .

For H3, we assumed that shape change was due to cell rearrangements only. This would mean that volume is conserved and therefore the determinant of the growth tensor  $\mathbf{G}$  is 1. With the local coordinates  $(R, h, z)$ , the growth tensor can be written as

$$\mathbf{G}(R, h, z) = \begin{bmatrix} \lambda_R & 0 & 0 \\ 0 & \lambda_h & 0 \\ 0 & 0 & \lambda_z \end{bmatrix}. \quad (4.4)$$

We tested two versions where  $\det(\mathbf{G}) = 1$ : a) the set of combinations where  $\lambda_i = 1.2$ ,  $\lambda_j = \frac{1}{\lambda_i}$ , and  $\lambda_k = 1$  and b) the set of combinations has  $\lambda_i = 1.2$  and  $\lambda_j = \lambda_k = \frac{1}{\sqrt{\lambda_i}}$  for  $i \neq j \neq k$ .

### 4.3.2 Results

In order to qualitatively match *in vivo* observations of the embryonic frog stomach, our model's geometry would need to change in several key ways from the original seen in Figure 4.8. The left side of the stomach, displayed in light blue for all figures, should move to the left in compared to Figure 4.8 A. Compared to Figure 4.8 B, the top line should become convex and the stomach should grow in the anterior direction. The left side cut face in Figure 4.8 C should thin to match the trend of width thinning seen in [Dav17].

#### 4.3.2.1 Isotropic Growth

Following H1, we considered growth to be isotropic for the left side with no growth on the right side. Volume is not conserved on the left side. This case can be considered equivalent to equal rates of mitosis in every direction in the the left side. The result shown in Figure 4.11 shows a slight shift of the anterior face towards the right. However, in in Figure 4.11 B, we do not see significant bending along the left side running posterior to anterior; it remains relatively straight. We can conclude from this discrepancy with the known biological shape change that the asymmetric-gene expression on the left side of the stomach does not cause simply a greater rate of mitosis in every direction.

#### 4.3.2.2 Anisotropic Growth with Volume Increase

Following H2, we modeled anisotropic growth of the left side of the stomach as a representation of oriented cell divisions. We considered oriented mitosis in each of our local coordinate directions individually. This oriented cell division would result in a lengthening in that specified direction. Since there was no equivalent shrinkage in any of the other directions, the domain's volume increased. For each individual direction, we held  $\lambda_i = 1.2$  and  $\lambda_j = \lambda_k = 1$  for  $i \neq j \neq k$ . We observed that:

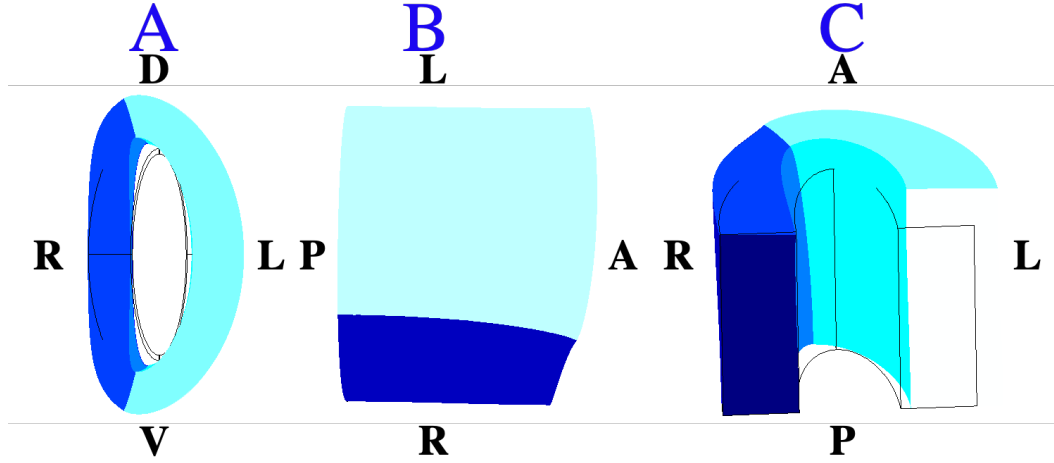


**Figure 4.11** Isotropic growth of the left side of the stomach and no growth of the right side. The stretch ratio in each direction is  $\lambda_R = \lambda_h = \lambda_z = 1.2$ . Under isotropic growth, the geometry becomes asymmetric and very slight bending relative to the applied growth is seen in the biologically anticipated direction in (A)-(C). This bend may increase given a higher stretch ratio. (C) The cut view is shown in perspective to aid with visualization of the bending.

- A stretch ratio of  $\lambda_R = 1.2$  gave a shape change, seen in Figure 4.12, that thickened the left side of the stomach but caused no bending.

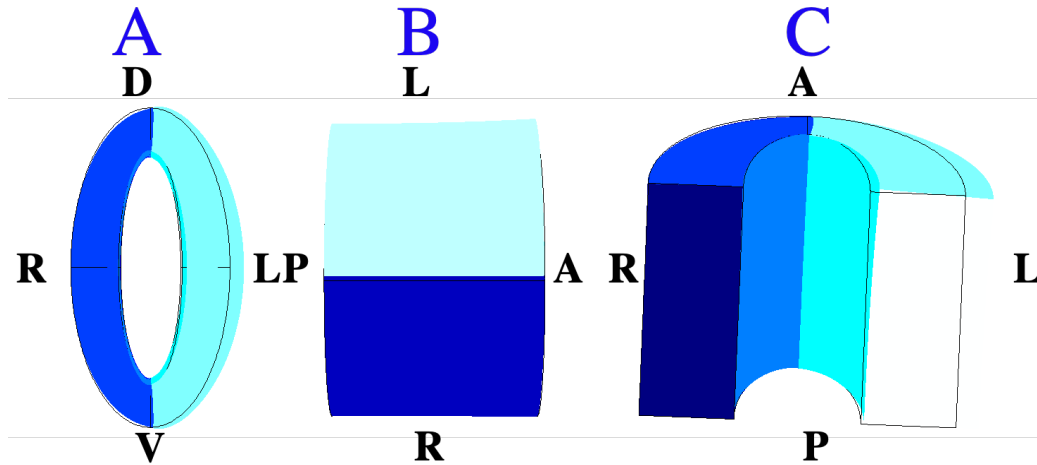


**Figure 4.12** Anisotropic growth on the left side in the radial direction. The stretch ratios are  $\lambda_R = 1.2$ ,  $\lambda_h = 1$ ,  $\lambda_z = 1$ . We observe thickening in the left side of the stomach in (A) and no bending in (A)-(C). Neither outcome is consistent with the shape changes seen in the developing frog stomach.

- A stretch ratio of  $\lambda_h = 1.2$  (Figure 4.13) yielded a slight bend to the left, in the opposite direction of what is observed in the frog, and an overall increase in the dorsal-ventral direction.

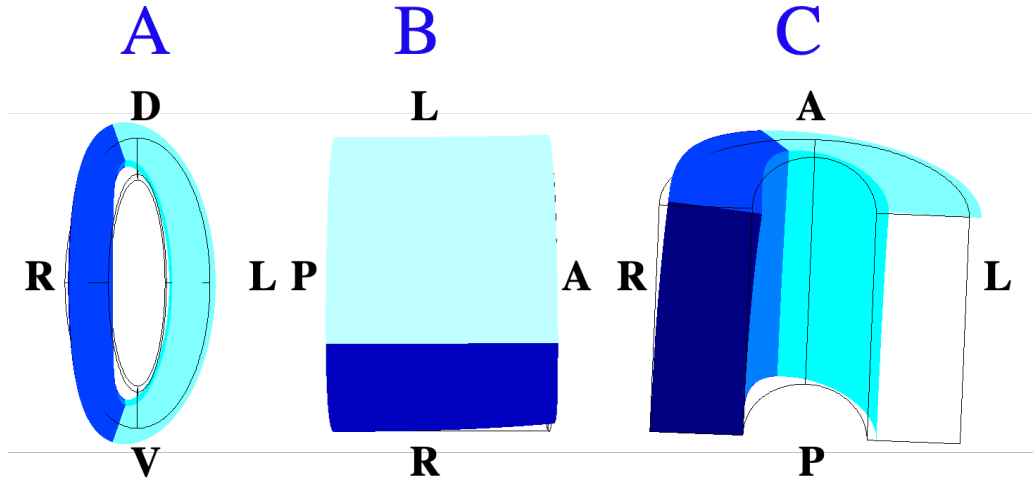


**Figure 4.13** Anisotropic growth on the left side in the hoop direction. The stretch ratios are  $\lambda_R = 1$ ,  $\lambda_h = 1.2$ ,  $\lambda_z = 1$ . The stomach appeared to extend in the dorsal-ventral direction in (A) but does not bend in the biologically anticipated direction in (B)-(C). This is not consistent with the shape changes seen in the developing frog.

- A stretch ratio of  $\lambda_z = 1.2$  (Figure 4.14) yielded a bend to the right, in the anticipated direction, but did not also yield the radial thinning seen in frog.

We can conclude that neither H2, a higher relative level of mitosis in just one direction of the left side, nor H1, a higher isotropic growth on the left side, can explain the shape change seen *in vivo*.

#### 4.3.2.3 Anisotropic Growth with Volume Conservation (Cell Rearrangements)

We hypothesized in H3 that the asymmetric gene expression seen in the stomach may cause a difference in the cell intercalation, or rearrangement, on the left side as compared to the right side. Since the cells are assumed to be purely rearranging, the volume of the stomach must be conserved and therefore  $\det(\mathbf{G}) = J_G = 1$ . We tested  $\lambda_i > 1$  in one direction balanced by  $\lambda_j < 1$  in one or two

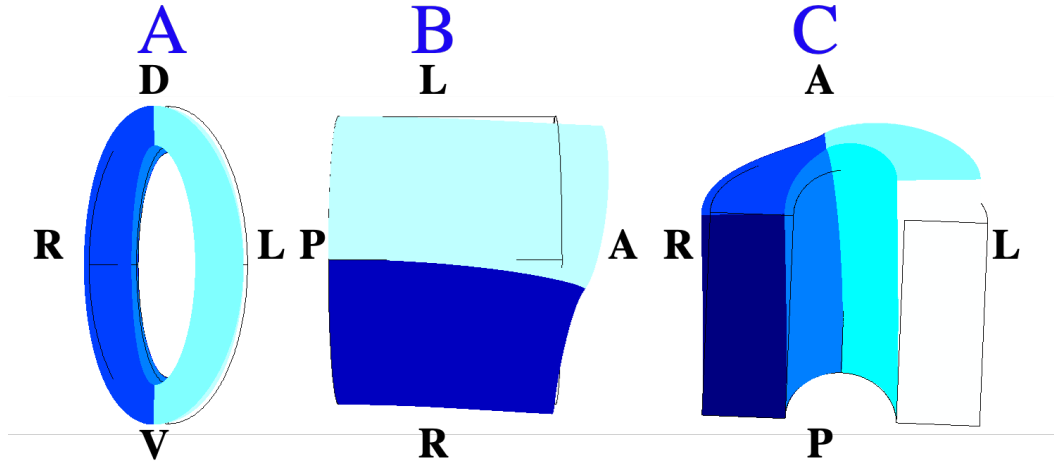


**Figure 4.14** Anisotropic growth on the left side in the axial direction. The stretch ratios are  $\lambda_R = 1$ ,  $\lambda_h = 1$ ,  $\lambda_z = 1.2$ . In (A)-(C), the deformed geometry shows bending from the left side over to the right side. However, it fails to show the radial thinning observed in [Dav17].

directions, where  $i \neq j$ , giving us 9 tests.

- **Radial thickening:** Radial thickening with  $\lambda_R = 1.2$  counterbalanced by shrinking in one or both of the other directions is shown in Figures 4.15-4.17, maintaining a constant volume. Radial thickening combined with hoop shrinking (Figure 4.16) creates bending unlike that seen *in vivo*. Radial thickening combined with axial shrinking with (Figure 4.17) or without (Figure 4.15) hoop shrinking creates a bend to the left in the wrong direction.

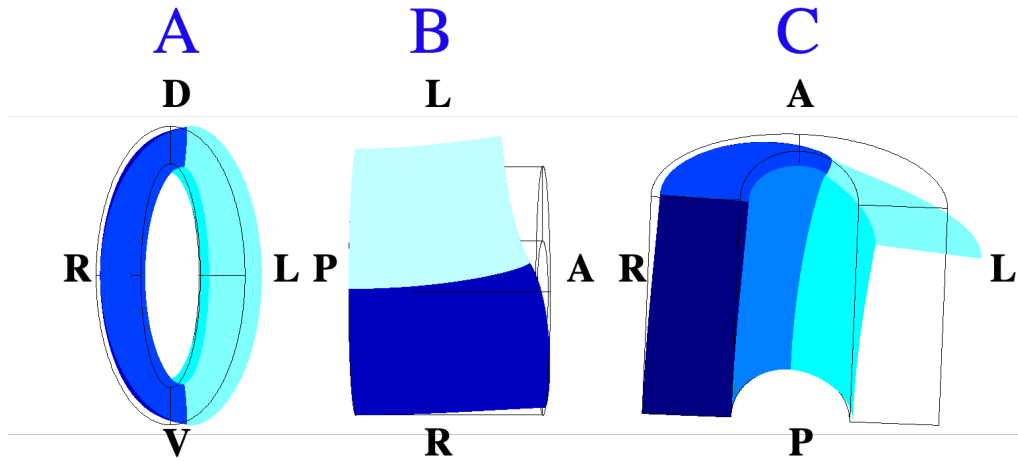


**Figure 4.15** Volume conserving anisotropic growth on the left side in the radial direction with shrinking in the axial direction. The stretch ratios are  $\lambda_R = 1.2$ ,  $\lambda_h = 1$ ,  $\lambda_z = 1/1.2$ . This shows the deformed right side crossing over into the left in (A)-(C) which is not consistent with what is seen in the embryonic frog.

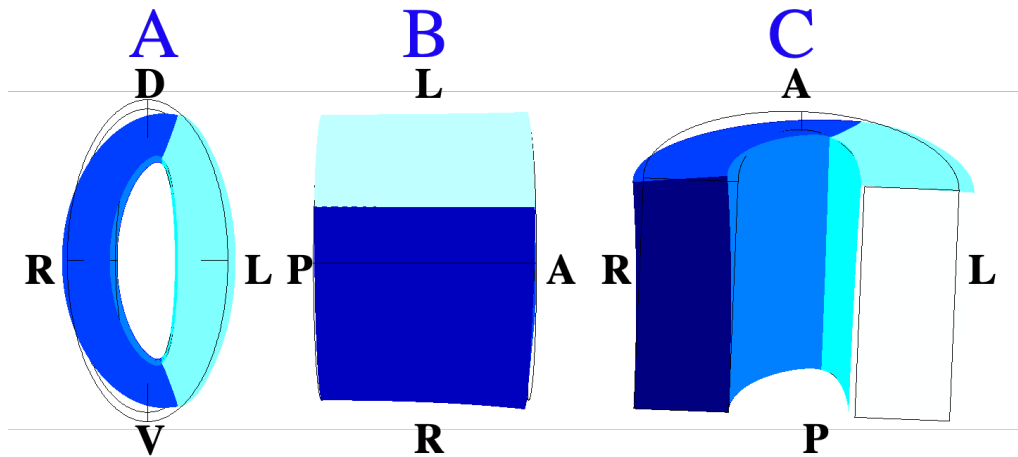


**Figure 4.16** Volume conserving anisotropic growth on the left side in the radial direction with contraction in the hoop direction. The stretch ratios are  $\lambda_R = 1.2$ ,  $\lambda_h = 1/1.2$ ,  $\lambda_z = 1$ . In views (A)-(C), this shows the deformed right side crossing over into the left which is not consistent with what is seen in the embryonic frog.

- **Hoop lengthening:** Hoop lengthening counterbalanced by an equivalent shrinking in one or both of the other directions is seen in Figures 4.18-4.20. Hoop lengthening with any combination of shrinkage consistently yielded a bend in the wrong direction. This bend is most



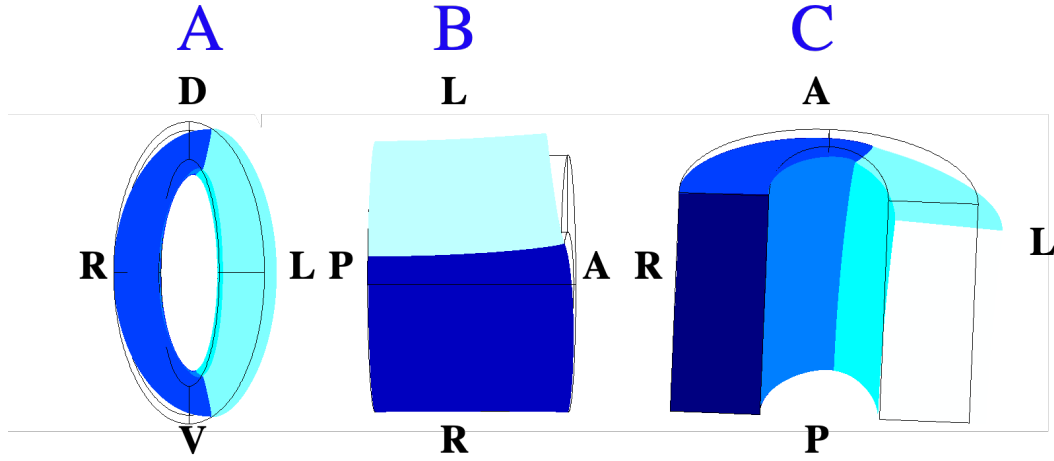


**Figure 4.17** Volume conserving anisotropic growth on the left side in the radial direction with shrinking in the axial direction and contracting in the hoop direction. The stretch ratios are  $\lambda_R = 1.2$ ,  $\lambda_h = 1/\sqrt{1.2}$ ,  $\lambda_z = 1/\sqrt{1.2}$ . In all views (A)-(C), the deformed right side crossed over into the left which is not consistent with what is seen in the embryonic frog.

visually significant in Figure 4.18, still quite visible in Figure 4.20, and less visually striking but still visible in Figure 4.19. Growth in the hoop direction is therefore not the primary factor creating the shape change seen in [Dav17] where significant radial thinning occurs in the frog embryo through Stages 34-39.

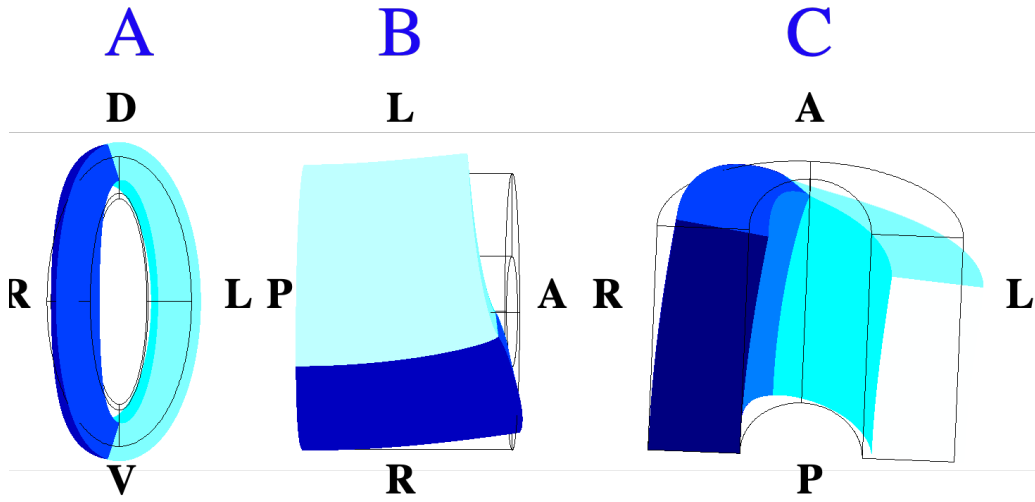


**Figure 4.18** Volume conserving anisotropic growth in the hoop direction with shrinking in the axial direction. The stretch ratios are  $\lambda_R = 1$ ,  $\lambda_h = 1.2$ ,  $\lambda_z = 1/1.2$ . (B) and (C) show bending in the opposite direction seen in [Dav17].

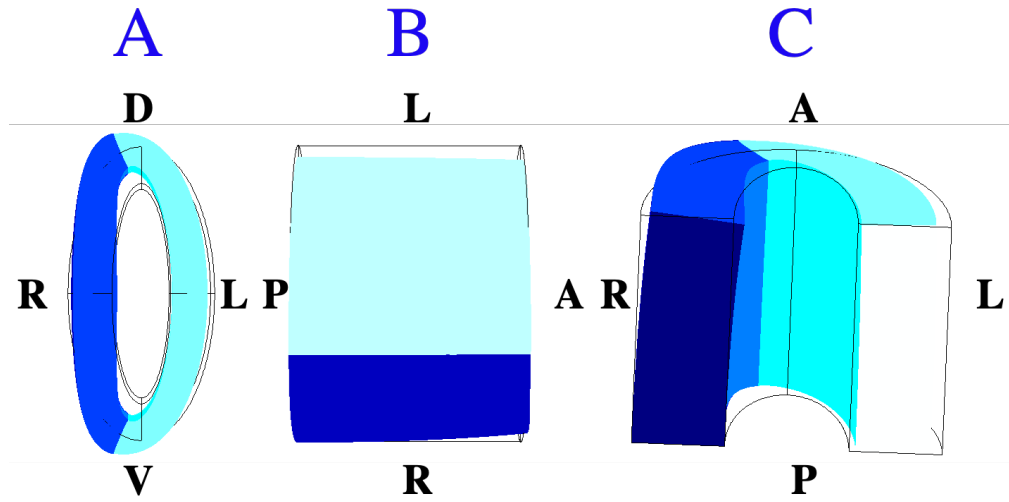


**Figure 4.19** Volume conserving anisotropic growth in the hoop direction with shrinking in the radial direction. The stretch ratios are  $\lambda_R = 1/1.2$ ,  $\lambda_h = 1.2$ ,  $\lambda_z = 1$ . (A) This shows bending in the opposite direction seen in [Dav17] though not to the extreme of the previous Figure 4.18.

- **Axial lengthening:** Axial lengthening counterbalanced by an equivalent shrinking in one or both of the other directions is seen in Figures 4.21-4.23. Any combination of shrinkage com-

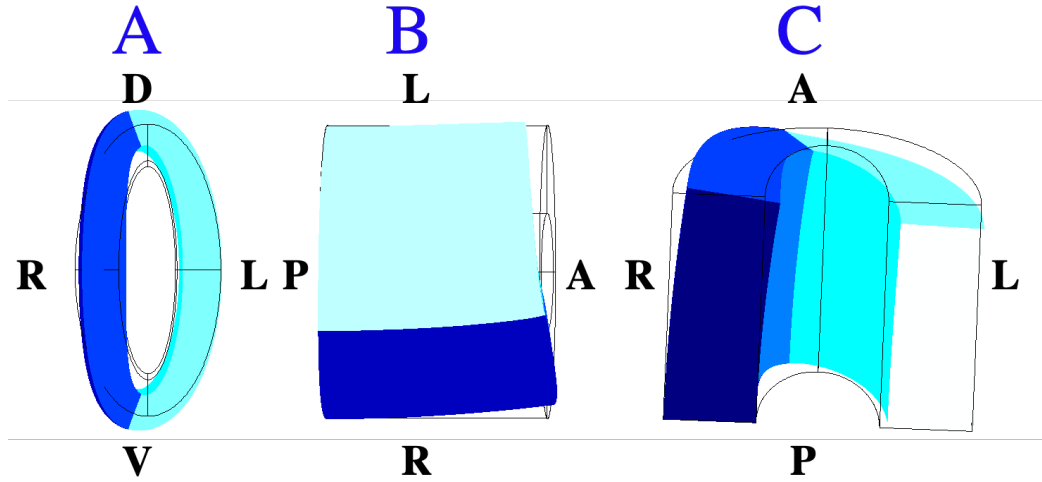


**Figure 4.20** Volume conserving anisotropic growth in the hoop direction with shrinking in the radial and axial direction. The stretch ratios are  $\lambda_R = 1/\sqrt{1.2}$ ,  $\lambda_h = 1.2$ ,  $\lambda_z = 1/\sqrt{1.2}$ . (B)-(C) Bending is in the opposite direction seen in [Dav17].

bined with axial lengthening yielded a bend to the right, in the biologically correct direction. Axial lengthening with hoop shortening bent in the correct direction but did not thin radially (Figure 4.21). Axial lengthening combined with both hoop shortening and radial thinning bent in the correct direction but is not as qualitatively similar as the following combination (Figure 4.23). Axial lengthening combined with radial thinning (Figure 4.22) yielded the most qualitatively similar result to all the non-mutant frog embryo images found in [Dav17].

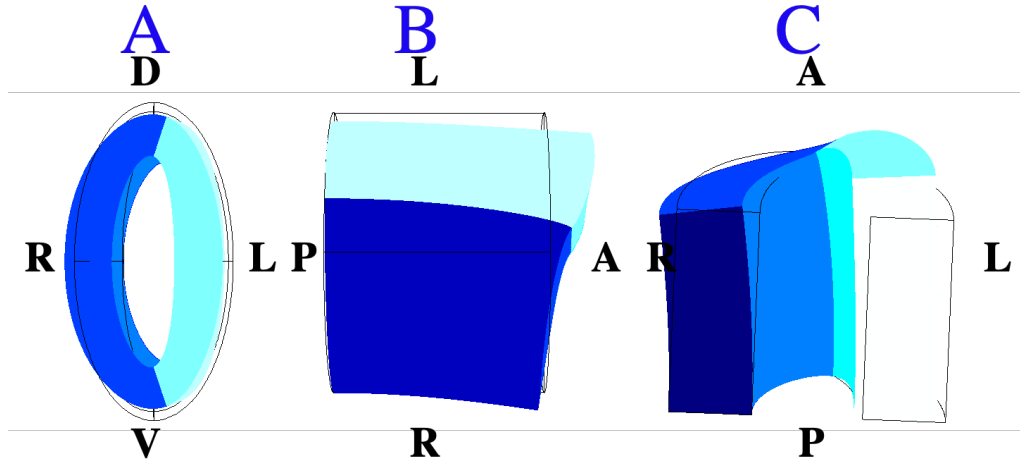


**Figure 4.21** Volume conserving anisotropic growth in the axial direction with contraction in the hoop direction. The stretch ratios are  $\lambda_R = 1.2$ ,  $\lambda_h = 1/1.2$ ,  $\lambda_z = 1.2$ . (B)-(C) show bending in the biologically anticipated direction.

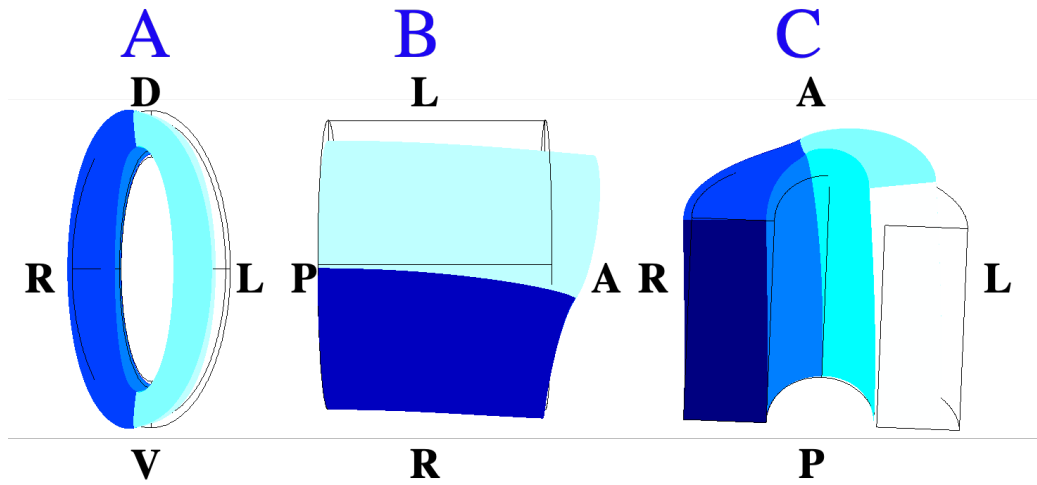


**Figure 4.22** Volume conserving anisotropic growth in the axial direction with thinning in the radial direction. The stretch ratios are  $\lambda_R = 1/1.2$ ,  $\lambda_h = 1$ ,  $\lambda_z = 1.2$ . (A)-(C) show bending in the biologically anticipated direction and (A) includes the thinner width on the left seen in [Dav17] as well.

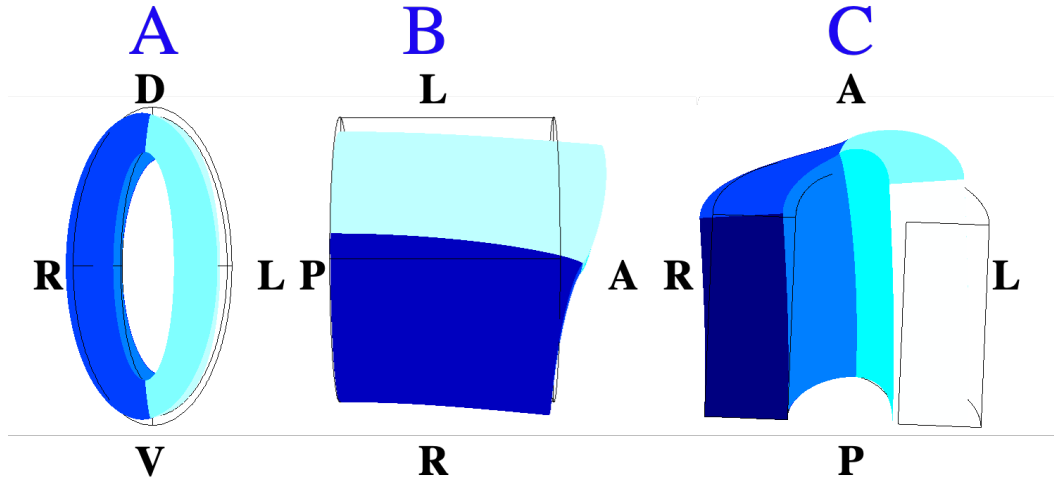


**Figure 4.23** Volume conserving anisotropic growth in the axial direction with contraction in the hoop direction and thinning in the radial direction. The stretch ratios are  $\lambda_R = 1/\sqrt{1.2}$ ,  $\lambda_h = 1/\sqrt{1.2}$ ,  $\lambda_z = 1.2$ . (A)-(C) all show bending in the biologically anticipated direction

## 4.4 Conclusions

Mathematical models of biological systems are necessarily simplifications of complex systems but a number of conclusions can be drawn from our simulations. The two-dimensional models allowed us to conclude that change in curvature is caused mostly by growth in our domain as opposed to on the boundary, implying that actuation of gene signaling occurs within the stomach and not just on the surface of the mesoderm. In the two-dimensional model, we also tested variations in stiffness of the left mesoderm and endoderm and showed it had an insignificant effect on the shape change; therefore, in our three-dimensional models we merged the endoderm and mesoderm. The three-dimensional model shows that a greater rate of mitosis alone in all directions in the left side of the stomach as compared to the right is not what causes the observed asymmetry, as it did not qualitatively match images of the developing frog stomach. Oriented cell divisions, represented mathematically as non-volume conserving anisotropic growth, could not cause both the biologically anticipated radial thinning and curvature. Specifically, radial thickening resulted in none of the

anticipated shape changes, hoop lengthening had a bend in the incorrect direction, and axial lengthening failed to yield radial thinning. We conclude that cell rearrangement, represented as volume-conserving anisotropic growth, is the most likely growth mechanism for the asymmetry in the stomach. We find that radial thinning with axial lengthening is the most qualitatively similar growth combination, meaning that cell rearrangement is an important factor in stomach shape change.

These models are useful for more than providing insight on the tissue changes leading to stomach asymmetry. They can suggest that the specific effect of genes known to cause asymmetry like *Foxj1*, *Pitx2*, and *Nodal* may be to cause oriented cell rearrangements. Future experiments should consider tracking cell location. Additionally, these simulations and conclusions may aid in identifying and explaining gene expression and developmental abnormalities. Further discussion of our results and conclusions can be found in Chapter 6.

## CHAPTER

# 5

## LUNG BRANCHING

Mathematical modeling of organogenesis, including branching, is an important tool for gaining biological insight from analyzing simpler model systems. We are using the emerging mathematical theory of morphoelasticity to test hypotheses about the growth and branching of the developing lungs. As will be discussed in Section 5.1.1, many models of lung branching have been focused on the signaling and either omit explicit modeling of shape change [Geo15], [GL18] or model shape change by simply moving a surface normal to itself without explicit conservation equations [Cle12b], [Cle12a], [MI12]. In [Geo15], the morphogen flux distribution on the epithelium was proposed to be an important factor for growth. In [GL18], modeling the transport of a representative morphogen to the epithelial surface in a variety of geometries showed that the flux distribution on the epithelial surface is strongly dependent on the local geometry of the branch tip. They conclude that, “We find that a single simple mechanism is theoretically capable of directing an epithelial tubule to elongate, bend, flatten, or bifurcate, depending solely on geometric ratios of the tissues in the vicinity of a

growing tubule tip." These hypotheses as to the correspondence between flux distributions and shape change were asserted in [GL18], but the associated tissue shape changes were never explicitly modeled. In this dissertation, we explicitly model both the signaling and the resulting growth. In order to test their hypotheses on flux distribution patterns and resulting shape changes we use the same transport modeling assumptions developed in [GL18] and implement epithelial growth using morphoelasticity in a hyperelastic shell.

## 5.1 Problem Background

Many organs contain branched structures which are essential to their function, such as the kidneys, the salivary and mammary glands, and the lungs. Our research focuses on the development of the branches in early stages of lung organogenesis. While the lungs' typical final shape and number of branches is known, understanding the mechanisms for the development of the lung is an important area of ongoing research. In [Met08], the authors have defined for the early lung three main branching modes: domain, planar, and orthogonal, which are illustrated in Figure 5.1. *Domain* branches set the overall shape of each lung lobe by forming the initial scaffold. *Orthogonal* branching fills the interior and surface of each lobe, with the lobe edges undergoing *planar* branching. It was speculated in [Met08] that these modes are caused by different mechanisms. However, the authors of [GL18] showed that planar and orthogonal could both be due to the same mechanism but in different local geometries.

### 5.1.1 Brief Overview of Published Models

Much previous modeling has been focused on lung organogenesis, with a wide variety of model assumptions and methods. The different models focus on either morphogen transport, mitosis, geometry, mechanics, or a combination. One approach, considering the transport and geometry, can be found in [Cle12b]. [Cle12b] modeled the lungs' growth in two dimensions as a moving interface between the epithelium and the mesenchyme but explicitly stated that mechanics was ignored in their model. The model in [Cle12b] based epithelial growth on the gradient of the morphogen



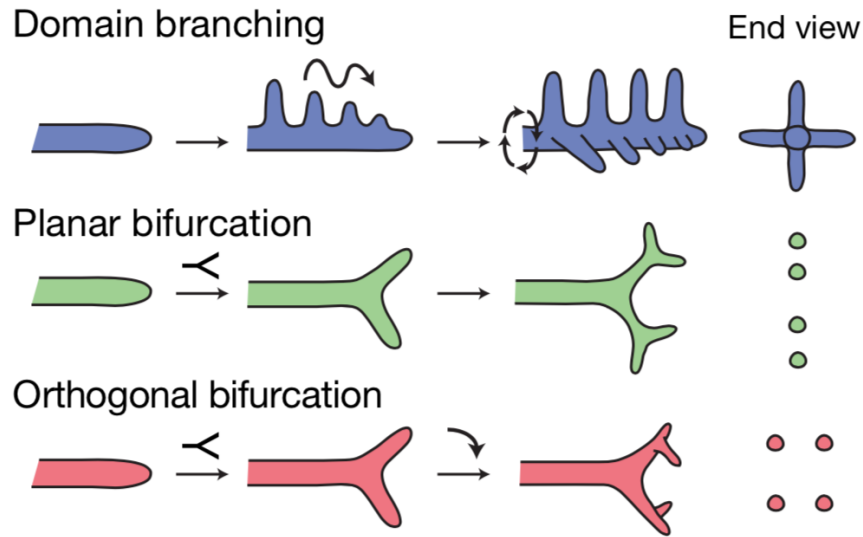


**Figure 5.1** Three modes of lung branching as defined and shown in [Met08]. The three modes of lung branching were defined as domain, planar, and orthogonal branching. For domain branching, new lung bud tips grow from the sides of an existing stalk. For planar bifurcation, the tip of an existing lung bud splits and this pattern continues iteratively. This results in lung tips that all lie on a line, as seen in the end view of the figure. For orthogonal bifurcation, the tip of a lung bud splits but the next generation of splitting is rotated  $90^\circ$ . This results in lung bud tips that do not exist along the same line but rather in a plane, as seen in the end view of the figure. [Met08] hypothesized that these different modes were all caused by different mechanisms. Reproduced from [Met08].

in the surrounding mesenchyme. The authors assumed that the partial differential equations for their model were in a quasi-static state because of the different time scales of growth and diffusion. Therefore at equilibrium the diffusion equation for the morphogen simplifies to the Laplace equation. A related paper by some of the same authors [Cle12a] considered a model that was also in 2D. The main focus of this model was branching asymmetry, and searching for conditions that generated asymmetry using a moving interface model similar to that used in [Cle12b]. Another closely related paper considered both molecular and physical aspects to affect growth [CM14]. The mesenchyme in [CM14] is modeled as a viscous medium and is incompressible. The model epithelium in [CM14] grew based on the gradient of the morphogen FGF10. The authors hypothesized that branching is affected by the local geometry based on the gradient of morphogen between the distal and proximal mesenchyme. They pointed out that lungs clearly have some sort of self-organization process

because they are self-avoiding, and that this distance between tissues may be the cause. However, they only considered "ideal tubular geometry" where the cross-sectional area was always circular.

In [MI12] and [Ger11], the authors considered a model, which they implemented in COMSOL, for lung branching, where reaction-diffusion equations govern growth. This growth, however, is modeled by moving the epithelium with a velocity that is purely normal to the surface. This velocity is determined by the concentration of several chemical species, governed by reaction-diffusion equations. They also assume that the thickness of the domain is constant, reasoning that the epithelium has one or a few layers of cells. In [MI12] specifically, they suggest modeling this process across multiple subdomains to reduce numerical artifacts. The authors tested the convergence of several reaction-diffusion equations including the Schnakenberg-Turing model in a two dimensional domain. [Ger11] considered a three dimensional domain where growth is modeled as surface normal displacements proportional to morphogen concentration at the surface of the epithelium. The focus of that paper was optimizing solution times in COMSOL without losing accuracy. The authors found that remeshing at small timesteps and using the built-in solver 'MUMPS' gave quick-running, stable solutions.

### **5.1.2 Simplified Signaling and Spatial Distribution of Morphogen Flux**

As pointed out by [Geo15] [GL18], it is not precisely the gradient of a morphogen that affects shape changes in the downstream tissue. It is common for biologists and modelers to use the term "gradient sensing," but strictly speaking, for sessile cells it is only possible to sense flux. Motile bacteria can engage in gradient sensing by moving through the gradient. The cells in an epithelium are stationary and thus can only directly sense flux to their surfaces. If transport is solely diffusive, then the flux is proportional to the local gradient. However, as discussed in [Geo15], gradient sensing is not equivalent to flux sensing when advection is also considered. Tracheal occlusion has been shown experimentally to enhance branching [Unb08]. [Geo15] investigated several mechanical hypotheses which might explain the mechanism of enhanced branching: (H1) the tissue stretch determined the local branch rate, (H2a) the concentration of morphogen determined the local branch rate, and

(H2b) the distribution of morphogen flux determined the local branch rate. They concluded that the locations of high stresses and strains from increased lumen pressure (H1) were not the locations of branching. Rather, the differing flux distributions on the epithelial surface (H2b) resulting from tracheal occlusion most directly indicated the location of branching tips and explained the increased branching of the occluded lungs. Advection was thus shown to be an important factor in morphogen transport in [Geo15]. However, for simplicity in this thesis, we ignore advection, so the flux is proportional to the gradient.

Through lung branching experiments on E11-E17 mice testing morphogen signaling and signal disruption, in [Met08] all three branching types were considered to have completely different generating mechanisms and the paper suggested that there may be a "rotator" mechanism. Specifically [Met08] suggested "each [branching mode] is controlled by a locally operative, genetic subroutine—a series of discrete patterning and morphogenesis events. Domain branching requires a proximal–distal ‘periodicity generator’ that sets the timing and spacing of branches within a domain, and a circumferential ‘domain specifier’ that dictates the positions of domains around the parent branch and the order in which domains trigger. Planar and orthogonal bifurcation require a branch ‘bifurcator’, and orthogonal bifurcation requires a ‘rotator’ that reorients the bifurcation plane by  $90^\circ$  between events. All subroutines require a ‘branch generator’" [Met08].

In comparison, the motivation in [GL18] "is to identify a unifying mechanism by which different branching modes may form. We hypothesize that geometric factors may influence the branching process, independently of molecular and mechanical influences." Using the simplified signaling model from [Geo15], in [GL18] it was shown that local geometry controls the flux morphogen distribution in a branching model lung. They concluded that hypothetically this single mechanism could explain the planar and orthogonal branching and showed many potential flux distributions based on local geometry ratios. Specifically, depending on simple geometric ratios, morphogen flux to the epithelium would be distributed in either a central "hot spot", a ring or annulus of higher flux, an elongated "hot spot" curve, or a pair of "hot spots" flanking the tip center.

We consider various three dimensional lung geometries and use the calculated morphogen flux

distributions on the epithelial surface to specify the growth function in a morphoelastic shell model of a growing lung epithelium. We use these models to evaluate hypotheses of shape changes from [GL18] using the signaling model of [Geo15] and [GL18].

## **5.2 Modeling Morphogenesis of the Embryonic Lung**

For our lung modeling, we considered the unique interaction between the shape, mechanics, and signaling systems inherent to a developing lung, specifically focusing on stage E12.5 mice, though our models are easily generalizable. In [GL18] it was hypothesized that: 1) if the morphogen flux to the epithelium was concentrated in a hot spot at an epithelial tip, tubule elongation would occur, 2) if morphogen flux was concentrated in a ring, tip flattening would occur, and 3) "when a single compact hot spot of morphogen flux splits into two compact hot spots we will see branching." However, shape changes were not explicitly modeled in that paper.

To test these shape-change hypotheses, we created a one-way coupled model that first solved a transport problem in the mesenchyme to determine the morphogen flux to the epithelium, and then grew the epithelium morphoelastically using growth stretch ratios proportional to the calculated local flux. Using the modeling framework developed in [GL18], we simplified lung histology, morphogen signaling, and geometry to construct a physically and biologically plausible, but simple model system. We used the geometry and signaling model from [GL18] as an input to a novel morphoelastic shell growth model (Sections 5.2.1-5.2.3). We considered the lung epithelium to be thin and maintain uniform thickness as it grows tangentially with transversely isotropic growth. We therefore adapted the morphoelastic framework to model the epithelium as a shell (Sections 5.2.4-5.2.6). Our modeling assumptions are explained in detail in the following sections.

### **5.2.1 Histological Assumptions**

Following the framework developed in [GL18], we simplified the histology of the embryonic lung to include just the mesothelial surface, mesenchyme, epithelium, and lumen. We modeled each tissue as a uniform continuum. This allowed us to model the epithelial tissue as materially isotropic.

We neglected mesenchymal growth and mechanics. We assumed the epithelium to be a uniform thin cell monolayer. We focused on mouse lung epithelial measurements at stage E12.5, though our method is generalizable.

### 5.2.2 Geometry Assumptions

Due to the complexity of the geometry of the lung we focus on a smaller region of interest at the tip of the lung bud where branching occurs. Following the logic established in [Kro19] and used in [GL18], we assume that the distal lung tips can be approximated as polygonal prism-shaped regions of interest packed in a polygonal array with any neighboring lung branch tips [Kro19]. We assumed that these prismatic regions of interest can be further geometrically simplified into circular or elliptical cross sections (Figure 5.2). For our models, the epithelium is represented in three dimensions as a

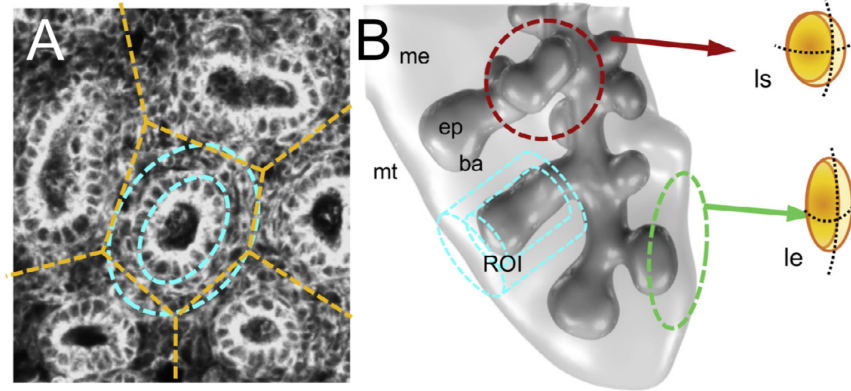


**Figure 5.2** Packing of lung buds. **A** displays the an example partitioning of a mouse lung into regions of interest. Simplified example regions of interest can be seen in subfigure **B**. These regions of interest further display the different curvatures of the mesothelial surface that occur in different regions of the developing lung. From [GL18].

capped elliptical or circular cylindrical shell nested in the larger solid capped elliptical or circular cylinder of mesenchyme, where the outer cap represents the local pleural or mesothelial surface. A cross section of an example region of interest is shown in Figure 5.3. Further discussion of the

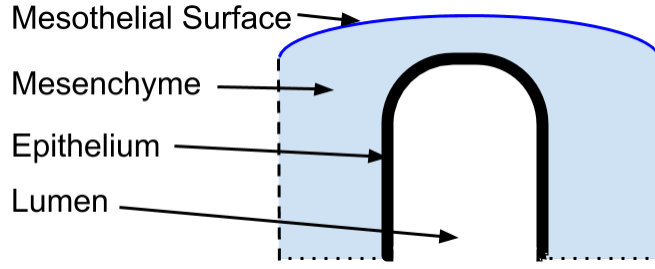


**Figure 5.3** Simplified histology of a single lung branch tip. Our simplified histology for a single lung branch tip includes the mesothelial surface, mesenchyme, epithelium, and lumen. The epithelium is a thin barrier tissue separating the mesenchyme from the lumen. Morphogens diffuse from the signaling mesothelial surface, represented by the blue line, through the mesenchyme, to be absorbed or bound on the epithelium, represented by the solid black line. Morphogen flux to the epithelium drives the shape change of the epithelium.

morphogen production and transport and its equations can be found in Section 5.2.3. Dashed boundaries in Figures 5.3- 5.5 represent the faces of the domain which are adjacent to other parts of the tissue.

Based on measurements from [Mai01] and [Jon19], we selected a representative range for the sizes of the various important geometric features in mouse embryos at stage E12.5 (Table 5.1). These features are shown in context in Figure 5.4. The distance  $L$ , from basal epithelial surface to pleural surface, is a key parameter in our models. In [Unb08],  $L$  was introduced as a function of time to quantify growth *in vivo*, and [Mai01] continues that practice. [Unb08] showed that as a lung tubule extends,  $L$  decreases to a minimum, at which time the tip splits and  $L$  increases. This measure  $L$  was shown in [GL18] to be critical to the control of morphogen flux patterning, and will be further

**Table 5.1** Lung bud measurements from [Mai01] and [Jon19]. All measurements were based on control, stage E12.5 mouse lungs.

Symbol	Description	Range ( $\mu\text{m}$ )
$\Phi$	epithelial thickness from basal to apical surface	5-25
$L$	distance from basal epithelial surface to pleural surface	17-35
$R_e$	distance across the lung bud including epithelial thickness	60-78
$R_M$	half the distance from epithelium in two adjacent lung buds	50-80

considered in this dissertation.

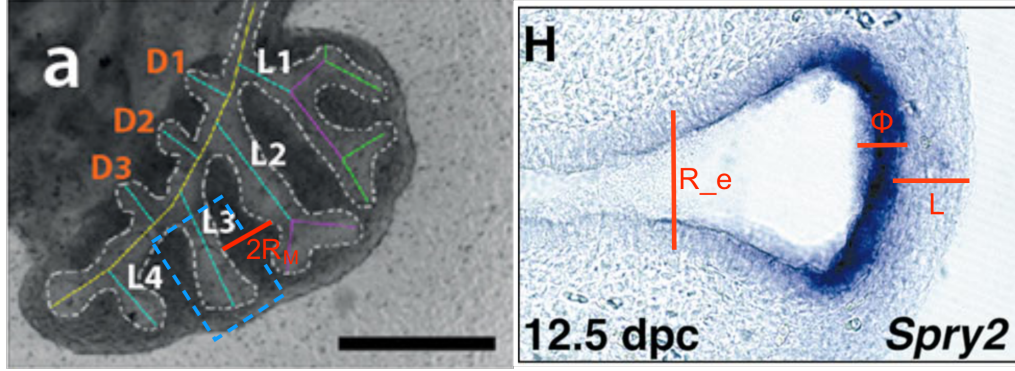


**Figure 5.4** Geometric measures in an E12.5 mouse lung annotated from [Jon19] left and [Mai01] right.  $2R_M$  is the full distance from one epithelial surface to another. We consider half this distance to be the location of the edge of our mesenchyme in our region of interest, where our region of interest can be considered to be the zone inside the blue dashed line.  $\Phi$  is the thickness of the epithelium, assumed to be constant.  $L$  is the distance between the basal epithelial surface and the pleural surface through the mesenchyme.  $R_e$  is the distance across the lung bud from basal epithelial surface to basal epithelial surface.

### 5.2.3 Morphogen Transport

To gain the most possible insight on the growth of the lung buds with the fewest variables, we simplified the complex interactions of biological signaling networks, following the model developed in [GL18]. We modeled the production, diffusion, and absorption of a single representative morphogen of concentration  $c$ . For simplicity, we ignore any advection, though it has been shown to affect flux distribution [Geo15]. An example cross-section of the local lung geometry displaying the boundaries and domain for the morphogen transport problem can be seen in Figure 5.5. In the 3D domain  $\Omega$ , the representative morphogen diffuses from the signaling surface  $\partial\Omega_p$ . Diffusion in a time-dependent

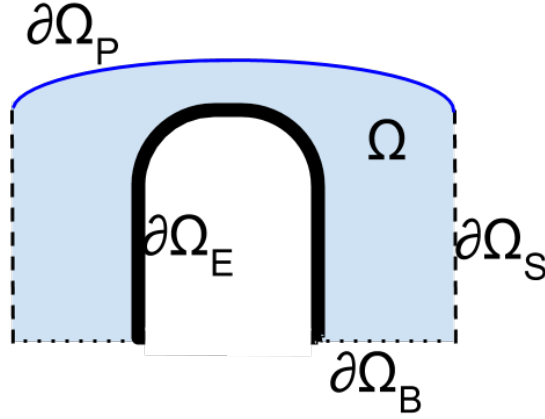


**Figure 5.5** Domain and boundaries for the transport model. In  $\Omega$ ,  $D\nabla^2 c = 0$ . The boundary condition for the pleural surface,  $\partial\Omega_P$ , is  $\hat{n} \cdot D\nabla c = k$ , meaning the morphogen is being produced at a constant rate represented as a constant flux. The boundary condition for the sides  $\partial\Omega_S$  and bottom  $\partial\Omega_B$  is  $\hat{n} \cdot D\nabla c = 0$ , because our region of interest has no net flux given that it is modeled as packing with its neighbors. The boundary condition for the epithelium,  $\partial\Omega_E$ , is given by  $c = 0$ , meaning all morphogen is assumed to be absorbed there.

system can be represented with the diffusion equation

$$\frac{\partial c}{\partial t} = D\nabla^2 c. \quad (5.1)$$

We assumed a constant and uniform diffusion coefficient  $D$  in the mesenchyme. However, we assumed a quasi-static state due to the much smaller time scale of diffusion relative to growth. Thus the diffusion equation simplifies to the Laplace equation, yielding

$$\nabla^2 c = 0. \quad (5.2)$$

The source of the representative morphogen is given by the boundary condition on the pleural surface. We model the pleural signaling surface,  $\partial\Omega_P$ , as having constant inward flux  $k$  of the representative morphogen. This is represented by  $\hat{n} \cdot D\nabla c = k$ .

Because we assume no net flux between similar regions of interest, the side faces of the local region of interest,  $\partial\Omega_S$ , have a no-flux boundary condition. Because we assume it is sufficiently



far from the signaling surface for flux to be negligible, the bottom boundary face,  $\partial\Omega_B$ , also has a no-flux boundary condition. For both  $\partial\Omega_S$  and  $\partial\Omega_B$ , this is represented by  $\hat{n} \cdot D\nabla c = 0$ .

Because we assume the representative morphogen to bind completely on the basal epithelial surface, the boundary of the epithelium,  $\partial\Omega_E$ , has a constant zero concentration of the representative morphogen,  $c = 0$ .

Together our transport system consists of

$$\nabla^2 c = 0 \quad \text{in } \Omega \quad (5.3)$$

$$\hat{n} \cdot D\nabla c = k \quad \text{on } \partial\Omega_P \quad (5.4)$$

$$\hat{n} \cdot D\nabla c = 0 \quad \text{on } \partial\Omega_S, \partial\Omega_B \quad (5.5)$$

$$c = 0 \quad \text{on } \partial\Omega_E. \quad (5.6)$$

We use this system to calculate the local flux  $j(X) = |\hat{n} \cdot D\nabla c|$  on  $\partial\Omega_E$ , which will drive the epithelial growth as discussed in Section 5.2.4.

## 5.2.4 Growth and Mechanics Model

To construct the system of partial differential equations for the mechanics and growth of our system, we needed to consider both the properties of the material we are growing and the correct growth formulation. To concisely convey anisotropic growth, we needed to first find a local coordinate system, and, since the epithelium is much thinner than it is long or wide, we chose shell theory as the basis of our mechanics model. Our modeling assumptions, theory, and implementation are described in greater detail in Chapter 2 and Sections 5.2.4.1-5.3.2.

### 5.2.4.1 Local Coordinates

Because the epithelium is often considered to be like sheet-like tissue acting as a boundary between the lumen and another tissue, we modeled the epithelium as a shell with no growth (change) in its thickness (Section 5.2.1). The growth is then no longer truly volumetric but rather can be

considered area growth. To represent this growth simply and concisely in three dimensions, we used a local orthogonal coordinate system,  $(\eta_1, \eta_2, \eta_3)$  (Figure 5.6), calculated by COMSOL as described in Section 3.1.2. Here  $\eta_3$  is normal to the shell surface and the  $\eta_1$  and  $\eta_2$  directions are tangent to the surface in the directions of maximum and minimum local curvature. Because we assumed lung

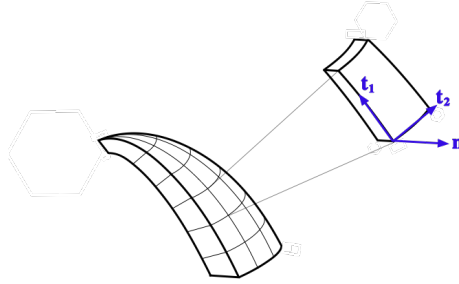


**Figure 5.6** Local orthogonal coordinates for the shell. The local coordinates  $(\eta_1, \eta_2, \eta_3)$  have corresponding unit vectors that are tangential in the direction of maximum curvature, tangential in the direction of minimum curvature, and normal to the shell surface, respectively. A representative shell piece is shown with its local coordinate system.

epithelial growth to be transversely isotropic with zero normal growth, the growth tensor  $\mathbf{G}$  from Equation 1.2.7 can now be represented in the local coordinates by

$$\mathbf{G}(\eta_1, \eta_2, \eta_3) = \begin{bmatrix} \lambda & 0 & 0 \\ 0 & \lambda & 0 \\ 0 & 0 & 1 \end{bmatrix}, \quad (5.7)$$

where  $\lambda$  is the stretch ratio in the tangential directions. The stretch ratio  $\lambda(\eta_1, \eta_2)$  is determined by the local morphogen flux,  $j(\eta_1, \eta_2) = \hat{n} \cdot (D \nabla c)$  on  $\partial \Omega_E$ . We scale these fluxes to specify the local growth stretch ratio

$$\lambda(\eta_1, \eta_2) = 1 + \frac{\epsilon_{\max} j(\eta_1, \eta_2)}{j_{\max}}, \quad (5.8)$$

where  $\epsilon_{\max}$  is the maximum value of the strain we want to impose and  $j_{\max}$  is the value of the largest local flux magnitude of any of the compared models. A value of  $\lambda > 1$  indicates growth, and  $\lambda = 1$  gives no change. The normal direction of the shell's growth is represented by the third entry of the diagonal of  $\mathbf{G}$  and remains 1, indicating that the shell does not change in thickness. If  $\lambda = 1$  the shell's volume is locally conserved since  $\det(\mathbf{G}) = \lambda^2$ .

### 5.2.5 Material Assumptions

As discussed in Section 1.4.1, the first mechanical assumption for our epithelial growth model is that all material properties are isotropic, meaning equal in every direction. The epithelial material is assumed to be elastically incompressible, meaning that in conditions where  $\det(\mathbf{G}) = 1$ , volume is conserved or  $\det(\mathbf{F}) = 1$ . In terms of the elastic deformation tensor  $\mathbf{A}$ , this material incompressibility means  $\det(\mathbf{A}) = 1$ . As previously explained in Section 1.4.3, due to the large deformations, the material is modeled as hyperelastic. The exact constitutive laws for the epithelium are not known, and difficult to determine experimentally, as straining the material initiates biological responses which can change the materials' response [Fun84], [Fun65].

### 5.2.6 Shell Mechanics

Shell theory is a subset of structural mechanics materials that are much thinner in one direction relative to the others, and the equations from Section 1.4.2.1 still hold, but with some additional assertions. Commonly used shell formulations include the Donnell-Mushtari model and the Byrne-Flügge-Lur'ye model [Com], [CB11], [Sch85], [Smi05]. In general, thin shell formulations ignore transverse shear, so plane sections normal to the midsurface remain normal to the midsurface after deformation. Thick shell theories do not usually utilize this constraint. In most circumstances, composite materials and materials with high ratio of thickness to span should be modeled as thick materials. Since for our modeling purposes we are considering the epithelium of the growing lung to be a shell and most measurements of epithelial cells give a thickness of approximately 5-24  $\mu\text{m}$  [Mai01], [Jon19], while the length of the minor axis of the epithelium ranges in our models from

40 to 80  $\mu\text{m}$ , we used Mindlin-Reissner thick shell theory, an extension of Mindlin-Reissner plate theory. This shell theory is a built-in model in our finite elements package COMSOL in the Structural Mechanics module. Along with the standard mass and momentum conservation equations, we also need to describe the stresses. The membrane stress,  $\sigma_m$ , is described by

$$\sigma_m = \mathbf{C}[\gamma - \epsilon_G], \quad (5.9)$$

where  $\gamma - \epsilon_G$  describes the elastic strain in the membrane and  $\mathbf{C}$  is the Cauchy stress tensor and  $\epsilon_G$  is the strain due to growth in the membrane and is a function of the stretch ratios we input. The bending stress is given by

$$\sigma_b = \frac{\mathbf{C}\Phi}{2}[\chi - \epsilon_G], \quad (5.10)$$

where  $\Phi$  is the shell thickness and  $\chi - \epsilon_G$  is the elastic strain in the bending direction. The  $\epsilon_G$  is the strain due to growth in the bending direction and is a function of the stretch ratios we input and is the same as the strain in the membrane direction. The average transverse shear stress is described by

$$\sigma_s = \frac{5}{6}2G(\zeta - \zeta_0), \quad (5.11)$$

where for our model  $\sigma_k = 0$ ,  $G$  represents the transverse shear modulus,  $\zeta - \zeta_0$  is the elastic strain in that direction, and 5/6 is a MITC correction factor, described in detail in Appendix B. The in-plane stress is given as a combination of the membrane stress and the bending stress where

$$\sigma_{\text{inplane}} = \sigma_m + \tilde{z}\sigma_b \quad (5.12)$$

such that  $\tilde{z}$  describes the scaled location in the thickness direction  $\eta_3$ , and ranges from -1, the apical surface, to 1, the basal surface of the shell as shown in Figure 5.7. Midsurface, the surface that is halfway between the apical and basal surfaces, is considered to always be at  $\tilde{z}=0$ . More detailed information about shell models can be found in [Smi05] [CB11].

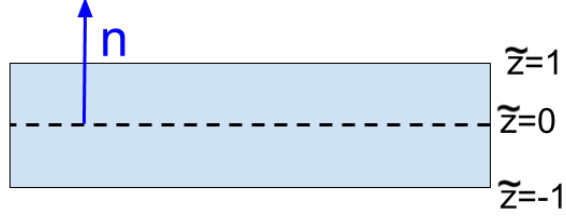


**Figure 5.7** Location in shell. The bottom or apical surface is considered to be located at  $\tilde{z} = -1$  and the top or basal at  $\tilde{z} = 1$ . In this two dimensional figure, the midsurface is represented by a dotted line. In thin shells planes normal to the midsurface, with the normal direction represented by the blue arrow in this two-dimensional simplification, remain normal to the midsurface even after deformation. In thick shells, that is not necessarily the case. For our model, we consider the positive normal direction to be oriented away from the lumen towards the mesothelial surface, or apicobasally.

To summarize our specific lung framework,

$$\mathbf{F} = \mathbf{A}\mathbf{G} \quad \text{deformation gradient tensor,} \quad (5.13)$$

$$\mathbf{G}(\eta_1, \eta_2, \eta_3) = \begin{bmatrix} \lambda & 0 & 0 \\ 0 & \lambda & 0 \\ 0 & 0 & 1 \end{bmatrix} \quad \text{growth tensor,} \quad (5.14)$$

$$\lambda(\eta_1, \eta_2) = 1 + \frac{\epsilon_{\max} j(\eta_1, \eta_2)}{j_{\max}} \quad \text{stretch ratio,} \quad (5.15)$$

with  $\mathbf{F}$  and  $\mathbf{A}$  determined by the model framework in Chapter 2 as seen in Equations 2.2 and 2.9, and  $j$  determined by the morphogen transport system described in Section 5.2.3.

### 5.3 Numerical Experiments

We modeled the representative morphogen transport, and its associated growth in many different regions of interest. The only differences between our models are the geometric definitions: signalling distance  $L$ , transverse aspect ratios, and shell thicknesses  $\Phi$ . One of the main geometric measures of interest is the signaling distance  $L$ , specifically the distance from the pleural signaling surface to the basal epithelial surface.  $L$  changes dynamically *in vivo* [Jon19] [Mai01] [Unb08] and has been

shown to affect the morphogen flux distribution [GL18]. However, differential growth due to the different flux distributions caused by interactions between by  $L$  and the geometry of the region of interest, has not been explicitly modeled. Following the framework in [GL18], to test its hypotheses of the lung tip shape changes, we compared regions of interest with the same cross-sectional shape but different distances  $L$ .

### 5.3.1 Geometry Definitions

To test the geometric control of morphogenesis, the local geometry of each of the models varies several geometric parameters, illustrated in Figure 5.8.  $L$  is the pole-to-pole distance between the pleural surface and the basal surface of the epithelium. The lengths of the minor and major axes of the outer ellipse are  $A_1$  and  $A_2$  respectively. The lengths of the minor and major axes of the inner ellipse are  $a_1$  and  $a_2$  respectively. For consistency, the cross-sectional area ratio of the inner ellipse to the outer ellipse  $\frac{a_1 a_2}{A_1 A_2}$  was held at 0.25. For ease of comparison, we stayed within the geometric parameter range in [GL18] where the lengths of the major and minor axes of the epithelium were 40-80  $\mu\text{m}$ , the major and minor axes of the mesenchyme were 100-200  $\mu\text{m}$ , and  $L$  was 10-40  $\mu\text{m}$ .

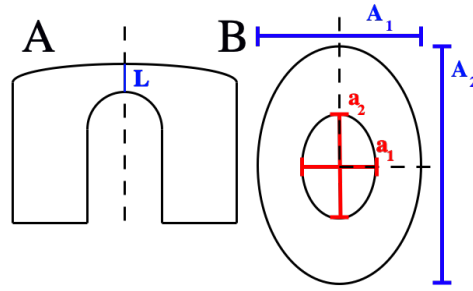


**Figure 5.8** Sketch of lung ROI geometry. (A) The cross section view shows a dotted line of symmetry and the polar distance between the pleural and basal epithelial surface  $L$ . (B) Other geometric parameters of interest are the minor axis of the inner ellipse,  $a_1$ , the major axis of the inner ellipse,  $a_2$ , the minor axis of the outer ellipse,  $A_1$ , and the major axis of the outer ellipse,  $A_2$ . Axes of reflection symmetry are represented by dotted lines.

### 5.3.2 Boundary Conditions for Growth and Stresses

The model required additional assumptions on the mechanics of our system. We assumed no external pressure, and all surface faces were unstressed, so  $\hat{n} \cdot \sigma = 0$  for all boundaries. For our model lung geometries, there exists at least one plane of symmetry. We therefore modeled a half domain to save computational time and facilitate visualization. Each of these cut faces had a symmetry boundary condition imposed. This means that none of these faces were allowed to rotate and that normal displacement to the  $xz$ -plane can be described by the displacement vector  $\hat{u}(x = 0) = 0$ . Figure 5.9 shows the boundary condition on a cut plane. Additionally, the bottom of the stalk  $\partial\Omega_{SB}$ , while not considered to be on a plane of symmetry, also has no normal displacement, so for displacement vector in the Cartesian coordinate system  $\hat{u}(z = 0) = 0$ .

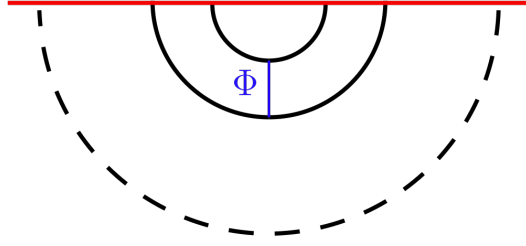


**Figure 5.9** Boundary condition on cut plane. For a top down view, with  $\Phi$  displaying the thickness of the shell, we have a plane of symmetry in red. All surfaces of the shell are under no stress, the surfaces touching the cut plane cannot move normal to the plane or rotate, and bottom surface of the plane also has no normal displacement.

### 5.3.3 Case 1: Axisymmetric

For our first numerical experiment, we used axisymmetric geometry with an epithelial shell thickness of  $15\text{ }\mu\text{m}$ . The mesenchyme was set to an outside diameter of  $A_1 = A_2 = 120\text{ }\mu\text{m}$ . The epithelium had basal diameter measurements of  $a_1 = a_2 = 60\text{ }\mu\text{m}$ , corresponding to a lumen diameter of  $30\text{ }\mu\text{m}$ . As observed in [GL18], as  $L$  decreases, the morphogen flux distribution pattern changes from a circular hot spot region to an annular region (Figure 5.10), which we confirmed as shown in Figure 5.11. It was hypothesized in [GL18] for this geometry that a circular morphogen flux distribution pattern would lead to extension, and an annular morphogen flux distribution pattern would lead to dimpling or flattening of the tip of the tubule or lung bud.

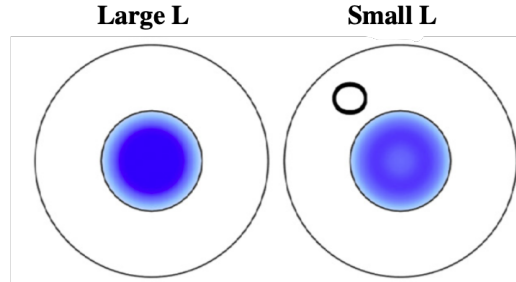


**Figure 5.10** Local ROI geometry of a cylindrical epithelium tubule nested in a larger cylindrical mesenchyme and its morphogen flux distribution pattern. As  $L$  decreases, the circular morphogen flux hot spot becomes a morphogen flux ring, denoted by "O". The authors of [GL18] hypothesized that a circular morphogen flux distribution pattern would correspond to tubule extension, while an annular morphogen flux distribution pattern was hypothesized to result in the the tip of the tubule dimpling or flattening. As annotated from [GL18].

Figure 5.11 shows the calculated deformations for several values of  $L$ . Darker areas represent higher growth, scaled the same across all three simulations so that the largest growth magnitude of the compared simulations nearly doubles the local area. Supporting one hypothesis put forward in [GL18], larger values of  $L$  resulted in a circular morphogen flux hot spot and extension of the lung bud towards the pleural surface. Extremely low values of  $L$  replicated the annular flux region found in [GL18] but the tubule did not noticeably flatten.



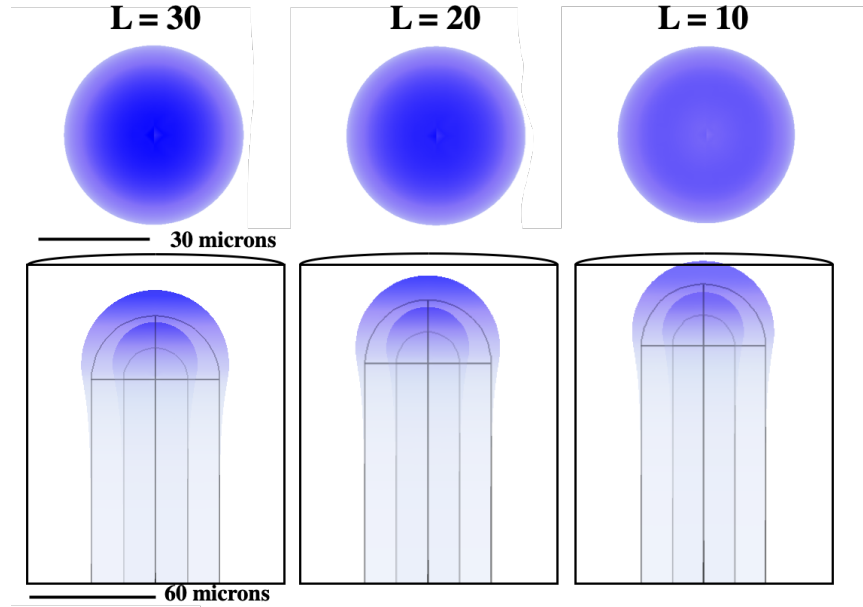
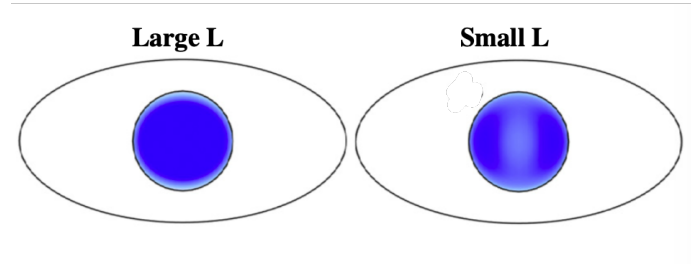


**Figure 5.11** Flux and growth of epithelium of circular cross section inside a mesenchyme of circular cross section. As previously defined,  $L$  is the distance between the basal epithelial surface and the pleural surface in  $\mu\text{m}$ . In the local cross-sectional geometry of an epithelium of circular cross section nested in a mesenchyme of circular cross section with a cross-sectional area ratio of 1:4, we considered several  $L$  values. Higher normal flux magnitude is displayed in darker colors. Larger values for  $L$  lead to a circular flux distribution pattern and epithelial extension towards the pleural surface, while small values of  $L$  lead to an annular region of higher flux magnitude and epithelial extension but no perceptible flattening.

#### 5.3.4 Case 2: Circular Epithelial Cross Section Inside Elliptical ROI Cross Section

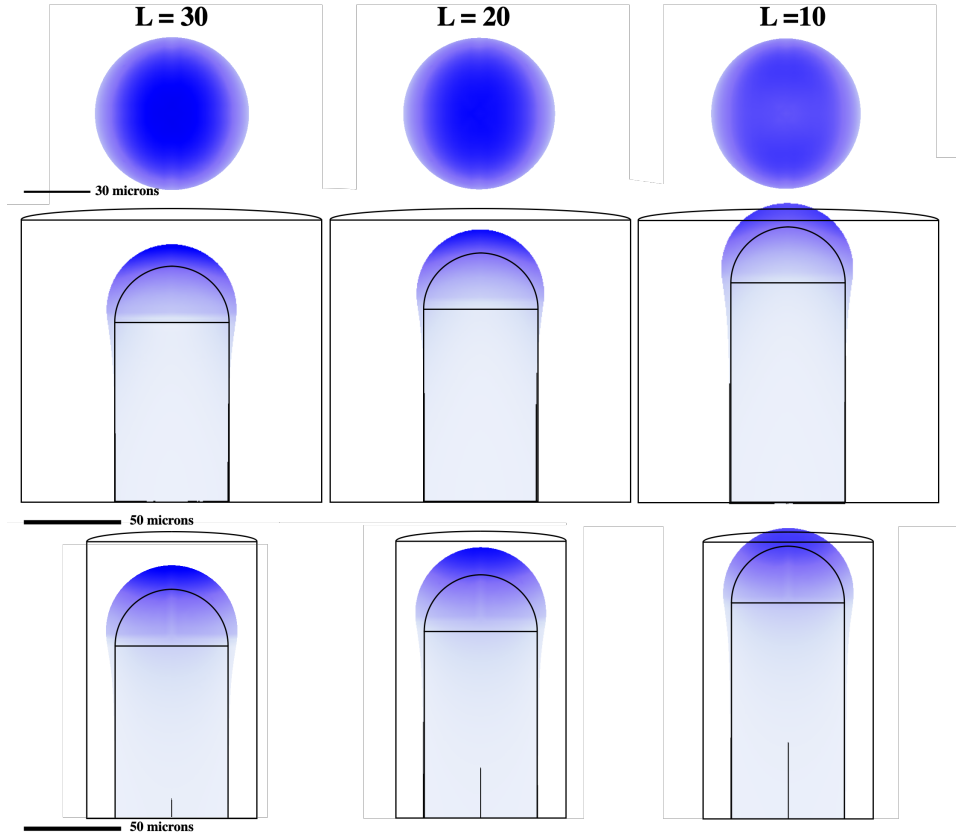
We also modeled an epithelium of circular cross section inside a mesenchyme of elliptical cross section, with epithelial shell thickness of  $15 \mu\text{m}$ . The epithelial outer radius was  $30 \mu\text{m}$ . The mesenchyme's minor axis was  $90 \mu\text{m}$  and the major axis was  $160 \mu\text{m}$ . As seen in Figure 5.12, [GL18] showed that for this geometry large  $L$  would result in a circular hot spot, while for a small  $L$  the hot spot would split. *In vitro* lung observations of FGF10 distribution have shown that a small  $L$  changes morphogen distribution towards these shouldering areas and away from the tip [Bel97]. The authors hypothesized in [GL18] that larger  $L$  values with their single hot spot would lead to

epithelial extension, while a small  $L$  value with its two localized areas of greater flux magnitude was hypothesized to lead to epithelial tip splitting or shouldering [GL18]. *Shouldering* refers to the widening and transverse flattening of the tip of a lung bud.



**Figure 5.12** Epithelium of circular cross section inside a mesenchyme ROI of elliptical cross section. Large values of  $L$  result in circular hot spots, while a small  $L$  value shows a split in the area of high flux distribution. In [GL18], the authors hypothesized that single hot spots for this geometry would cause extension of the epithelium, while tip splitting or branching of the epithelium is hypothesized to occur for split hot spots when an epithelium of circular cross section is inside a mesenchyme of elliptical cross section. Image annotated from [GL18].

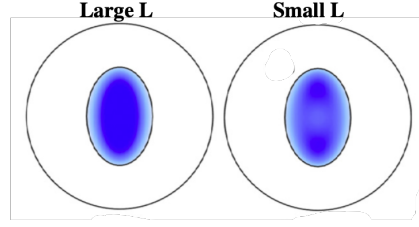
We replicated the results in [GL18] that extremely low values of  $L$  lead to a split in of the morphogen flux region (Figure 5.13). Our model results support the hypothesis made in [GL18] that larger values of  $L$  result in extension of the lung bud towards the pleural surface. Furthermore, our model shows some curvature changes after growth, which implies that over time this particular geometry may result in branch splitting.



**Figure 5.13** Flux and growth of epithelium of circular cross section inside a mesenchyme of elliptical cross section. We observed that at the smallest  $L$  value the flux distribution pattern splits into two zones, as shown in [GL18]. However, we did not observe shouldering given the split morphogen flux distribution in this simulation. We found that all  $L$  values and their different morphogen flux distributions corresponded to extension.

### 5.3.5 Case 3: Elliptical Epithelial Cross Section Inside Circular ROI Cross Section

We also considered an epithelium of elliptical cross section with a minor axis of  $64 \mu\text{m}$  and major axis of  $100 \mu\text{m}$  inside mesenchyme of circular cross section with a radius of  $80 \mu\text{m}$ . The cross-sectional area ratio remained at 1:4. The epithelial thickness was  $15 \mu\text{m}$ . It was shown in [GL18] that in this local geometry small values of  $L$  would lead to two shouldered flux hot spots and they hypothesized that this would lead to growth shouldering or tip splitting of the lung tubule end. Their calculated flux distributions are shown in Figure 5.14.



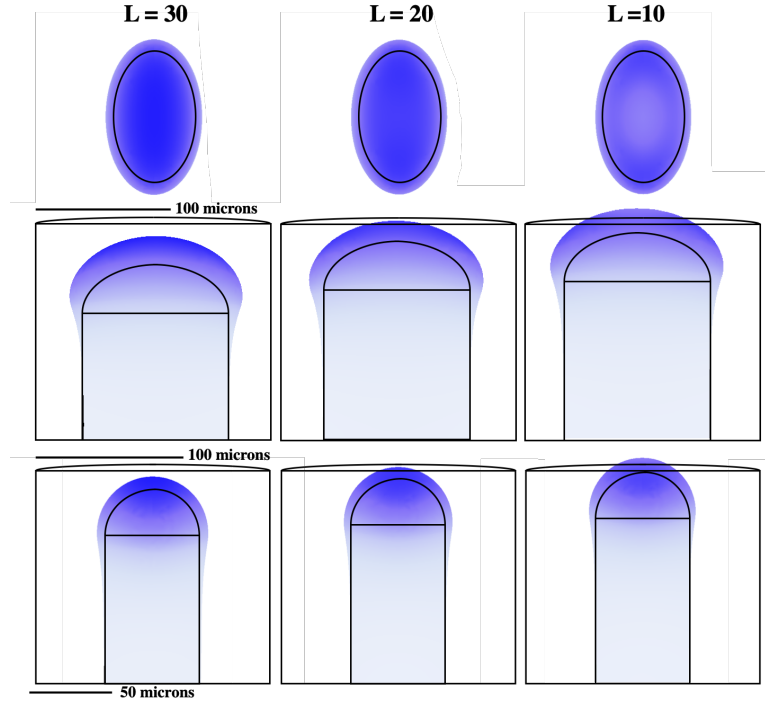
**Figure 5.14** Epithelium of elliptical cross section in a mesenchyme circular cross section. The flux distribution splits into two hot spots as  $L$  decreases. In [GL18], tip splitting or branching is hypothesized to occur for split flux distributions, like that seen when  $L$  is small in a local geometry of an epithelium of elliptical cross section is inside a mesenchyme of circular cross section. Larger  $L$  values for this geometry cause a single hot spot. This hotspot is hypothesized to lead to epithelial extension towards the pleural surface. Image annotated from [GL18],

Figure 5.15 shows our results for the flux magnitude and deformation for several values of  $L$ . We observe the split into two morphogen flux hot spots as  $L$  decreases, verifying the morphogen flux results from [GL18]. For our model all  $L$  values show some shouldering of the grown epithelium regardless of the flux distribution being either one or two hot spots, which was not hypothesized in [GL18]. There is extension occurring along the major axis of the epithelium's elliptical cross section at the top of the tubule without much expansion along the minor axis, so the aspect ratio of the ellipse is increasing at the tip. Specifically, the tip is getting wider in its major axis direction. Additionally at smaller  $L$  values, some slight changes of curvature at the tip can be observed.

### 5.3.6 Case 4: Elliptical Epithelial Cross Section Inside Elliptical ROI Cross Section

We considered the local geometry of an epithelium of elliptical cross section with a minor axis of  $50 \mu\text{m}$  and major axis of  $64 \mu\text{m}$  nested in a mesenchyme of elliptical cross section with a minor axis of  $80 \mu\text{m}$  and a major axis of  $160 \mu\text{m}$ . Shell thickness is maintained at  $15 \mu\text{m}$ . As shown in Figure 5.16, it was hypothesized in [GL18] that single hot spots, like those observed for larger values of  $L$ , would cause extension. However, smaller values of  $L$  were shown to lead to local flux hot spots and it was hypothesized that these split hot spots would cause shouldering. We replicated the shape of the morphogen flux distributions found in [GL18] for this case as well (Figure 5.17).

Figure 5.17 shows the growth proportional to these morphogen flux distribution patterns for



**Figure 5.15** Flux and growth of epithelium of elliptical cross section inside a mesenchyme of circular cross section. In the specific region of interest of an epithelium of elliptical cross section inside a mesenchyme of circular cross section with cross-sectional area ratio of 1:4, we considered  $L = 10, 20, 30 \mu\text{m}$ . Darker colors correspond to higher local values of normal flux magnitude. Single morphogen flux hot spots, corresponding to higher  $L$  values, showed considerable extension towards the pleural surface.

several values of  $L$ . From our simulations there appears to be shouldering of growth for all values of  $L$  but based on the flux distribution, we would hypothesize that branching would occur over time for epithelium closer to the pleural surface due to the clear split in distribution for the flux.

### 5.3.7 Varying Epithelial Thickness

For our original purposes of verifying the morphogen flux distribution patterns in [GL18] and testing the authors' hypotheses on growth of a lung tubule, a representative epithelial thickness of  $\Phi = 15 \mu\text{m}$  was used throughout the simulations shown in 5.3-5.3.6. However, this was just a representative

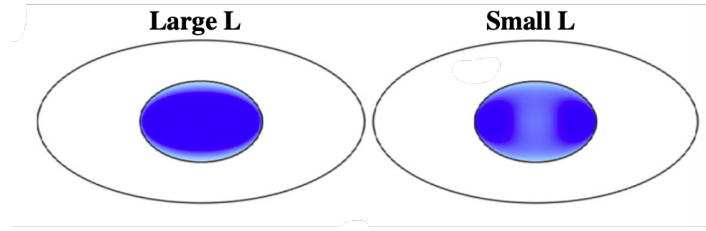


**Figure 5.16** Flux distribution of an epithelium of elliptical cross section inside a mesenchyme of elliptical cross section. In [GL18], single morphogen flux hot spots, seen for the larger  $L$  values, for this geometry are hypothesized to lead to epithelial extension towards the pleural surface, while tip splitting or branching of the epithelium is hypothesized to occur for split morphogen flux hot spots, seen for smaller  $L$  values, when an epithelium of elliptical cross section is inside a mesenchyme of elliptical cross section. Image annotated from [GL18].

value to give insight on a complicated biological system. Changing the  $\Phi$  value through a range that we observed in [Mai01] leads to significantly different shape changes. Figure 5.18 shows the differences caused by varying epithelial thickness when  $L = 10 \mu\text{m}$  for the same capped elliptic cylinder epithelium and capped elliptic cylinder mesenchyme model considered in Section 5.3.6. These differences are subtle in the side views but clear in the top view. The cross-sectional aspect ratio of the shell is different for the different thicknesses after growth. With less thickness, the shell undergoes more shape change. The thin shells shoulder and flatten more than the thick shells do.

We note that care must be taken to construct an appropriate geometry in COMSOL, as it explicitly defines only one surface of the shell, which in our models is the basal surface. COMSOL generates the other surface of the shell, the apical surface, by mapping every point from the defined (basal) surface using a vector normal to the defined (basal) surface, whose length is the shell's thickness. We observed that for our thicker shells with  $\Phi = 15 \mu\text{m}$ , it was possible to have simulations that self-intersected both before and after growth depending on the local geometry (Figure 5.19). Surprisingly, self intersection did not prevent convergence of the simulations.

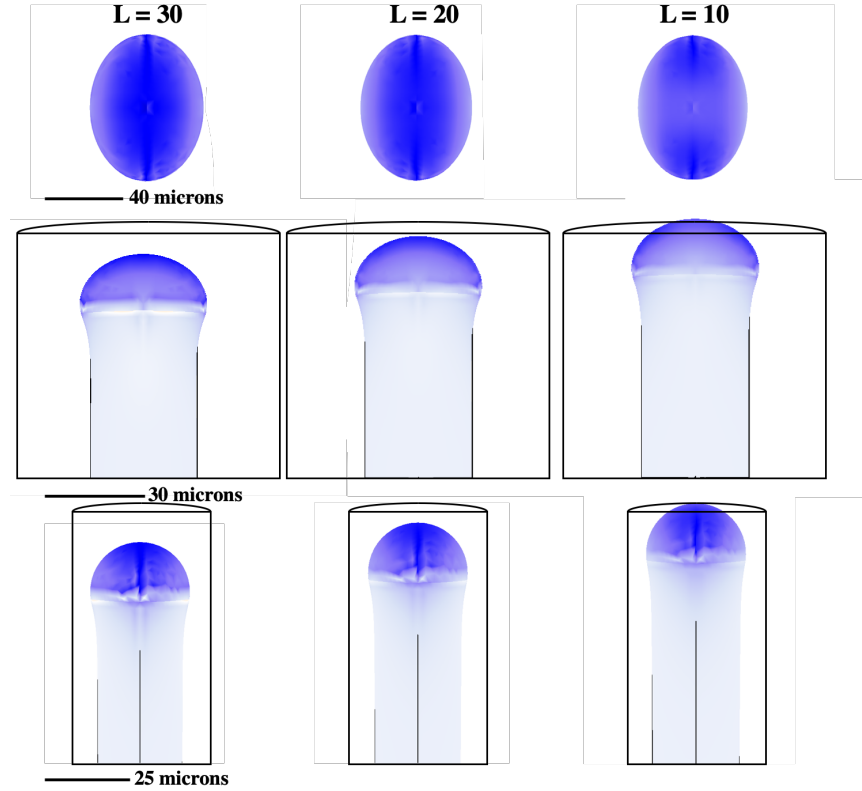


**Figure 5.17** Flux and growth of epithelium of elliptical cross section inside a mesenchyme of elliptical cross section. Our flux distribution matches that seen in [GL18]. Extension of the tubule is seen with single morphogen flux hot spots, seen for the large  $L$  values, and some shouldering occurs with all values.

## 5.4 Conclusions

Our models focused on the interplay between signaling, geometry, and growth. Many published models have been focused on the complex signaling networks like [Unb08],[Jon19], [War05], [Mai01], [Nye08] and some have modeled pseudo-growth using a "growth velocity" normal to the surface [MI12], [Ger11]. Based on the work done in [Geo15] [GL18], in this chapter we tested their hypotheses on the relationship between local geometry, local flux distribution, and growth. We created one of the first morphoelastic shell models [Ton06] to explicitly model this phenomenon. We concluded that different local flux distributions, as created from different local geometries, affect growth.

Specifically for the axisymmetric case, we verified that the morphogen flux distribution pattern changed from a circular to annular region as found in [GL18]. However, we did not confirm their hypothesis that significant flattening of the tip would result from an annular morphogen flux region. Consistent with [GL18]’s hypothesis, we did observe some shouldering and flattening of the epithelial tips as the morphogen flux distribution became either elongated or split into separate local hot spots for regions of interest where the mesenchyme or epithelium was of elliptical cross section. Additionally, we found that epithelial thickness, within the range observed *in vivo*, affects the growth shape changes for non-axisymmetric cases. However, care must be taken when considering shell models, as simulations can converge that self-intersect. These models are biologically relevant as they provide insight on an extremely complex process. Our work supports the idea that there are not many different mechanisms that cause branching, as suggested in [Met08], but rather, as investigated in [GL18], local geometry can explain differences in shape change. Additionally, these simulations and conclusions may aid in identifying and explaining the relationship between morphogen expression and developmental lung abnormalities. Further discussion of our results and possible extensions can be found in Chapter 6.



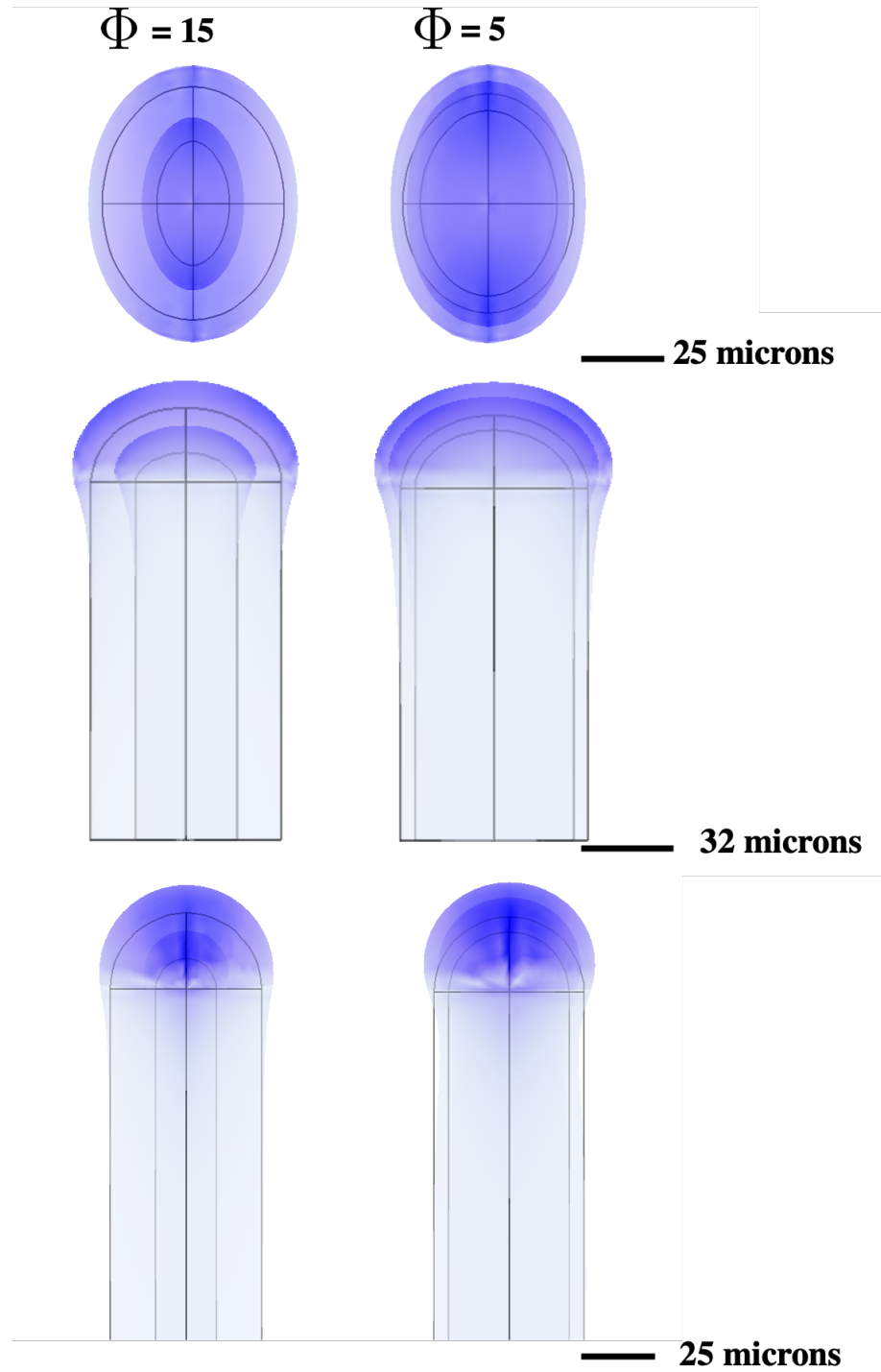


**Figure 5.18** Differences in shape change caused by varying epithelial thickness. Comparing the thickness of the epithelium from  $\Phi = 15 \mu\text{m}$  to  $\Phi = 5 \mu\text{m}$ , we observed that epithelial thickness caused variation in shape change due to growth. Notice that as seen from the top for  $\Phi = 5 \mu\text{m}$  the shell changed its cross-sectional aspect ratio much more significantly than for  $\Phi = 15 \mu\text{m}$ .

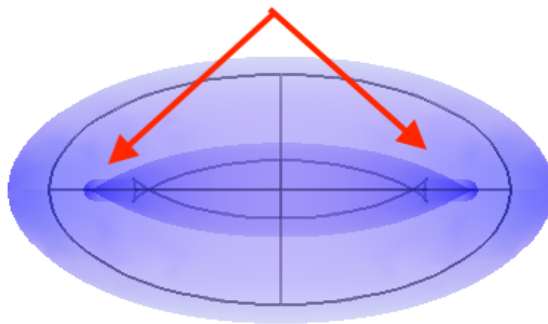


**Figure 5.19** Self intersection due to epithelial thickness and interaction with overall shape. For an epithelial cross section with minor axis  $20\ \mu\text{m}$  and major axis  $40\ \mu\text{m}$  and thickness of  $\Phi = 15\ \mu\text{m}$ , simulations converge but the shell self-intersects. This is not biologically realistic.

## CHAPTER

# 6

## DISCUSSION

In this dissertation we used the relatively new continuum framework of morphoelasticity to model shape change in two separate morphogenetic model systems. Many previous models in developmental biology focus on the complex signaling processes while neglecting shape change and mechanics. In this thesis, we used simple signaling assumptions to drive rationally defined shape changes.

### **6.1 Stomach Bending**

As the embryonic stomach develops, LR asymmetry is generated, which is caused by asymmetric gene expression [Dav17]. However, we do not know the exact manner in which these asymmetrically expressed genes, such as *Foxj1*, actuate the shape change. In Chapter 4, we investigated whether volume-preserving or non-volume-preserving, isotropic or anisotropic growth would lead to shape

changes consistent with shape changes that have been observed in the developing frog stomach [Dav17].

Because we considered both sides to be growing, we modeled the growth of the left side relative to the right side. We modeled the right side as simply growing isotropically, so in order to create asymmetry, the left must grow differently from the right. We determined that distinguishing between the inner and outer layers of the embryonic stomach was unnecessary to identify the core morphogenetic phenomena. We modeled increased isotropic growth of the left side, corresponding to increased isotropic mitosis on the left. The expected shape change, as observed experimentally, is bending from the left side to the right when combined with radial thinning. Shape change from this isotropic growth assumption was not consistent with observations from embryonic frog as it neither bent in the correct direction or thinned radially, so we concluded that there must be an anisotropic component to growth.

We considered non-volume-conserving anisotropic growth where we modeled increased left-side growth in each of our local coordinate directions separately. This corresponds to increased mitosis through oriented cell divisions in just one direction of the left stomach. While an assumption of left axial lengthening gave shape changes that were most consistent with the observed shape change in frogs, none of the directional mitotic growth results truly matched the stomach's shape. We concluded that increased mitotic growth of the left side alone cannot explain the observed deformation. We therefore considered volume-conserving anisotropic growth, corresponding to cell intercalation on the left side of the stomach. The shape change observed with axial lengthening balanced by radial thinning is most consistent with what is observed in the frog stomach. We concluded that the primary agent of curvature change in the stomach must be cell rearrangement on the left side, specifically including radial thinning.

Careful measurements would need to be done in the pseudo-cylindrical coordinates to further quantify the shape change *in vivo*. We suggest that future experiments focus on cell rearrangement, particularly in the axial and radial directions.

## 6.2 Lung Branching

The many molecular factors, including growth factors such as FGF10, that govern embryonic lung morphogenesis have been well studied [Jon19], [War05], [Mai01], [Nye08]. Morphogen flux distributions have been shown to correlate to the location of branching [Geo15]. These morphogen flux distributions were shown in models to be dependent on local geometry, but flux-regulated growth was not explicitly modeled in [GL18]. In Chapter 5, we developed one of the first morphoelastic shell models, and applied it to the question of epithelial shape change in the pseudo-glandular stage of the lung using the simple signaling model developed in [Geo15] and [GL18]. Morphoelastic shell modeling is an emerging area of modeling and has been applied previously in other systems, such as fungi [Ton06].

We verified the effects of local geometry on the morphogen flux on the epithelium shown in [GL18]. For the axisymmetric case, we verified that the morphogen flux distribution pattern changed from a circular to annular region. However, we failed to confirm the hypothesis from [GL18] that significant flattening of the tip would result from an annular morphogen flux region for all of the shell thicknesses we tested. Consistent with one of their other hypotheses, we did clearly observe shouldering of the epithelial tips as the morphogen flux distribution became either elongated or split into separate local hot spots for regions of interest where the mesenchyme or epithelium was of elliptical cross section. We also concluded that the thickness of the shell is an important feature contributing to the resulting shape change for these geometries. We observed thin shells to shoulder and flatten significantly more than thick shells.

Given that lung epithelia do not remain a monolayer, or even have a uniform thickness during growth [Mai01], an extension to our research would include considering a non-uniformly thick epithelium with non-constant stiffness. Based on images from [Mai01], the epithelium appears to be thinner along the stalk particularly where the stalk meets the curved "head" of the lung bud. This thinness could lead to buckling in that region. We believe that thickness changes would yield a saddle shape on the basal epithelial surface that would better show the beginnings of branching

rather than the convex shapes we found.

The distance between the basal epithelial surface and the mesothelial surface of the lung changes over time [Bel97] [Mai01] [Jon19] but the surfaces do not come in contact. We neglected the mesenchymal mechanical resistance and mesenchymal growth but future work could include it. The mesenchyme has been previously modeled as a fluid in [Wan07] and a viscous medium in [CM14] and any stiffness of this medium will have an effect on epithelial shape change as it resists the growth.

### **6.3 Further Extension**

A further extension of this work would be to consider multiple time steps. Also, the growth from a single large strain in a body, as a stand-in for growth over time, is not equivalent to the growth from applying strains to a body continuously over time. Biological tissues can undergo strain-stiffening, develop residual stresses, and remodel [Fun65], [Gor17] [Bel75] [BG06]. As the region of interest grows, the morphogen transport would also change. A model that considered multiple time steps (or continuous time) would need to make assumptions about how much these residual strains remain or dissipate. Shape change over time has been previously modeled where the residual stresses completely dissipate, as was introduced in [LM95]. In order to be correctly formulated, a time-dependent model would have to include energy-dissipation terms, would likely consider viscoelasticity, and would need additional equations relating them. Also in order to accomplish this, remeshing of the deformed geometry would be required at every time step due to the potentially large distortions of the geometry. Remeshing complicated geometries can cause several issues with the mesh that would have to be resolved at every time step; mesh elements can become inverted, become overly large and therefore introduce error, or intersect. We have shown in Chapter 5, that self-intersection did not necessarily mean a simulation would not converge in COMSOL and must be manually searched for. There have been analyses of remeshing in COMSOL, but not for the shell module [Ger11].

## 6.4 Conclusion

In conclusion, we have used the mathematical framework of morphoelasticity to test hypotheses in two biological systems. Morphoelasticity provides the rigor of rational mechanics in modeling and, when carefully implemented, provides an important tool for understanding how signaling leads to specific shape changes. We created models that included morphoelasticity with isotropic and anisotropic growth, local coordinate systems, and large deformations. With this modeling framework, we were able to conclude from our models that creation of the asymmetry of the stomach as seen *in vivo* cannot be described by mitosis alone even with anisotropy in the cell division. We showed that cell rearrangement or oriented cell division is essential for stomach bending. For the lung bud models in particular, we also used thick shell theory coupled to a morphogen transport system. Our lung morphogenesis models provided insight on the importance of local geometry and the mechanics of growth during the pseudoglandular period and are the first models to utilize the area growth of the epithelium modeled as a morphoelastic shell.

These two different modeling approaches of solid mechanics for the combined endoderm and mesoderm of the stomach, and shell mechanics for the thin, sheet-like epithelium can be generalized for many other organ systems. Specifically, asymmetry also occurs in organs like the liver [Wom18] and the heart [Now06] that also show *Pitxc2* expression. Similar branching patterns to the lungs occur in the salivary glands and the kidneys as well. However, like previous lung branching models, robust modeling has been done for the signaling but not necessarily for growth in these tissues [IM13], and our approach could be applied to these cases. Morphoelasticity is a promising new framework in morphogenesis that is already allowing us to draw conclusions about complex biological systems.

## BIBLIOGRAPHY

- [Bar17] Barton, D. L. et al. “Active vertex model for cell-resolution description of epithelial tissue mechanics”. *PLOS Computational Biology* **13** (2017), pp. 1–34.
- [Bat89] Bathe, K.-J. et al. “The MITC7 and MITC9 plate bending elements”. *Computers and Structures* **32.3** (1989), pp. 797–814.
- [Bat90] Bathe, K.-J. et al. “Displacement and stress convergence of our MITC plate bending elements”. *Engineering Computations* **7.4** (1990), pp. 291–302.
- [Bel97] Bellusci, S. et al. “Fibroblast growth factor 10 (FGF10) and branching morphogenesis in the embryonic mouse lung”. *Development* **124** (1997), pp. 4867–4878.
- [BG06] Beloussov, L. V. & Grabovsky, V. I. “Morphomechanics: goals, basic experiments, and models”. *Journal of Developmental Biology* **50.2** (2006).
- [Bel75] Beloussov, L. V. et al. “Mechanical stresses and morphological patterns in amphibian embryos”. *Journal of Embryology and Experimental Morphology* **34.3** (1975), pp. 559–574.
- [Bla17] Blanchard, G. B. “Taking the strain: quantifying the contributions of all cell behaviour to changes in epithelial shape”. *Philosophical Transactions of the Royal Society of London* **372** (2017).
- [CB11] Chapelle, D. & Bathe, K.-J. *The finite element analysis of shells - Fundamentals*. Ed. by Bathe, K.-J. 2nd ed. Computational fluid and solid mechanics. Springer, 2011.
- [CM14] Clement, R. & Mauroy, B. “An archetypal mechanism for branching organogenesis”. *Physical Biology* **11** (2014).
- [Cle12a] Clement, R. et al. “Branching geometry induced by lung self-regulated growth”. *Physical Biology* **9** (2012).
- [Cle12b] Clement, R. et al. “Shape self-regulation in early lung morphogenesis”. *PLoS ONE* **7.5** (2012).
- [Dav17] Davis, A. et al. “Stomach curvature is generated by left-right asymmetric gut morphogenesis”. *Development* **144** (2017), pp. 1477–1483.
- [Fer99] Fertis, D. G. *Nonlinear mechanics*. 2nd ed. CRC Press, 1999.
- [Fun65] Fung, Y. *Foundations of Solid Mechanics*. Prentice Hall, 1965.



- [Fun84] Fung, Y. "Structure and stress-strain relationship of soft tissues". *Biomechanics*. 24. American Society of Zoologists. 1984, pp. 13–22.
- [GL18] George, U. Z. & Lubkin, S. R. "Tissue geometry may govern lung branching mode selection". *Journal of Theoretical Biology* **442** (2018), pp. 22–30.
- [Geo15] George, U. Z. et al. "Quantifying stretch and secretion in the embryonic lung: Implications for morphogenesis". *Mechanisms of Development* **138** (2015), pp. 356–363.
- [Ger11] Germann, P. et al. "Simulating Organogenesis in COMSOL". *Proceedings of the 2011 COMSOL Conference in Stuttgart*. 2011.
- [Gor17] Goriely, A. *The Mathematics and Mechanics of Biological Growth*. Interdisciplinary Applied Mathematics. Springer, 2017.
- [GG92] Graner, F. & Glazier, J. A. "Simulation of biological cell sorting using a two-dimensional extended Potts model". *The American Physical Society* **69**.13 (1992).
- [Hac18] Hackett, R. M. *Hyperelasticity Primer*. 2nd ed. Springer, 2018.
- [Hes11] Hester, S. D. et al. "A multi-cell, multi-scale model of vertebrate segmentation and somite formation". *PLOS Computational Biology* **7**.10 (2011).
- [Hol00] Holzapfel, G. A. *Nonlinear solid mechanics: a continuum approach for engineering*. Wiley, 2000.
- [Hon04] Honda, H. et al. "A three-dimensional vertex dynamics cell model of space-filling polyhedra simulating cell behavior in a cell aggregate." *Journal of Theoretical Biology* **226**.4 (2004), pp. 439–453.
- [IM13] Iber, D. & Menshykau, D. "The control of branching morphogenesis". *Open Biology* **3**.9 (2013).
- [Jon19] Jones, M. R. et al. "A comprehensive analysis of fibroblast growth factor receptor 2b signaling on the epithelial tip progenitor cells during early mouse lung branching morphogenesis". *Frontiers in Genetics* **9**.746 (2019).
- [Kro19] Krogh, A. "The number and distribution of capillaries in muscles with calculations of the oxygen pressure head necessary for supplying the tissue". *Journal of Physiology* **52**.6 (1919), pp. 409–415.
- [LM69] Liebermann-Meffert, D. "Development of form and position of the human stomach and its mesenteries". *Acta. Anat.* **72** (1969), pp. 376–410.
- [LM95] Lubkin, S. R. & Murray, J. D. "A mechanism for early branching in lung morphogenesis". *Journal of Mathematical Biology* **34**.1 (1995), pp. 77–94.

- [Mai01] Mailleux, A. A. et al. "Evidence that SPROUTY2 functions as an inhibitor of mouse embryonic lung growth and morphogenesis". *Mechanisms of Development* **102** (2001), pp. 81–94.
- [Mas04] Massaro, D. et al., eds. *Lung Development and Regeneration*. Vol. 190. Lung Biology in Health and Disease. Marcel Dekker, 2004.
- [MI12] Menshykau, D. & Iber, D. "Simulating Organogenesis in COMSOL: Deforming and Interacting Domains". *Proceedings of the 2012 COMSOL Conference in Milan*. 2012.
- [Mer06] Merks, R. M. H. et al. "Cell elongation is key to in silico replication of in vitro vasculogenesis and subsequent remodeling". *Developmental Biology* **289** (2006), pp. 44–54.
- [Met08] Metzger, R. et al. "The branching programme of mouse lung development". *Nature* **453.5** (2008).
- [MI08] Morishita, Y. & Iwasa, Y. "Growth based morphogenesis of vertebrate limb bud". *Bulletin of Mathematical Biology* **70** (2008), pp. 1957–1978.
- [Now06] Nowotschin, S. et al. "Tbx1 affects asymmetric cardiac morphogenesis by regulating Pitx2 in the secondary heart field". *Development* **133** (2006), pp. 1565–1573.
- [Nye08] Nyeng, P. et al. "FGF10 maintains distal lung bud epithelium and excessive signalling leads to progenitor state arrest, distalization, and goblet cell metaplasia". *Developmental Biology* **8.2** (2008).
- [Oer14] Oers, R. F. M. van et al. "Mechanical cell-matrix feedback explains pairwise and collective endothelial cell behavior in vitro". *PLOS Computational Biology* **10.8** (2014).
- [Oku14] Okuda, S. et al. "Vertex dynamics simulations of viscosity-dependent deformation during tissue morphogenesis". *Mechanobiology* (2014).
- [OM01] O’Rahilly, R. & Muller, F. *Human Embryology and Teratology*. 3rd ed. Wiley-Liss, 2001.
- [Phi13] Phillips, R. et al. *Physical biology of the cell*. Ed. by Scholl, S. 2nd ed. Garland Science, 2013.
- [Rod94] Rodriguez, E. et al. "Stress-dependent finite growth in soft elastic tissues". *Journal of Biomechanics* **27.4** (1994), pp. 455–467.
- [Sch85] Schmidt, R. "A current trend in shell theory: Constrained geometrically nonlinear Kirchhoff-Love type theories based on polar decomposition of strains and rotations". *Computers and structures* **20** (1985), pp. 265–275.
- [Smi05] Smith, R. C. *Smart Material Systems: Model Development*. Frontiers in Applied Mathematics. Society for Industrial and Applied Mathematics, 2005.

- [Com]     *Structural mechanics module user's guide*. 5-3. COMSOL, 2017.
- [SM13]    Szabo, A. & Merks, R. M. H. "Cellular Potts modeling of tumor growth, tumor invasion, and tumor evolution". *Frontiers in Oncology* **3** (2013).
- [Tab08]    Taber, L. A. "Theoretical study of Belousov's hyper-restoration hypothesis for mechanical regulation of morphogenesis". *Biomechanics and Modeling in Mechanobiology* **7.6** (2008), pp. 427–441.
- [Tho61]    Thompson, D. W. *On growth and form*. Ed. by Bonner, J. T. 2nd ed. Cambridge University Press, 1961.
- [Ton06]    Tongen, A. et al. "Biochemical model for appressorial design in *Magnaporthe grisea*". *Journal of Theoretical Biology* **240.1** (2006), pp. 1–8.
- [TN92]     Truesdell, C. & Noll, W. *The non-linear field theories of mechanics*. Ed. by Antman, S. 2nd ed. Springer, 1992.
- [Unb08]    Unbekandt, M. et al. "Tracheal occlusion increases the rate of epithelial branching of embryonic mouse lung via the FGF10-FGFR2b-Sprouty2 pathway". *Mechanics of Development* **125** (2008), pp. 314–324.
- [Wan07]    Wan, X. et al. "Mechanics of mesenchymal contribution to clefting force in branching morphogenesis". *Biomechanics and Modeling in Mechanobiology* **7.5** (2007), pp. 417–426.
- [War05]    Warburton, D. et al. "Molecular Mechanisms of early lung specification and branching morphogenesis". *Pediatric Research* **57** (2005), pp. 26–37.
- [Wom18]    Womble, M. et al. "The left-right asymmetry of liver lobation is generated by Pitx2c-mediated asymmetries in the hepatic diverticulum". *Developmental Biology* **439.2** (2018), pp. 80–91.

## **APPENDICES**

## APPENDIX

### A

# PRELIMINARY NUMERICAL EXPERIMENTS

We tested the morphoelastic framework on some simple shapes to gain more knowledge of our models' behavior before continuing to more complex shapes. We tested combinations of anisotropic and isotropic inhomogeneous growth for both solid and shell mechanics where we considered growth to be occurring only in a subset of the domain. We tested five individual growth models in a simplified cylindrical geometry using the cylindrical coordinates  $(r, \theta, z)$  as seen in Figure A.1. Our boundary conditions on the top and bottom were no  $z$ -displacement, for a displacement vector  $u = (u, v, 0)$ , and no rotation. The other faces had a no stress boundary condition,  $\hat{n} \cdot \sigma = 0$ .

We modeled inhomogeneous growth, occurring just in a circular zone on the side of the cylin-

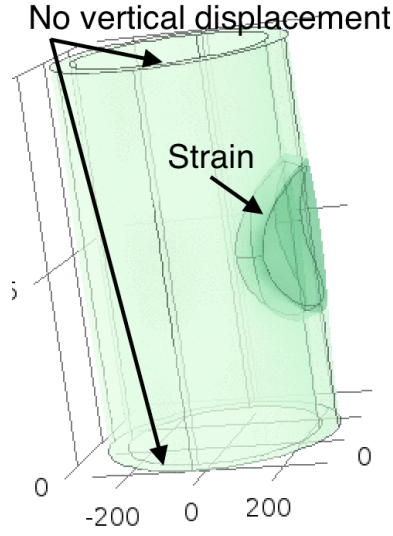


**Figure A.1** Cylindrical geometry for preliminary experiments. The simplified geometry was the same for both solid mechanics and shells. Consider a cylinder whose boundary conditions are no z-displacement and no rotation at the top or bottom. On that cylinder in the slightly darker circle is where the different growth strains were applied. The cylinder had a radius of  $250 \mu\text{m}$ , a height  $750 \mu\text{m}$ , and a thickness of  $50 \mu\text{m}$ .

der, five different ways: (a) volume conservation where the cylinder shrank circumferentially and elongated axially ( $\lambda > 1$ ), so the growth tensor for the circular region was

$$\mathbf{G}(r, \theta, z) = \begin{bmatrix} 1 & 0 & 0 \\ 0 & 1/\lambda & 0 \\ 0 & 0 & \lambda \end{bmatrix}, \quad (\text{A.1})$$

(b) volume conservation where the cylinder shortened axially and grew circumferentially ( $\lambda > 1$ ), so

the growth tensor for the circular region was

$$\mathbf{G}(r, \theta, z) = \begin{bmatrix} 1 & 0 & 0 \\ 0 & \lambda & 0 \\ 0 & 0 & 1/\lambda \end{bmatrix}, \quad (\text{A.2})$$

(c) growth circumferentially, so the growth tensor for the circular region was

$$\mathbf{G}(r, \theta, z) = \begin{bmatrix} 1 & 0 & 0 \\ 0 & \lambda & 0 \\ 0 & 0 & 1 \end{bmatrix}, \quad (\text{A.3})$$

(d) growth axially, so the growth tensor for the circular region was

$$\mathbf{G}(r, \theta, z) = \begin{bmatrix} 1 & 0 & 0 \\ 0 & 1 & 0 \\ 0 & 0 & \lambda \end{bmatrix}, \quad (\text{A.4})$$

and (e) growth both axially and circumferentially, so the growth tensor for the circular region was

$$\mathbf{G}(r, \theta, z) = \begin{bmatrix} 1 & 0 & 0 \\ 0 & \lambda & 0 \\ 0 & 0 & \lambda \end{bmatrix}. \quad (\text{A.5})$$

Volume conservation, in (a)-(b), where  $\det(\mathbf{G}) = 1$ , represented pure cell rearrangement; (c)-(e) represent possibly non-uniform cell division. The results of these five tests can be seen in Figure A.2 for the solid mechanics case and in Figure A.3 for the shell case, where strain is equivalent to  $\lambda - 1$ . Whereas these tests separate the two different processes of cell rearrangement and volume increase, they can be concurrent, but the effects are then harder to see.

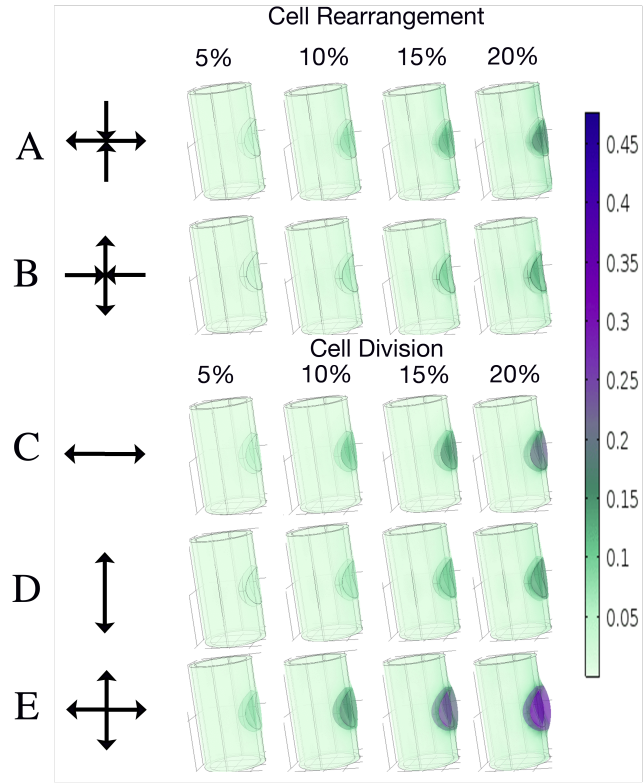


**Figure A.2** Application of local growth strain to a solid cylinder in a cylindrical coordinate system. Using a cylinder that has a height to radius ratio of 3:1, we tested the solid mechanics version of this problem. Going from left to right, we increased the strain by 5% increments from 5% to 20%. More dramatic shape changes would be expected at 20% than at 5%. The color bar represents first principal strain. In (A)-(B), we tested cell rearrangement cases. In (A), the cylinder grew circumferentially but the height shrank and in (B) its height grew but it decreased circumferentially. (C)-(E) are the cellular division cases, where volume is not conserved. In (C) the cylinder grew circumferentially, in (D) along the height, and in (E) in both directions.



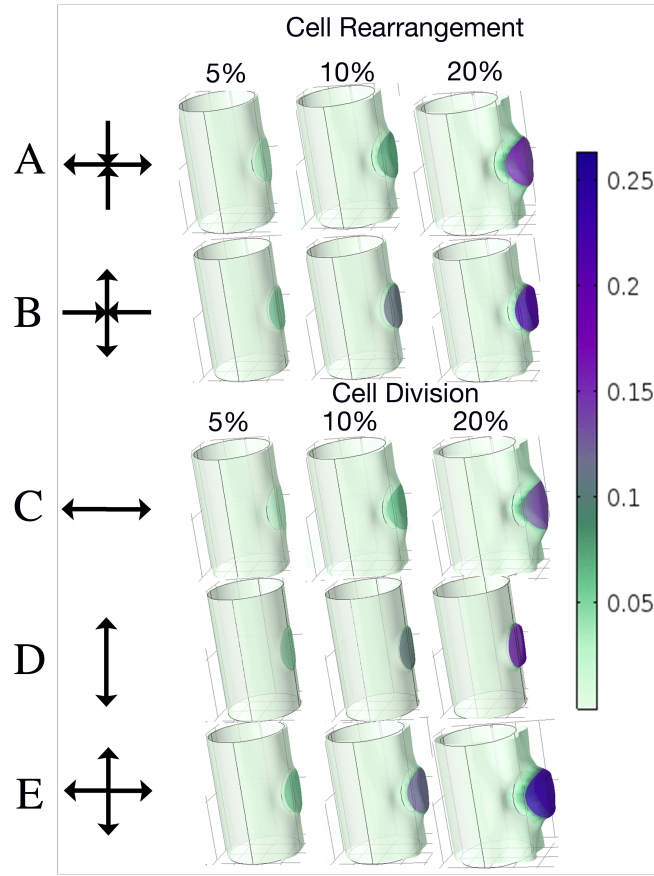


**Figure A.3** Application of local growth strain to a cylindrical shell in a cylindrical coordinate system. Using the shell formulation instead, we tested the same geometry and growth models as in Figure A.2. Going across we increased the strain from 5% to 10% to 20%. 15% was disregarded because it gave no additional information. The color bar represents first principal strain. In (A)-(B), we tested cell rearrangement cases. In (A), the cylinder grew circumferentially but the height shrank and in (B) its height grew but it decreased circumferentially. (C)-(E) are the cellular division cases, where volume is not conserved. In (C) the cylinder grew circumferentially, in (D) along the height, and in (E) in both directions.

A simple change in boundary condition can lead to a dramatically different result, as can be seen in Figure A.4: instead of no displacement on both ends,  $z$ -displacement is allowed on one for the shell formulation. Additionally, if there is a solid inside the shell this affects the outcome. As shown in Figure A.5, the solid material mechanically resists the thin shell's growth.

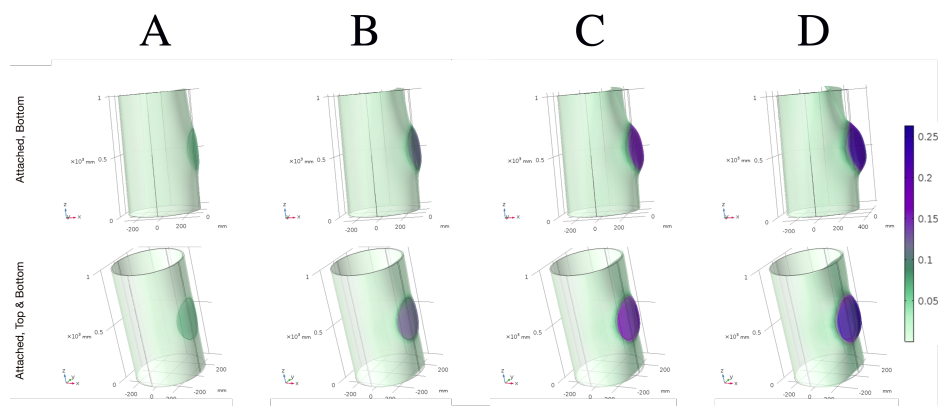


**Figure A.4** Effects of boundary conditions. To emphasize that boundary conditions can drastically affect results, two similar cases are shown. Going across the strain is increased by 5% from (A) 5%, (B) 10%, (C) 15%, and (D) 20%. The color bar represents first principal strain. The top row is where this shell formulation has no vertical displacement only on the bottom of the cylinder. The bottom row is where it has no vertical displacement on both the top and bottom of the cylinder. All other conditions are exactly the same. Notice that the top row has interesting dimpling or buckling above the area of strain.

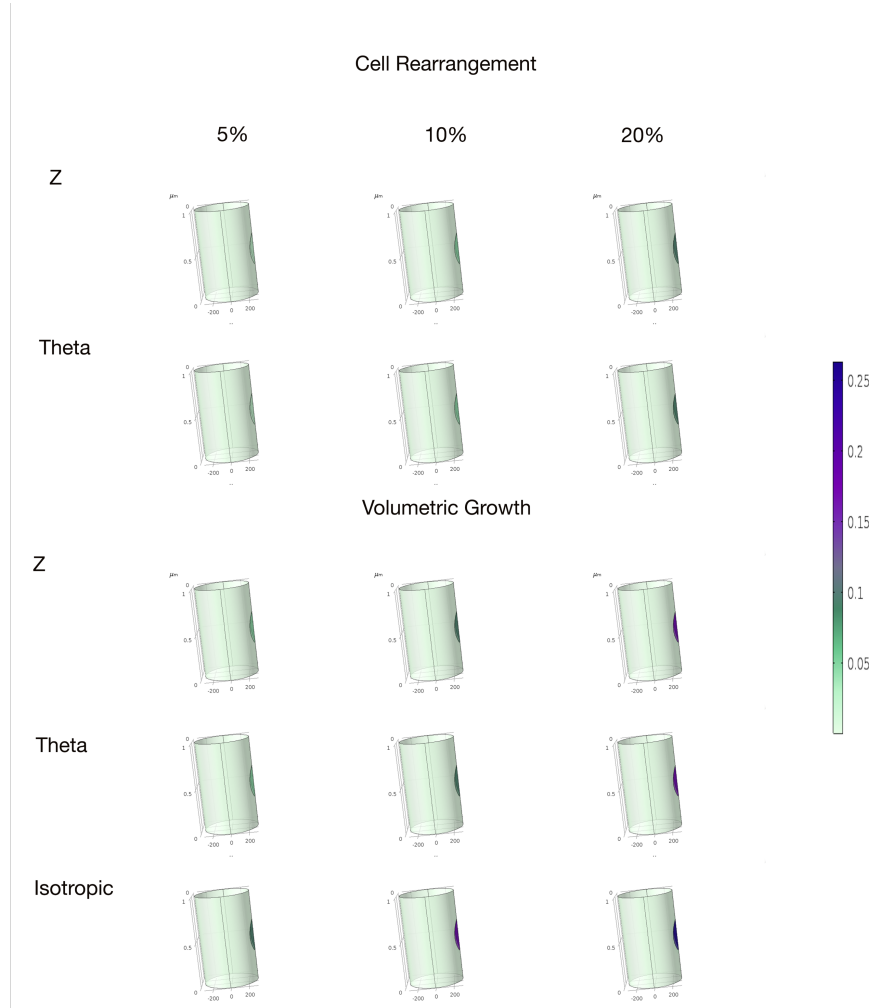


**Figure A.5** Cylindrical shell strained while surrounding a solid material. Using the shell formulation but with a relatively low stiffness solid inside, we tested the same geometry. Going across we increased the strain from 5% to 10% to 20%. From top to bottom, we grouped cell rearrangement together, first increasing height and then increasing circumferentially. Then we grouped volumetric growth together increasing in height, then circumference, and then both. Notice that there is very little overall deformation and the strained circle remains in a very similar location and configuration compared to how it began. The color bar represents first principal strain.

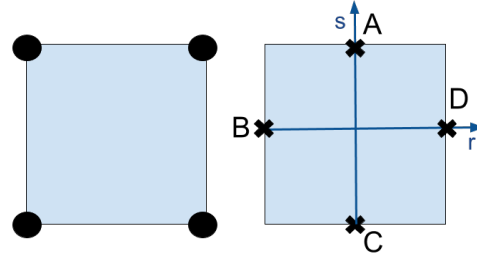
## APPENDIX

### B

# MIXED INTERPOLATION OF TENSORIAL COMPONENTS

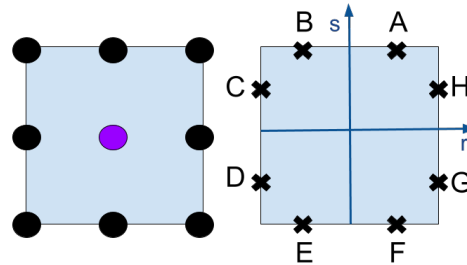
Mixed interpolation of tensorial components, MITC, is a finite element method commonly used for solving equations of shells and plates. COMSOL uses this technique to solve for the solutions to shell problems. MITC methods utilize *tying points* which are specific points selected so that components of the reduced shear strain tensor are considered to be exactly equal to the shear strain calculated from the displacements. Following the notation and language from [CB11] for quadrilateral elements like those we implemented, these tying point components are covariant components in a local coordinate system  $(r, s)$  where  $r$  and  $s$  range from -1 to 1. This is done under the expectation that these covariant components, called  $\zeta_r$  and  $\zeta_s$ , will make the elements more

robust with respect to distortion. There are several potential configurations; we will consider two here. Following convention, the number of interpolation points, four, directly follows the abbreviation MITC for each configuration name. The MITC4 configuration for quadrilateral elements is shown in



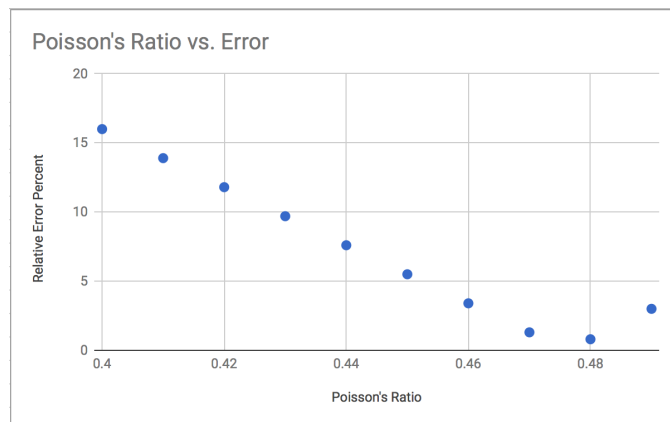
**Figure B.1** For the same element, the left square shows the interpolation points for the displacement,  $\underline{u}$ , and the rotation,  $\underline{\theta}$ . In the right square, the tying points are represented by crosses and labelled with A, B, C, and D. As represented in the local coordinates (r,s), A is located at (0,1) and B is located at (-1, 0). Notation after that in [CB11].

Figure B.1 and the MITC9 configuration for quadrilateral elements is shown in Figure B.2. Detailed explanations of MITC methods and their performance can be found in [CB11], [Bat90], and [Bat89].



**Figure B.2** For the same element, the left square shows the interpolation points for the displacement,  $\underline{u}$ , and the rotation,  $\underline{\theta}$  as black circles. The additional purple circle represents an additional interpolation point for the rotation only. In the right square, the tying points are represented by crosses and labelled A through H. As represented in the local coordinates (r,s), A is at  $(1/\sqrt{3}, 1)$  and C is at  $(-1, 1/\sqrt{3})$ . Notation after that in [CB11].

Finite element methods for shells like the MITC method are prone to what is called *shear locking*. A numerical method is said to be *locking* if the accuracy of the numerical approximation declines as a parameter goes to a limiting value, as happens in linear elastic problems when the Poisson's ratio  $\nu = 0.5$ . We ran experiments in COMSOL where this was the case, and thus in Chapter 3 only consider Poisson's ratio up to  $\nu = 0.49$ . In a simple example of locking, we considered a domain a 1mm by 1mm square directly abutting another 1mm by 1mm square. Square B had a fixed, non-moving boundary directly opposite the shared edge. Square A was strained 10% isotropically. We used the linear strain formulation and could compute the analytical solution. Figure B.3 shows the error increase as  $\nu$  tends towards the limiting value  $\nu = 0.5$ . While that was a simple linear elastic model,



**Figure B.3** Locking of numerical methods. As shown for a linear elastic solid mechanics model, when Poisson's ratio gets closer to 0.5 the relative percent error decreased in a linear fashion. The slight uptick at  $\nu = 0.49$  indicates locking.

locking can occur in other types of models and is a phenomena observed in shell models. To combat locking COMSOL will fix points surrounding the problematic area and add additional degrees of freedom.